UNIVERSITY OF CALIFORNIA

Los Angeles

Manufacturing and Characterization of Temperature-Stable, Novel, Viscoelastic Polyurea Based Foams for Impact Management

A dissertation submitted in partial satisfaction
of the requirements for the degree
Doctor of Philosophy in Mechanical Engineering

by

Brian Josue Ramirez

2017

© Copyright by

Brian Josue Ramirez

2017

ABSTRACT OF THE DISSERTATION

Manufacturing and Characterization of Temperature-Stable, Novel, Viscoelastic Polyurea Based Foams for Impact Management

by

Brian Josue Ramirez
Doctor of Philosophy in Mechanical Engineering
University of California, Los Angeles, 2017
Professor Vijay Gupta, Chair

The aim of this thesis was to develop advance, high performance polyurea foams for multi-hit capability in protective equipment that respond over a range of impact energies, temperatures, and strain rates. In addition, the microstructure of these materials should be tunable such that the peak stress (or force) transmitted across the foam section can be limited to a specific value defined by an injury threshold while maximizing impact energy absorption.

Novel polyurea foams were manufactured and found to exhibit a reversible viscoelastic shear deformation at the molecular level. The intrinsic shear dissipation process is synergistically coupled to controlled collapse of a novel pore structure. The microstructure compromises of stochastic polyhedral cells ranging from 200 – 500 μm with perforated membranes with small apertures (~ 20 μm). This makes them strain rate sensitive as the rate at which the air escapes the cells depend upon the loading rate. These mechanisms operate simultaneously and sequentially, thereby significantly reducing the transmitted impact forces across the foam section. Thus, they behave as an elastically modulated layered composite because the cells stiffen or soften in response

to the changing loading rate. Therefore, the newly developed polyurea foams are able to manage the varying material strain rate that occurs within the same loading event without the need to modulate the stiffness or density. Additionally, polyurea foams were found to retain its excellent impact properties over a range of temperatures (0°C to 40°C) by having a glass transition temperature well below 0°C. This is in contrast to commercially available high performance foams that have the glass transition temperature near 0°C and absorb energy through phase transformation at ambient conditions, but significantly stiffen at lower temperatures, and dramatically soften at higher temperatures**.** This expands the application domain of polyurea foam material considerably as it can be tailored to withstand a range of dynamic forces and impact velocities, showing further improvement over currently used protective foams.

This thesis also presents a new composite foam concept that involves infiltrating a polyurea-based foam through an open 3D lattice structure with a truss-like network of 2 mm-size struts. The combination of dynamic buckling at the macro (preform lattice struts) and the micro (foam pores) levels increases the stiffness and plateau strength of the composite polyurea foam. The composite foams absorb more impact energy in same section thickness, while keeping both the peak stress and impulse duration low compared to high performance expanded polystyrene (EPS) and Poron foam technology, but without the material crushing or undergoing phase shift, respectively. Most importantly, the composite foams display stability at both low (0°C) and high temperatures (40°C) because of its extremely low T_g of -50°C. Being viscoelastic, they recover fully within 30 s after each impact, without loss of any energy absorption capability. These properties should allow these materials to have a wide range of military and civilian applications, especially in advance armors and protective body and headgear systems.

The dissertation of Brian Josue Ramirez is approved.

Ajit Mal

Nasr Ghoniem

Jaime Marian

Vijay Gupta, Committee Chair

University of California, Los Angeles

2017

Para mi familia…

Table of Contents

List of Figures x
List of Tables xv
Acknowledgements xvi
Vita xviii
CHAPTER 1 1
Introduction 1
1.1 Motivation of Present Study 1
1.2 Objectives of Present Study 3
1.3 Document Organization 4
CHAPTER 2 6
Background: Fundamental Knowledge 6
2.1 Cellular Solids 6
2.1.1 Microstructure 6
2.1.2 Foaming Reaction and Additives 7
2.1.3 Foaming Process 9
2.1.4 Foam Manufacturing 10
2.1.5 Mechanics of Foams 12
2.1.6 Constitutive Modeling of Foams 14
2.2 Polyurea: Review of the Literature 16
2.2.1 Chemistry 17
2.2.2 Mechanical Behavior of Polyurea 19
2.2.3 Impact Properties of Polyurea 25
2.2.4 Modeling of Polyurea 27
2.2.5 Concluding Remarks 30
CHAPTER 3 32
Tailoring the Rate-Sensitivity of Low Density Polyurea Foams through Cell Wall Aperture Size 32
3.1 Introduction 32

3.2 Material Preparation and Characterization 36
3.3 Experimental Techniques 38
3.3.1 Low and Intermediate Strain Rate Testing 38
3.3.2 High Strain Rate Testing 39
3.4 Results 41
3.4.1 Low and intermediate strain rates 41
3.4.2 High strain rate response 46
3.5 Conclusions 49
CHAPTER 4 51
Impact Attenuation of Viscoelastic Polyurea Foam Liners in Helmets 51
4.1 Introduction 51
4.2 Materials 52
4.3 Experimental Procedures 54
4.3.1 Compression tests 54
4.3.2 NOCSAE Standard Tests 55
4.3.3 Severity Index and Head Injury Criteria 57
4.3.4 Federal Motor Vehicle Safety Standards (FMSS) Liner Tests 58
4.4 Results and Discussion 60
4.4.1 Compression Test Results 60
4.4.2 NOCSAE Helmet Test Results 62
4.4.3 FMVSS Liner Test Results 66
4.5 Conclusions 67
CHAPTER 5 68
Shock Attenuation Properties of Polyurea Based Foams for Midsoles in Footwear 68
5.1 Introduction 68
5.2 Materials and Methods 70
5.2.1 Materials 70
5.2.2 Quasi-static Compression Tests 71
5.2.3 Impact Attenuation Tests 72
5.2.4 Relative Rebound Energy and Maximum Displacement 73
5.3 Results and Discussion 74
5.3.1 Quasi-Static Compression Results 74

5.3.2 Shock Attenuation Results 76
5.3.3 Rebound Energy and Displacement Results 79
5.4 Conclusions 82
CHAPTER 6 83
Mechanical Properties of Newly Developed Polyurea Based Foams 83
6.1 Introduction 83
6.2 Materials 83
6.3 Experimental Methods 84
6.3.1 Hardness 84
6.3.2 Tensile Strength and Elongation 85
6.3.3 Compression Set 86
6.3.4 Resiliency 86
6.3.5 Tear Strength 87
6.4 Results and Discussion 88
6.5 Conclusion 94
CHAPTER 7 96
Temperature-Stable, Novel, Viscoelastic, Composite Polyurea Foams for Impact Management 96
7.1 Introduction 96
7.2 Material Preparation and Characterization 97
7.3 Experimental Methods and Procedures 100
7.3.1 Low and Intermediate Strain Rate Testing 100
7.3.2 Reduction of Data: Energy Absorption Diagrams 101
7.4 Results 102
7.4.1 Stress-Strain Characteristics 102
7.4.2 Strain Rate Effects 104
7.4.3 Energy Absorption Results 108
7.4.4 Impact Test Results 109
7.5 Conclusions 113
CHAPTER 8 116
Modeling the Compressive Stress-Strain Behavior of Polyurea Foams 116
8.1 Modeling of Cellular Solids 116
8.1.1 Quasi-static Models 116

8.1.2 Dynamic Models 119
8.1.3 Chapter Objectives 120
8.2 Materials 120
8.3 Experimental Methods 120
8.4 Results and Discussion 120
8.4.1 Stress-strain Results 120
8.4.2 Goga Foam Model Results 122
8.4.3 Jeong Foam Model Results 125
8.5 Conclusion 128
Chapter 9 129
Conclusions and Outlook 129
References 132

List of Figures

Figure 2.1: Open cell (Left) and closed cell (Right) [14]. 7

Figure 2.2: Slabstock foaming machine [19]. 11

Figure 2.3: Carousel molded foam machine [20]. 11

Figure 2.4: Typical compressive stress-strain curve for cellular materials [14]. 13

Figure 2.5: Comparing Hyperfoam model with experimental data in (Left) compression (Right) simple shear [21]. 15

Figure 2.6: Stress relaxation data compared to viscoelastic model [22]. 16

Figure 2.7: Polyurea formulation. 17

Figure 2.8: AFM of polyurea film [25]. 18

Figure 2.9: Stoichiometric effect on the stress-strain behavior of polyurea ($\varepsilon = .06s - 1$)[25]. 20

Figure 2.10: Storage and loss moduli for polyurea with varying index (1 Hz) [27]. 21

Figure 2.11: Stress-strain behavior of polyurea under (*Left*) no confinement *(Right*) confinement [29]. 22

Figure 2.12: Strain rate effect on the tensile stress-strain behavior of polyurea [31]. 23

Figure 2.13: Strain rate effect on the compressive stress-strain behavior of polyurea [33]. 23

Figure 2.14: Shear response of polyurea under varying pressures and shearing rates [34]. 25

Figure 2.15: Steel-polyurea bilayer specimens under pressure-pulse experiments (*Top*) Polyurea on the front surface (*Bottom*) Polyurea on the back surface [37]. 26

Figure 2.16: Li and Lua [48] model of polyurea behavior under varying strain rates. 28

Figure 2.17: (*Left*) Master relaxation curve (*Right*) Shift factor as function of time [49]. 29

Figure 2.18: Comparison of experimental and modeled behavior of polyurea [51]. 30

Figure 3.1: Scanning electron micrographs of the microstructure of (A) Polyurea Foam PU 280, and (B) polyurea foam PU300. 37

Figure 3.2: Scanning electron micrograph of the microstructure of expanded polystyrene foam EPS72. 38

Figure 3.3: Stress-strain behavior of polyurea PU280 foam at quasi-static and intermediate strain rates. 42

Figure 3.4: Stress-strain behavior of polyurea PU300 foam at quasi-static and intermediate strain rates. 43

Figure 3.5: Stress-strain behavior of expanded polystyrene EPS72 foam at quasi-static and intermediate strain rates. 43

Figure 3.6: The plateau stress and energy absorption as a function of strain rate for expanded polystyrene EPS72 foam and polyurea foams PU280 and PU300. 45

Figure 3.7: Stress-strain behavior of expanded polystyrene EPS72 foam at high strain rates. 47

Figure 3.8: Stress-strain behavior of polyurea PU280 foam at high strain rates. 47

Figure 3.9: Stress-strain behavior of polyurea P300 foam at high strain rates. 48

Figure 3.10: Strain-rate dependence of the plateau strength of PU foams. The broken lines are the predicted contribution to the plateau stress due to the aperture size effect, based on Equation (6). 49

Figure 4.1: SEM images of the microstructure of PU Foams. 53

Figure 4.2: SEM image of the microstructure of VN Foam. 53

Figure 4.3: NOCSAE standard impact test setup for football helmets. 56

Figure 4.4: PU98 foams inside the Riddell football helmet. 57

Figure 4.5: (Left) 5 kg DOT size-C dummy headform, (Middle) 6 mm thick skull-cap, and (Right) Motorcycle Helmet. 59

Figure 4.6: Engineering stress-strain behavior of PU98, PU170, PU230, and VN600 under quasi-static deformation rate of 0.04 s^{-1}. 61

Figure 4.7: Engineering stress-strain behavior of PU98, PU170, PU230, and VN600 under dynamic deformation rate of 200 s^{-1}. 61

Figure 4.8: Head Acceleration of NOCSAE tests using polyurea foams compared to VN. 64

Figure 5.1: Typical ground reaction force while running [2]. 68

Figure 5.2: Drop-weight tower for impact tests. 73

Figure 5.3: Stress-strain behavior of PU foams at a strain rate of 0.004 s^{-1}. 75

Figure 5.4: Force-time curves at 5 J impact for (A) PU foams and (B) EVA and TPU foams. ... 76

Figure 5.5: Force-time curves at 7 J impact for (A) PU foams and (B) EVA and TPU foams. ... 77

Figure 5.6: Force-time curves at 5 J impact for (A) PU foams and (B) EVA and TPU foams with polyurea dense film. ... 78

Figure 5.7: Force-time curves at 7 J impact for (A) PU foams and (B) EVA and TPU foams with polyurea dense film. ... 78

Figure 5.8: Typical force-deflection for PU foams at 5 J impact energy. ... 79

Figure 5.9: Relative rebound energy values for foam and bilayer samples. ... 80

Figure 5.10: Maximum deflection of foam and bilayer system at a 5J impact energy. ... 81

Figure 6.1: Indentation test of PU foam using Asker C durometer. ... 85

Figure 6.2: Tension specimen dimensions [82]. ... 85

Figure 6.3: Compression set test set-up. ... 86

Figure 6.4: Resiliency test showing steel ball and plastic tube for measuring the rebound height. ... 87

Figure 6.5: Tear strength specimens (*Left*) Die-C (*Right*) Split. ... 88

Figure 6.6: The effect of density on the hardness of PU and TPU foams. ... 89

Figure 6.7: The effect of density on the tensile strength of PU and TPU foams. ... 90

Figure 6.8: The effect of density on the elongation of PU and TPU foams. ... 90

Figure 6.9: The effect of density on the compression set of PU and TPU foams. ... 91

Figure 6.10: The effect of density on the resiliency of PU and TPU foams. ... 92

Figure 6.11: The effect of density on the Die-C tear strength of PU and TPU foams. ... 93

Figure 6.12: The effect of density on the Split Test tear strength of PU and TPU foams. ... 93

Figure 7.1: Preform polymer lattice. ... 98

Figure 7.2: Foaming of preform lattice material to create composite polyurea foam (**A**) Side-view (**B**) Top-view. ... 98

Figure 7.3: SEM Images of (A) CPF240 (B) Poron320 and (C) EPS72. 99

Figure 7.4: Quasi-static ($\dot{\varepsilon} = 0.04s^{-1}$) compressive stress-strain behavior of preform lattice-PL135, polyurea foam-PU112, and composite polyurea foam-CPF240. 103

Figure 7.5: Dynamic ($\dot{\varepsilon} = 200s^{-1}$) compressive stress-strain behavior of preform lattice-PL135, polyurea foam-PU112, and composite polyurea foam-CPF240. 104

Figure 7.6: Quasi-static ($\dot{\varepsilon} = 0.04s^{-1}$) compressive stress-strain behavior of CPF240, EPS72, and Poron320. 107

Figure 7.7: Dynamic ($\dot{\varepsilon} = 200s^{-1}$) compressive stress-strain behavior of CPF240, EPS72, and Poron320. 107

Figure 7.8: Quasi-static ($\dot{\varepsilon} = 0.04s^{-1}$) (A) energy absorption-W and (B) cushioning efficiency-CE as a function of stress for CPF240, EPS72, and Poron320. 108

Figure 7.9: Dynamic ($\dot{\varepsilon} = 200s^{-1}$) (A) energy absorption-W and (B) cushioning efficiency-CE as a function of stress for CPF240, EPS72, and Poron320. 109

Figure 7.10: Stress-time history of CPF240, EPS72, and Poron320 samples impacted by (A) 5 J (B) 10 J (C) 15 J (D) 20 J and (E) 25 J energy. 110

Figure 7.11: Stress-time history of CPF240, EPS72, and Poron320 samples impacted by 15 J energy (A) 1st hit, (B) 2nd hit, and (C) 3rd hit. 111

Figure 7.12: Stress-time history of CPF240, EPS72, and Poron320 samples impacted by 15 J energy at (A) 40°C and (B) 0°C. 113

Figure 8.1: Stress-strain behavior of Goga foam model [84]. 118

Figure 8.2: Stress-strain behavior of PU foam with density of 140 kg/m^3 at increasing strain rates. 121

Figure 8.3: Stress-strain behavior of PU foam with density of 180 kg/m^3 at increasing strain rates. 121

Figure 8.4: Stress-strain behavior of PU foam with density of 200 kg/m^3 at increasing strain rates. 122

Figure 8.5: PU-140 kg/m^3 experimental data vs. Goga model (A) .004 (B) .04 (C) .4 (D) 60 s^{-1}. 123

Figure 8.6: PU-180 kg/m^3 experimental data vs. Goga model (A) .004 (B) .04 (C) .4 (D) 60 s^{-1}. 124

Figure 8.7: PU-200 kg/m^3 experimental data vs. Goga model (A) .004 (B) .04 (C) .4 (D) 60 s^{-1}. 124

Figure 8.8: PU-140 kg/m^3 experimental data vs. Jeong model (A) .004 (B) .04 (C) .4 (D) 60 s^{-1}. 126

Figure 8.9: PU-180 kg/m^3 experimental data vs. Jeong model (A) .004 (B) .04 (C) .4 (D) 60 s^{-1}. 127

Figure 8.10: PU-200 kg/m^3 experimental data vs. Jeong model (A) .004 (B) .04 (C) .4 (D) 60 s^{-1}. 127

List of Tables

Table 4.1: Headform's impact velocity, peak head gs, GSI, and HIC values using PU Foams. .. 63

Table 4.2: Headform's impact velocity, peak head gs, GSI, and HIC values comparing PU with VN Foams. 64

Table 4.3: Headform's impact velocity and peak head gs comparing PU and VN Foams at different temperatures. 65

Table 6.1: The effect of density on the mechanical properties of PU foams. 94

Table 6.2: The effect of density on the mechanical properties of TPU foams. 94

Table 8.1: Goga constitutive model parameters for PU foams. 125

Table 8.2: Jeong constitutive model parameters for PU foams. 126

Acknowledgements

I would like to first thank my parents Lorenzo and Elisa, my three siblings: Elizabeth, Irving and Michael, my brother-in-law Rick, and my beautiful niece Victoria for their unconditional love and support throughout my educational journey, without them, none of this would have been possible. A huge thanks to all my friends, cousins, aunts, uncles, and grandparents for their continued encouragement and belief in me. Thank you to my girlfriend Bianca, for the countless dinner meals, editing my writing, and more importantly for the encouragement to continue to work hard during tough times.

I would like to acknowledge my advisor, Professor Vijay Gupta, for all the research guidance and mentorship during my time at UCLA. I would also like to thank the members of my committee: Professor Ajit Mal, Professor Nasr Ghoniem, and Professor Jamie Marian for their academic and professional guidance.

Ryan and Carlos: thank you so much for welcoming me into the lab and for your willingness to assist me with any technical difficulties I faced in my research. I also want to thank Dr. Owen Kingstedt and my undergraduate student Utkarsh Misra for your help and contributions to my research. I am also grateful to have shared lab space with Professor Lynch's students: Peng, Rodolfo, Jizhai, Xu, Auni, Chris, Yu-Ching and Hwan who made coming to lab enjoyable and all that I learned from our discussions. I am also thankful for my interactions with MAE staff members: Abel, Angie, and Heejin for all their administrative assistance, as well as Jose and Anatolli for the much needed assistance in the machine shop, and Sergey from the Material Science department for your help with SEM training.

I would also like to thank the Graduate Division at UCLA, especially Anna Guzman, Anne Dela Cruz, Professor Carlos Grijalva, and Sarah Valdovinos for opening the doors to some amazing opportunities such as the Competitive Edge Summer Program, the Bouchet Honors Society, and the California Alliance Program.

My deepest gratitude goes out to my undergraduate advisors at Cal Poly Pomona: Professor Mehrdad Haghi, Professor Winny Dong, Professor Wei Bidlack, Professor Frank Torres, and Professor Angela Shih who introduced me to research and the possibility of obtaining a Ph.D. I also thank you for the academic, professional, and life advice that set me on the path that I am today. I would also like to thank Professor Ravichandran from Caltech for his mentorship since my days as summer undergraduate researcher in his lab.

Lastly, I wish to acknowledge the grant support from the Office of Naval Research, through Grant No. N0008. Additionally, I would like to acknowledge the support from the Eugene V. Cota-Robles Fellowship (UCLA), the Dissertation Year Fellowship (UCLA), The East Los Angeles Community Union (TELACU) Graduate Fellowship (a special thanks to David and Priscilla Lizarraga for their support and encouragement), the City of Commerce Scholarship, and the Boeing Graduate Scholarship.

Vita

Education

2008	Schurr High School Montebello, California
2013	B.S. Mechanical Engineering, Minor in Material Science California State Polytechnic University, Pomona
2015	M.S. Mechanical Engineering, Solid and Structural Mechanics University of California, Los Angeles

Honors and Awards

2010-2012	Ronald E. McNair Scholars Program California State Polytechnic University, Pomona
2011	LSAMP-Louis Stokes Alliance for Minority Participation California State Polytechnic University, Pomona
2012	Summer Undergraduate Research Fellowship California Institute of Technology
2013-2017	Eugene V. Cota-Robles Graduate Fellowship University of California, Los Angeles
2016-2017	Dissertation Year Fellowship University of California, Los Angeles
2017	Edward A. Bouchet Graduate Honor Society-UCLA 2017 Inductee

Publications

V. Gupta, N. Ghoniem, R. Crum, G. Po, D. Seif, S.V. Prikhodko, H.A. Colorado, **B. Ramirez**, C. Gámez, Microstructure evolution in metal nanostructures under extreme conditions of temperature and strain rate, Proceedings of the Indian National Science Academy 82 (2) (2016) 201-208.

V. Gupta, R. Crum, C. Gamez, **B. Ramirez**, N. Le, G. Youssef, J. Citron, A. Kim, A. Jain, and U. Misra, Adhesive and Ultrahigh Strain Rate Properties of Polyurea Under Tension, Tension/Shear, and Pressure/Shear Loadings with Applications to Multilayer Armors, *Elastomeric Polymers with High Rate Sensitivity*, R. Barsoum (Ed.), 71-92, Elsevier (2015)

B. Ramirez, O.T. Kingstedt, R. Crum, C. Gamez, V. Gupta, Tailoring the rate-sensitivity of low density polyurea foams through cell wall aperture size, (*Accepted-Journal of Applied Physics*)

B. Ramirez, U. Misra, V. Gupta, Temperature-stable, novel, viscoelastic, composite polyurea foams for impact management, (*Submitted*)

B. Ramirez, V. Gupta, Biomechanical impact mitigation properties of polyurea based foams in football helmets, (*Submitted*)

R. Crum, C. Gamez, **B. Ramirez**, N. Le, V. Gupta, Observations of intrinsic crazing in polyurea subjected to combined tension-shear loading at ultrahigh strain rates**,** (*Submitted*)

C. Gamez, R. Crum, **B. Ramirez**, V. Gupta, Failure of polyurea under combined pressure/shear loading at ultrahigh strain rates**,** (*Submitted*)

M. Sarraf, A.R. Bushroa, N.H. Kasim, B. Nasiri-Tabrizi, R. Crum, C. Gamez, **B. Ramirez**, V. Gupta, Adhesion measurement of highly-ordered TiO_2 nanotubular arrays coated on Ti–6Al–4V, (*Submitted*)

Presentations

B. Ramirez, Manufacturing and Characterization of Polyurea Based Foams, *Lawrence Livermore National Laboratory Seminar*, Livermore, CA, December 7, 2016 (Invited Speaker)

B. Ramirez, V. Gupta, Characterization of UCLA Composite Foam under Quasi-static and Dynamic Compressive Loadings, *2016 Society of Hispanic Engineers (SHPE) Conference, Seattle, WA*, November 4, 2016

B. Ramirez, V. Gupta, Dynamic Properties of Newly Developed UCLA Polymer Foams, *California Alliance Third Annual Retreat, University of California, Berkeley*, April 8, 2016

B. Ramirez, V. Gupta, Strain Rate Effect on the Elastic Properties of Newly Developed UCLA Polymer Foams, *2015 Society of Hispanic Engineers (SHPE) Conference, Baltimore, MD*, November 13, 2015

B. Ramirez, N. Lee, D. Gupta, V. Gupta, Orientation-Dependent Impact Behavior of Polymer/EVA Bilayer Specimens at Long Wavelengths, *2014 Society for the Advancement of Chicanos and Native Americans in Science (SACNAS), Los Angeles, CA*, October 18, 2014 (Poster)

Patents

Vijay Gupta, **Brian Ramirez**, and Utkarsh Misra, "Composite Foam"
U.S. Patent Serial No.62/316,241

CHAPTER 1

Introduction

1.1 Motivation of Present Study

Elastomeric foams of varying densities are widely used in protective head and body gears and in a variety of mechanical, civil, and aerospace structures for protection against blast and impact loads [1-2]. Foams manage impact by undergoing large deformations under low stress by increasing the time over which the velocity of the incoming impact is arrested and by dissipating the impact energy through local viscoelastic or plastic crushing processes through bending, twisting, and buckling of the struts that form the skeleton of its structure [3-13]. The compressive stress-strain behavior of a typical viscoelastic or a plastic foam exhibits three distinct regions: (i) a linear elastic region associated with cell wall bending, (ii) a stress plateau region that results from continuous collapse of the foam's cell structure on itself through non-linear fully recoverable (viscoelastic foams) or irrecoverable (plastic foams) buckling of its struts, and (iii) a densification region where the already-collapsed cells begin to compress against each other to near full density, resulting in a steeply rising stress. The amount of energy absorbed or dissipated by the foam is roughly equal to the area under its stress-strain curve.

For a given foam thickness, which is typically constrained by the specific application, the design process reduces to determining the lowest density of the foam per unit volume that keeps the peak load below the injury threshold level without bottoming out. For head health applications, the peak transmitted stress must be kept below 1.5 MPa [14-15]. The manufacturing technology has advanced significantly over the past two decades in that any polymer can be foamed into the

desired density through control of process variables and by use of various surfactants, foaming and gelling agents. The industrial processes are also well developed to produce foams with *uniform* microstructures in large quantities at fairly low cost. Today foams are used in practically every industry. Despite their ubiquity and maturity, there are several areas where improvements in the foam technology can be made, especially those that pertain to impact applications, as discussed next.

Expanded polystyrene (EPS) based systems are lightweight (with densities on the order of 45-75 kg/m^3) and absorb impact energy through plastic crushing [9-11]. Because they are effective energy absorbers in small section thicknesses (less than 1"), they are widely used as liners in protective body and headgear systems, including commercial bicycle and motorcycle helmets. An advantageous property of EPS foams is the ability to keep the peak crushing stress below the injury threshold level by choosing an appropriate foam density. EPS72 with a density of 72 kg/m^3 is the most efficient in absorbing impact energy among all currently available foam systems at the stress level of 1.2 MPa [14]. A major drawback of EPS foams is that they do not recover after plastic crushing and therefore provide reduced protection during subsequent impacts which at times may occur in the same event. This single event constraint severely limits the use of EPS in sports.

Another class of high performance foams that overcome the single-hit limitation of EPS foams are those that use phase transformation as their energy dissipation mechanism [16]. These materials have a glass transition temperatures, T_g, near 0°C and recover fully after each impact. The material undergoes a reversible rubbery-to-glassy phase transition due to the shift in T_g associated with very short duration loading. As shown later, these materials outperform most foams albeit under ambient conditions. At moderately lower temperatures (0°-5°C), below their T_g, they become hard and transmit very high forces as their microstructure has already transitioned

into the glassy phase. This makes them impractical for use in applications that require performance over a range of temperatures. Furthermore, they are unable to pass any temperature-based industry standard tests. Poron and Poron-XRD foams made by Rogers Corporation are examples of such foams [17].

Almost every current application utilizes foams with a *uniform* microstructure. Even with the choice of the lowest density these foams are not truly optimized. This is because the initial linear response and the plateau stress which determine the impact attenuation and momentum trapping properties of the foam depend strongly on the loading rate [3-13] which changes within the same impact event. The material strain rate is lower at the start of the loading as the foam cells start to collapse, and then builds up quickly during the densification process, and finally, reduces significantly when the velocity of the impactor has slowed down substantially. One way to *further* optimize the foam's performance is to create a section with modulated stiffness or density to account for this varying material strain rate. Such a foam structure cannot be manufactured in a single low-cost manufacturing step. It would require lamination where foam layers of different density, stiffness, and thickness are stacked up in a specific order. In addition to being expensive, the lamination process is not easily scalable as required for production of high volume commodity products.

1.2 Objectives of Present Study

The aim of this thesis was to create a class of high performance low density (less than 250 kg/m^3) *viscoelastic* polyurea foams that absorb more energy than EPS foams of similar or lower densities and retain their performance over a range of temperature (0°C to 40°C) and strain rate (50 s^{-1} to 5000 s^{-1}) loading in section thicknesses of 25 mm or less. In addition, the microstructure of these

materials should be tunable such that the peak stress can be kept below the injury threshold level such as 1.2 MPa for head health applications.

1.3 Document Organization

Reporting of this thesis is organized into six main chapters, excluding the introduction (Chapter 1), background knowledge (Chapter 2), and conclusions (Chapter 9). **Chapter 3** presents the plateau stress and energy absorption of low density (≤ 300 kg/m^3) polyurea (PU) foams measured at deformation rates ranging from 0.004 s^{-1} to 5000 s^{-1}. In **Chapters 4**, the combined benefits of temperature stability and rate sensitivity of low density (≤ 200 kg/m^3) viscoelastic polyurea based foams are demonstrated by integrating them as liners into football and motorcycle helmets. Football and motocross helmet drop tests were investigated using the National Operating Committee for Standards in Athletic Equipment (NOCSAE) standards and Federal Motor Vehicle Safety Standards (FMVSS) 218, respectively. **Chapter 5** studies the impact attenuation, rebound energy (resiliency), and maximum deflection of polyurea foams and polyurea foam/polyurea dense film bilayer systems at 5 and 7 J impact energies according to the American Society for Testing and Materials (ASTM) test methods F1976 and D3574 for their application as midsoles in footwear. In **Chapter 6**, the effect of density on the cell size, hardness, compression set, tensile strength, elongation, tear strength, and resiliency are presented following ASTM-D3574 standards. **Chapter 7** introduces a new composite foam concept that involves infiltrating a polyurea-based foam through an open 3D lattice structure with a truss-like network of 2 mm-size struts. The stress-strain characteristics, energy absorption, and cushioning efficiency are measured at quasi-static and dynamic strain rates using an Instron load frame and a drop tower facility, respectively. Lastly,

Chapter 8 investigates the use of both constitutive and phenomelogical models to predict the quasi-static and dynamic stress-strain behavior of low density polyurea foams.

CHAPTER 2

Background: Fundamental Knowledge

2.1 Cellular Solids

Cellular solids, also referred to as foams (3D) or honeycombs (2D), are widely used in structural, thermal, and acoustic applications for weight reduction. More importantly, they are used for their impact absorption properties along with providing comparable stiffness and strength to that of the solid material from which they are foamed. The interaction between the mechanical properties of the solid polymeric material and the cellular structure of foams give them the unique ability to dissipate a wide range of impacts. This subsequent section provides an overview on flexible polymer foams.

2.1.1 Microstructure

Foams are three-dimensional cellular solids that are made up of interconnected network of beams and columns. If the material is distributed along the edges (sometimes identified as struts), it is referred to as an open cell foam. In an open cell foam, air can flow freely within the foam. On the other hand, if the material is distributed along the faces, the foam is referred to as a closed cell foam. Here, gas or air is trapped within each cell. Figure 2.1 shows the microstructure of an open and closed cell foam.

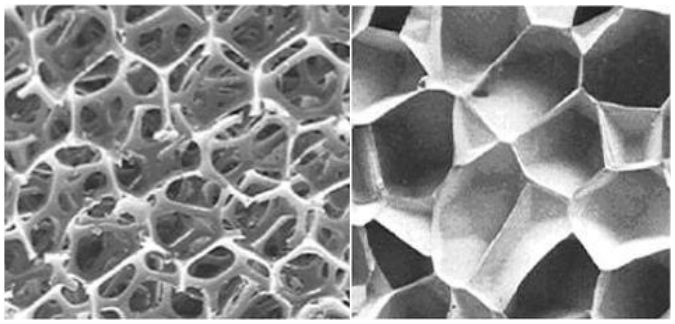


Figure 2.1: Open cell (Left) and closed cell (Right) [14].

The microstructure of a foam is usually analyzed geometrically using Euler's law [14], expressed as

$$-C + F - E + V = 1 \tag{2.1}$$

where C is the number of cells, F is the number of faces, E is the number of edges, and V is the number of vertices (the nodes where the struts meet). For a single cell (C=1), we can obtain a relationship between the number of edges per face ($\bar{n}$) and the number of faces F by

$$\bar{n} = \frac{Z_e Z_f}{Z_e - 2}\left(1 - \frac{2}{F}\right) \tag{2.2}$$

where Z_e is the number of edges which meet at a vertex and Z_f is the number of faces which meet at an edge. In foams, the typical values for Z_e is 4 and 3 for Z_f.

2.1.2 Foaming Reaction and Additives

Foaming a polymer consists of two competing reactions: gelling and blowing. The gelling reaction is essentially the polymerization reaction of the strut material. On the other hand, the blowing reaction creates the gas to expand the polymer as it is curing, thus creating the cellular structure.

A balance between the two reaction rates is necessary in order to successfully create a polymer foam. If the foam's blowing reaction is much faster than the gelling, the gas bubbles will grow, coalesce, and break, ultimately collapsing the foam structure. This is primarily due to the polymer not having enough strength to support itself as it expands. Since the blowing reaction is occurring too rapidly, the polymerization needed for strength is not present. However, if the gelling reaction is much faster than the blowing reaction, the nucleation and growth of cell bubbles are suppressed. This results in the formation of closed cells, severe shrinkage, and pruning, where the foam loses its hardness and stiffness [14]. Thus, in most cases, the use of catalysts is critical to the formation of a balanced foam. Catalysts can increase the reaction rates of gelling, blowing, or both to help balance the foam formulation.

Additionally, additives such as blowing agents, surfactants, and chain extenders are used to control the overall properties of the foam. Blowing agents create the gas within the foaming reaction and assist in controlling the density of the foam [18]. Increasing the amount of blowing agent will cause the mixture to rise more, decreasing the density of the foam. Surfactants, meanwhile, help to emulsify the different component blends and stabilize the cell nucleation and growth by lowering the surface tension and viscosity of the mixture [18]. Chain extenders further increase the amount of crosslinking present in the polymerization stage, creating a polymer with a more uniform and interconnected network of chains [19]. Finally, other additives such as colorants, flame retardants, and antioxidants can be used to meet desired needs for esthetics, reduced flammability, and resistance to light discoloration, respectively.

2.1.3 Foaming Process

The foaming process consists of four major stages: cell nucleation, cell growth, cell opening, and curing. First, cell nucleation occurs from high rpm mixing of all components in the formulation. Thorough mixing ensures that the components are blended into a homogenous mix and helps create very small nucleation sites in the form of tiny air bubbles. The second stage, cell growth, begins when the foaming reaction starts. The froth (mixture containing tiny bubbles) starts to expand due to the higher pressure within the bubbles, caused by the gas generated from the blowing reaction. The pressure inside each cell nuclei must therefore be higher than the opposing forces due to gravity, surface tension, elasticity, viscosity, and friction to grow [18]. From the LaPlace relation shown as

$$\Delta P = \frac{2\gamma}{R_c} \tag{2.3}$$

where ΔP is the excess pressure inside the cell bubble, γ is surface tension of the liquid, and R_c is the critical radius of the cell bubble, it can be determined that small cells start with higher pressure and thus tend to coalesce into larger cells to lower their internal pressure.

As the cells grow they eventually collide with one another, distorting the cells' shape and begin to pull together the cell wall material that is in contact, to form the edges/struts. This is the onset of the third stage, cell opening. The cell walls that are in contact, exhibit extreme thinning and rupture due to a sudden decrease in viscosity and an increase in stress [18]. Meanwhile the struts remain unstressed and continue to pull material towards them. However, if the stress is too high, the foam can locally develop large cracks within its structure, known as splits, caused by the rupture of cell walls and struts altogether.

In the final stage, when the cells have ruptured, the foam equilibrates to ambient pressure. The trapped gas is vented and the foam relaxes, usually known as “Blow-Out,” which can be physically seen during the manufacturing process when gas bubbles escape and the foam essentially breathes, expanding and contracting as the gas escapes. Therefore, at the curing stage, the struts must be strong enough to support the foam structure, since the pressure is no longer there for support. Finally, the foams must be allowed to cure to allow the polymerization reaction to fully complete.

2.1.4 Foam Manufacturing

The two most common methods for manufacturing foams are slabstock and molded technique. The slabstock method allows for continuous pour of the foam mixture onto a conveyer belt, where the foam is only restricted laterally and is free to rise vertically on a paper substrate [19]. In Figure 2.2, the most common slabstock machine called Maxfoam is shown. The mixture must be poured uniformly across the width of the conveyer before the foam starts to rise. The foam thickness is then controlled by using a cut off blade to cut down the foam to uniform height after it finishes rising. The drawback of this method is that only rectangular samples can be made and cutting complex shapes from such pieces results in a large amount of wasted material.

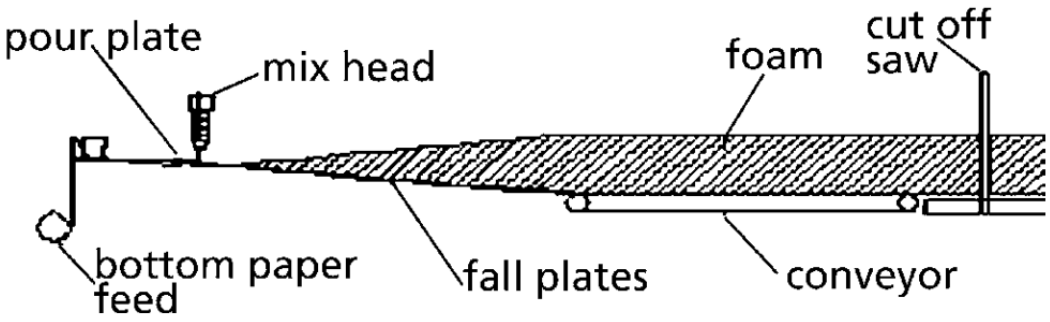


Figure 2.2: Slabstock foaming machine [19].

In the molded foam technique, the foam mixture is poured into a pre-heated metal mold. In Figure 2.3, a carousel molded foam machine is shown, where the mixture is poured into the mold and then allowed to rise and fill the mold before demolding the material for the next pour. In this method, complex shapes and net-shape products can be manufactured. However, the foaming time and demolding processes limit the amount of productivity [20].

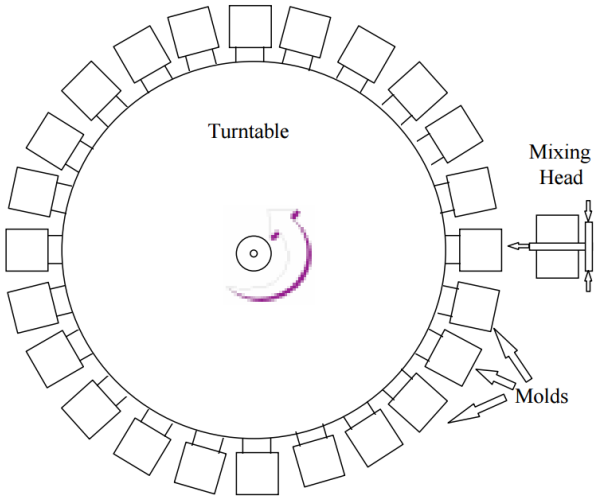


Figure 2.3: Carousel molded foam machine [20].

2.1.5 Mechanics of Foams

The compressive stress-strain behavior of foams exhibit the following three distinct regions (shown in Figure 2.4):

1. Linear elastic region
2. Stress plateau region
3. Densification region

In region 1, the linear elastic behavior is attributed to the bending of cell edges in open cell foams and stretching of cell faces in closed cell foams. Next, in region 2 the bending is followed by a continuous collapse of the cells through non-linear buckling and warping. This gives the foam the ability to collapse on itself, thereby increasing the amount of strain to failure under a constant stress [14]. Finally, in the densification region, the individual cells being to compress against each other, fully collapsing the foam. At this stage, the foam acts as a hard material due to the incompressibility nature of the solid polymer, dramatically increasing the stress over small strains. Regions 1 and 2 provide the foams with the energy absorption capabilities by undergoing large deformations under low stresses. Altogether, this makes foams very attractive for impact applications, since they can dissipate the impact energy through deformation, reducing the impact force or stress that gets transmitted.

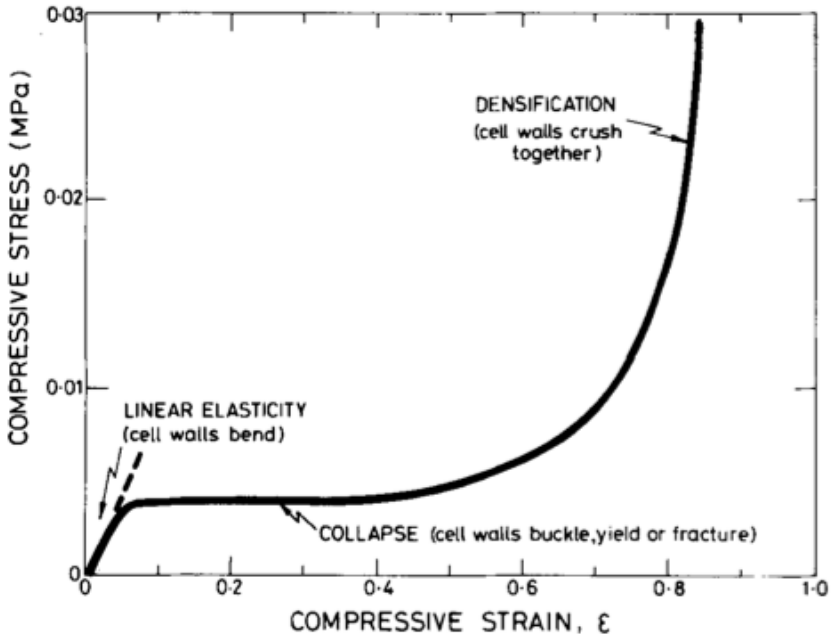


Figure 2.4: Typical compressive stress-strain curve for cellular materials [14].

The mechanical behavior of foams largely depend on their relative density, expressed as

$$\rho^* = \frac{\rho_f}{\rho_s} \tag{2.4}$$

where ρ_f is the density of the foam and ρ_s is the density of the solid polymer. Typical relative density values in foams can range anywhere between 0.01 and 1. Ashby and Gibson [14] observed that the Young's modulus and plateau stress increase with increasing relative density, while the densification strain decreases, with increasing relative density. Additionally, from a geometric perspective they determined that the foam properties can be related to the relative density as follows

$$\frac{E_f}{E_s} = C_1(\rho^*)^n \quad \text{(Elastic Modulus)} \tag{2.5}$$

$\frac{\sigma_{pl}}{E_s} = C_2(\rho^*)^n$ (Plateau Stress) (6)

where$E_f$is the Young's modulus of the foam, E_s is the Young's modulus of the solid polymer, σ_{pl} is the foam's plateau stress, C_1 and C_2 are fitting constant, while n is 2 for open cell foams and 3 for closed cell foams. Therefore, when designing with foams, the relative density must be taken into careful consideration in order to obtain the desired behavior.

Other factors that influence the mechanical behavior of foams include strain rate, temperature, and air damping effect. The viscoelastic nature of the solid polymer—discussed later in the polymer background section—from which the foams are made of, give rise to the strain rate and temperature dependent behavior. Additionally, at higher strain rates, the air dampening effect within the foam provides a larger contribution to the overall stiffness of the foam [14].

2.1.6 Constitutive Modeling of Foams

Ogden's Hyperfoam model is typically used to model the hyperelastic compressive and shear behavior of flexible polymer foams. The strain energy density function is given by

$$U = \sum_{i=1}^{N} \frac{2\mu_i}{{\alpha_i}^2}\left[{\lambda_1}^{\alpha_i} + {\lambda_2}^{\alpha_i} + {\lambda_3}^{\alpha_i} - 3 + \frac{1}{\beta_i}\left({J_{el}}^{-\alpha_i\beta_i} - 1\right)\right] \quad (2.7)$$

where μ, α, and, β are fitting constants which are temperature and density dependent, λ_i are the principal stretch ratios, and J_{el} is the elastic volume ratio given by the product of the principal stretch ratios. Foams under uniaxial compression and simple shear can be assumed to have a Poisson's ratio and lateral stretch ratios of zero due to the foam collapse [21]. Under the condition of the previous assumptions, the uniaxial compressive stress and shear are given by

$$\sigma_2 = \frac{\partial U}{\partial \lambda_2} = \frac{2}{\lambda_2}\sum_{i=1}^{N}\frac{\mu_i}{\alpha_i}\left[{\lambda_2}^{\alpha_i} - {J_{el}}^{-\alpha_i\beta_i}\right] \tag{2.8}$$

$$\sigma_s = \frac{\partial U}{\partial \gamma} = \sum_{j=1}^{2}\left[\frac{2\gamma}{2({\lambda_j}^2-1)-\gamma^2}\sum_{i=1}^{N}\frac{\mu_i}{\alpha_i}\left({\lambda_j}^{\alpha_i}-1\right)\right] \tag{2.9}$$

where γ is the shear strain and λ_j are the two principal stretch ratios. Materials with high coefficient values are stiffer than those with lower coefficient values [21]. Using Equations (2.8) and (2.9), the stress-strain behavior of flexible foams under compression and shear appear to fit very well with the Hyperfoam model as shown in Figure 2.5.

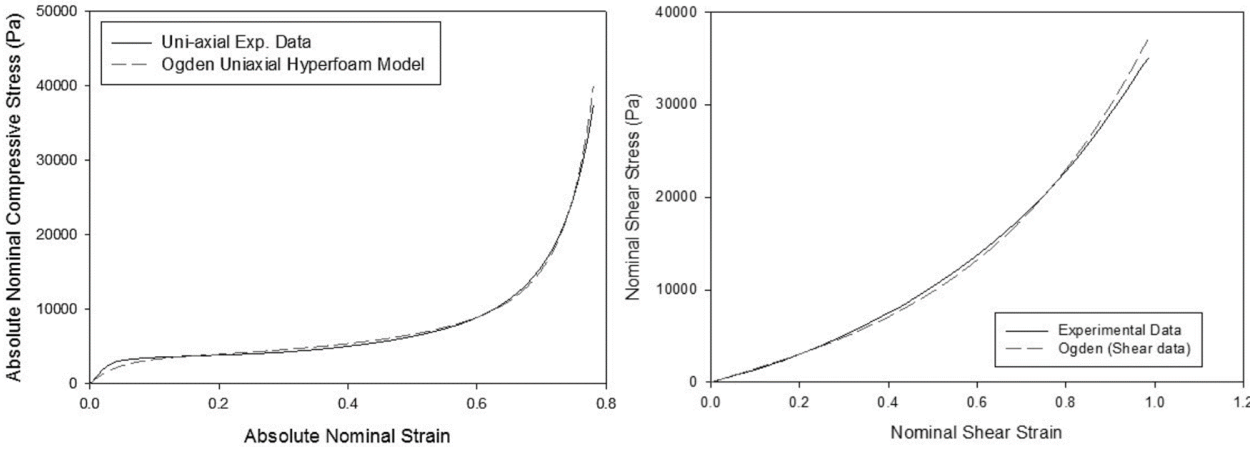


Figure 2.5: Comparing Hyperfoam model with experimental data in (Left) compression (Right) simple shear [21].

The viscoelastic response of flexible polymer foams is usually modeled with a Prony series fitted from the relaxation behavior. Since the shear modulus dominates the viscoelastic behavior, the Prony series is represented as

$$G(t) = 1 - \sum_{i=1}^{N} g_i\left(1 - e^{\frac{-t}{\tau_i}}\right) \tag{2.10}$$

where g_i and τ_i are the fitting constants and represent the relaxation modulus and relaxation time, respectively. Equation (2.10) is then multiplied with Equation (2.9) to obtain the time dependent properties of the foam. Figure 2.6 clearly shows that adding the viscoelastic response to the hyperelastic model, the time dependent behavior in foams can be more accurately predicted.

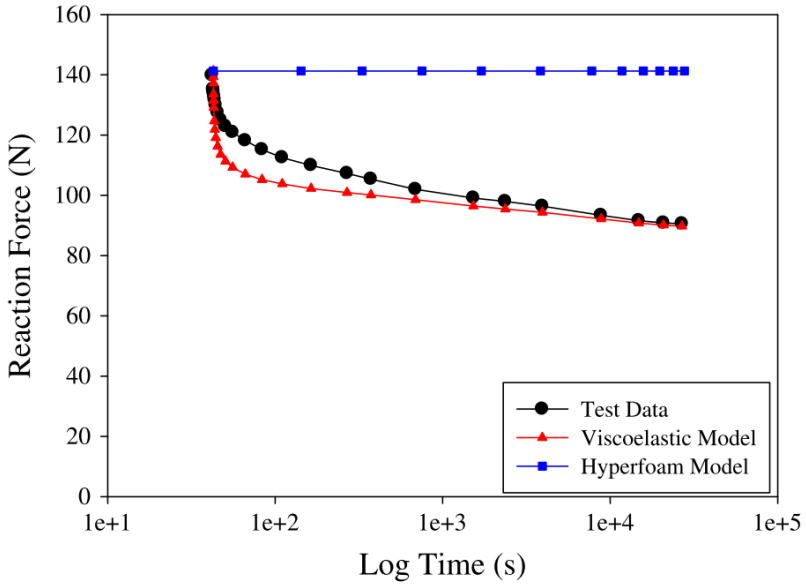


Figure 2.6: Stress relaxation data compared to viscoelastic model [22].

2.2 Polyurea: Review of the Literature

Currently, polyurea elastomers are used in a wide range of applications such as coatings, liners, and joint adhesives for protection against impact, ballistic penetration, abrasion, or corrosion [23-42]. This broad range of applications is due to the unique properties that polyureas exhibit. Polyurea elastomers have shown to have impact mitigation properties over a large range of frequencies and viscoelastic properties that strongly depend on pressure, temperature, and strain rate, along with improved moisture resistance, chemical resistance, and temperature stability over other elastomers [22-42]. Additionally, the micro phase segregation of hard and soft domains in

combination with the extensive hydrogen bonding in polyureas, grant it the ability to chemically tailor its mechanical stiffness, toughness, resiliency, and hardness [27]. Moreover, the rapid reaction time during the step-polymerization give polyureas gel times in minutes, allowing for fast curing times and to be used as spray-coatings.

2.2.1 Chemistry

Polyureas are formed by growth step-polymerization between an isocyanate group (-N=C=O) and an amine group ($-NH_2$) (see Figure 2.7). As a result, polyurea elastomers can refer to a large variety of polymers using different weight ratios and functional groups.

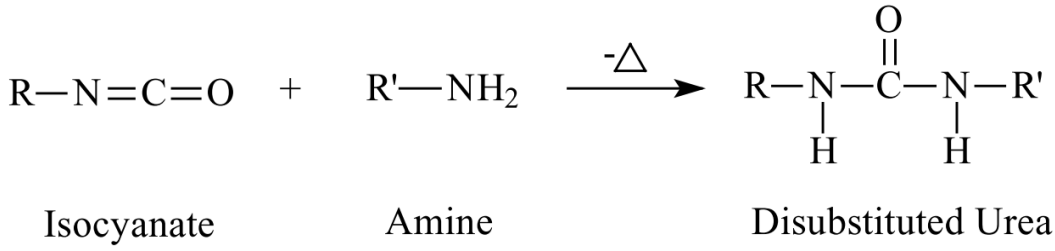


Figure 2.7: Polyurea formulation.

The chemical reaction yields a series of micro-phase segregated, thermo-plastically cross-linked hard and soft domains [23-25]. The hard domains consist of urea segments and R' functional groups from the amine, while the soft domains consist of R functional groups from the isocyanate. It is important to note that the structure of the hard domains is crystalline, not amorphous as in polyurethanes. The micro-phase segregation is governed by the Gibbs free energy of mixing:

$$\Delta G_m = \Delta H_m - T\Delta S_m \quad (2.11)$$

where ΔG_m is the free energy of mixing, ΔH_m is the enthalpy of mixing, and ΔS_m is the entropy of mixing. In such case, the high molecular weight of polyureas make $T\Delta S_m$ very small compared to ΔH_m , thus yielding a positive Gibbs free energy of mixing, driving the phase separation [23]. In Figure 2.8 the hard and soft segments in polyurea are shown through atomic force microscopy (AFM). The soft domains in polyurea elastomers have a low glass transition temperature (*Tg*), making the matrix of the polymer flexible at low temperatures. On the other hand, the hard domains have a high *Tg* and tend to thermo-plastically link together through hydrogen bonding, creating what are known as urea micro domains. Hence, the hard domains act similar to particle dispersion hardening in advanced composites [25]. This complex microstructure is attributed to the unique mechanical and chemical properties of polyureas.

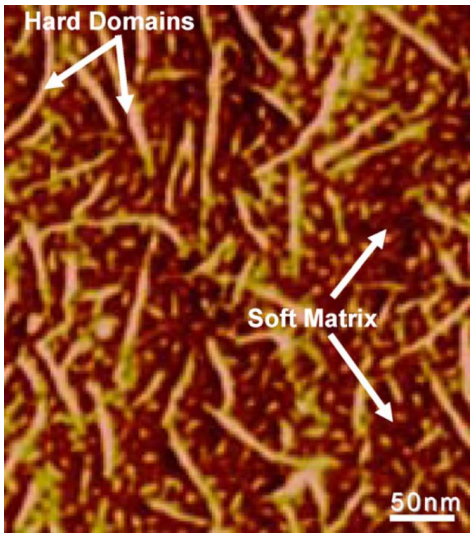


Figure 2.8: AFM of polyurea film [25].

The stoichiometry ratio used in manufacturing of polyureas play a huge role in determining the amount of hard and soft domains. The volume fraction of hard domains increase with increasing isocyanate content, altering the microstructure and properties of polyurea. The percent stoichiometry used is often referred as the isocyanate index or simply, index. Mixing the

components in a 1:1 stoichiometry ratio (100% stoichiometry) indicates an index of 100. To determine the weight ratios needed for amine to isocyanate, the following two equations are used to calculate the desired weight ratios for a given index value (or percent stoichiometry):

Equivalents of Isocyanate = [(Equivalents of Amine) * (Isocyanate Index)] / 100 (2.12)

Where

Equivalents = Parts/Equivalent Weight (2.13)

The most commonly used starting materials to form polyurea elastomers are Isonate® 143L (modified Methylene Diphenyl Diisocyanate (MDI) made by The Dow Chemical Company) and Versalink® PI000 (oligomeric diamine made by Air Products and Chemicals, Inc.). Additionally, a 4:1 amine to isocyante weight ratio is used for 100% stoichiometry (index of 100). This results in a polyurea containing a volume fraction of 36% hard domains and a density of 1073 kg/m^3 [23-42]. Unless it is stated otherwise, any further mention of polyurea will refer to Versalink® PI000 and Isonate® 143L with weight ratio of 4:1.

2.2.2 Mechanical Behavior of Polyurea

Fragiadakis et al. [25] showed that the stress-strain behavior of polyurea is dramatically different under quasi-static tension for different stoichiometric indexes **(**see Figure 2.9). The stoichiometric ratios affect the amount of hard to soft domains, the degree of cross linking, phase separation, and hydrogen bonding between urea micro-domains, resulting in a drastic change in mechanical properties [25]. Moreover, Choi et al. [26] found that polyurea yields beyond the initial linear

response due to permanent rearrangement dominated by soft segments under quasi-static strain rates.

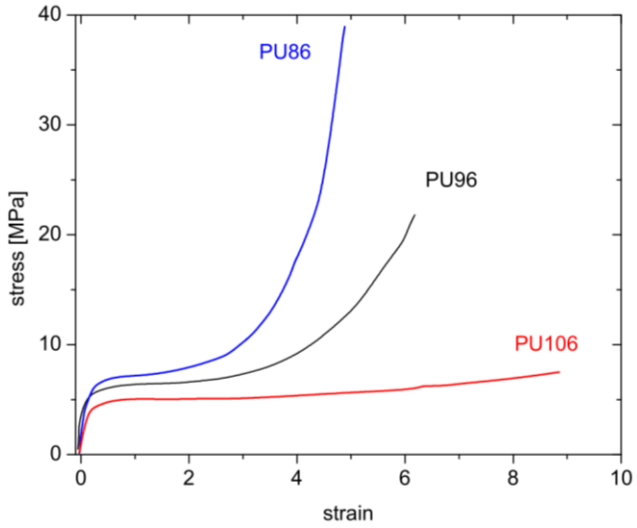


Figure 2.9: Stoichiometric effect on the stress-strain behavior of polyurea ($\dot{\varepsilon} = .06s^{-1}$)[25].

Holzworth et al. [27] further showed that through dynamic mechanical analysis (DMA), the complex modulus of polyurea, which measures both the elastic and viscous response, was highly dependent on stoichiometric index. However, the glass transition temperature of polyurea were approximately -50˚C for all samples, independent of stoichiometry used. The complex modulus is expressed as:

$$E^* = E' + iE'' \tag{2.14}$$

where E' is the storage moduli (elastic response) and E'' is the loss modulus (viscous response). Both the storage and loss moduli were found to be constant below the Tg and increase with increasing stoichiometric ratio above the Tg as shown in Figure 2.10. Therefore, the index used in

the formation of polyurea and the temperature at which the loading occurs, plays a crucial role in both the elastic and viscoelastic response [27, 28].

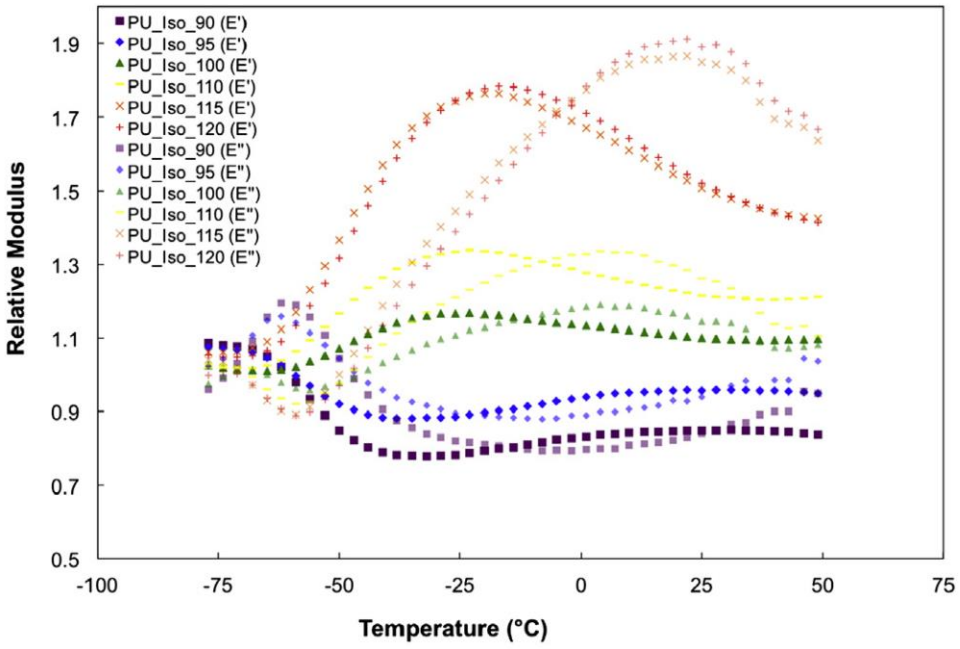


Figure 2.10: Storage and loss moduli for polyurea with varying index (1 Hz) [27].

As in most viscoelastic polymers, two important factors that affect the mechanical behavior of polyurea is the applied pressure and strain rate. Yi et al. [29] conducted unconfined and confined compression tests on polyurea under quasi-static strain rates. The unconfined polyurea samples displayed highly non-linear strain rate dependent elastic behavior, hysteresis during unloading, and cyclic softening. Meanwhile, the confined samples under hydrostatic pressure displayed an almost strain rate insensitive linear elastic behavior, increased stiffness response, and negligible hysteresis (see Figure 2.11). Moreover, Amirkhizi et al. [30] showed that the increase in stiffness when an external applied pressure is imposed on polyurea was also present at high strain rates through confined Split Hopkinson Pressure Bar (SHPB) experiments. The hydrostatic pressure on

polyurea make it more difficult for the soft domains to expand, making the overall system stiffer and follow a linear elastic behavior since it relies mostly on the hard crystalline domains [32].

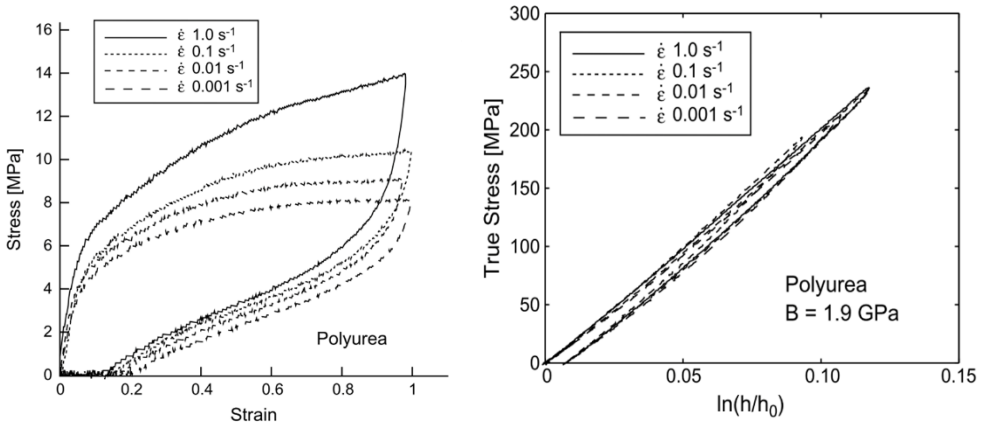


Figure 2.11: Stress-strain behavior of polyurea under (*Left*) no confinement *(Right*) confinement [29].

Furthermore, Roland et al. [31] examined the effect of strain rate on the tensile behavior of polyurea, while Yi et al. [29], Schim et al. [32], and Sarva et al. [33] examined the compressive strain rate behavior of polyurea. All showed that polyurea exhibits a strong rate dependent non-linear stress-strain behavior. Figure 2.12 and 2.13 show the strain rate dependent behavior of polyurea under tension and compression, respectively.

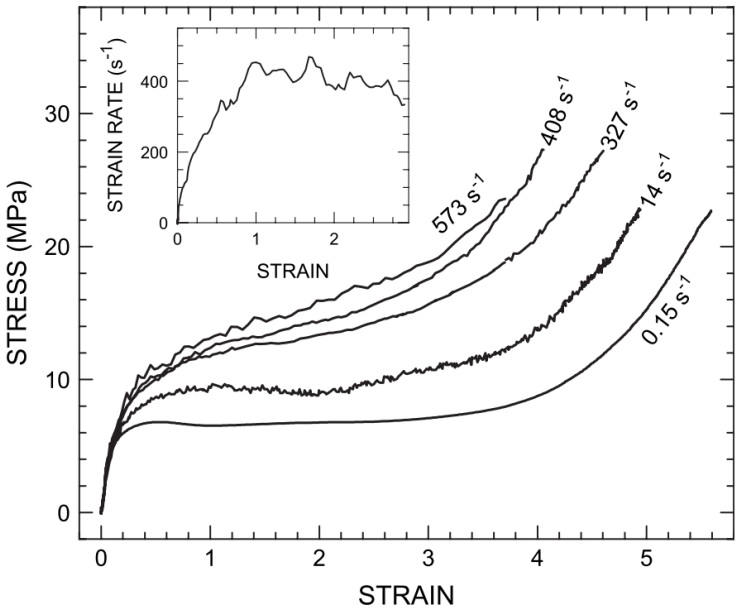


Figure 2.12: Strain rate effect on the tensile stress-strain behavior of polyurea [31].

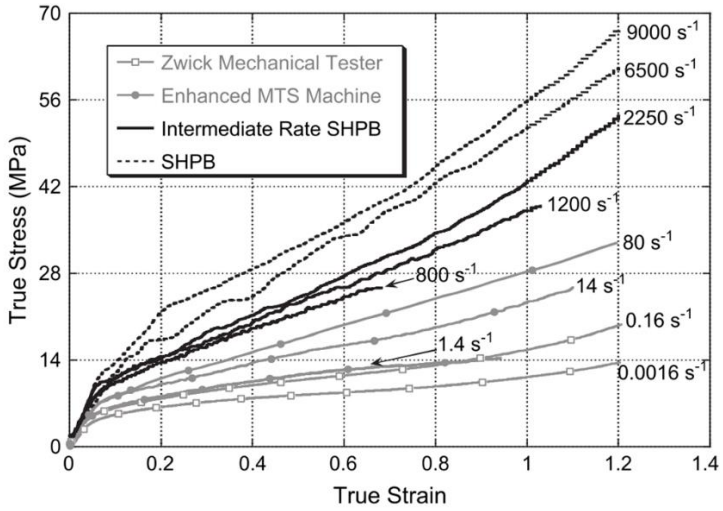


Figure 2.13: Strain rate effect on the compressive stress-strain behavior of polyurea [33].

The stiffness of polyurea was found to increase with an increasing strain rate. Additionally, the glass transition shift effect due to strain rate was observed, where at low strain rates (~10^0-10^3

s^{-1}) polyurea behaves in a rubber-like state, while at high strain rates (~10^3 s^{-1} or higher) it behaves in a glassy-like polymer [31-33]. Another interesting phenomenon observed in the stress-strain behavior of polyurea is the sharp increase in stress over small initial strains, which is not commonly seen in other polymers. The initial stiffness allows for polyurea to accommodate larger stresses over small strains, giving polyurea the ability to dissipate more energy than other polymers.

Furthermore, Jiao et al. [34] examined the shearing resistance of polyurea under high shearing rates with low and high hydrostatic pressures. Interestingly, the shearing resistance in polyurea was found to be insensitive to shearing rates (~10^5 s^{-1}), but highly sensitive to pressure, by increasing its shearing resistance with increasing pressure as shown in Figure 2.14. As a result, this allows polyurea to dissipate energy away from the target area through shear deformation under hydrostatic pressures [34]. Moreover, the spall strength or dynamic tensile strength of polyurea was determined to be 106 MPa under high (~10^6 s^{-1}) strain rates by Jaio et al. [35] and 93 MPa under ultra-high (~10^7 s^{-1}) strain rates by Youssef et al. [36]. Seeing that both values are relatively similar, indicates that increasing the strain rate above 10^6 s^{-1} will unlikely result in higher strength since polyurea is already deforming in a glass-like behavior [36].

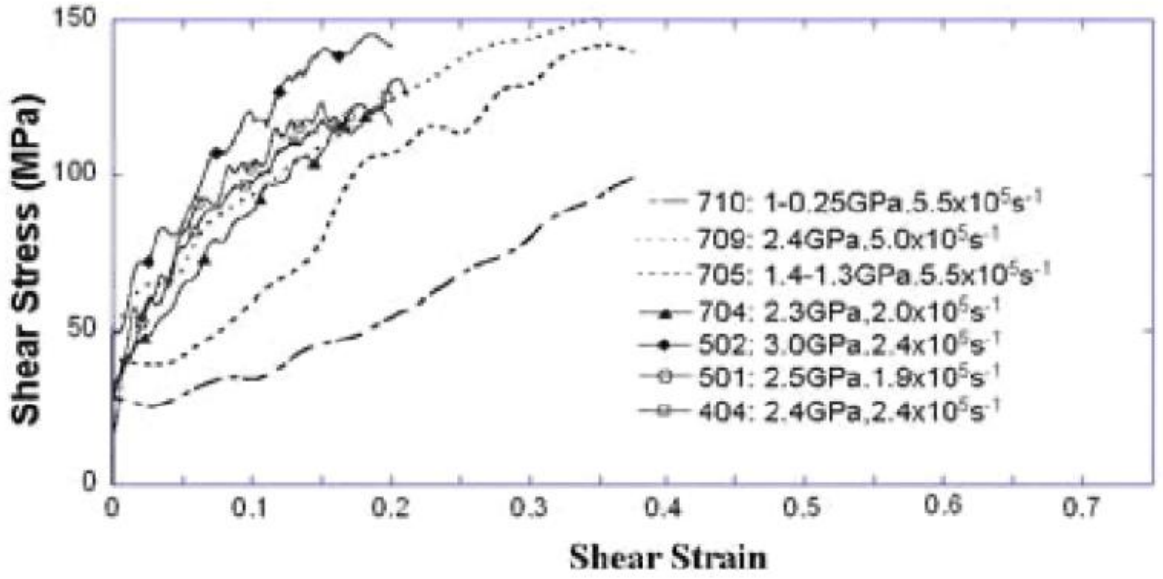


Figure 2.14: Shear response of polyurea under varying pressures and shearing rates [34].

2.2.3 Impact Properties of Polyurea

In this section, the impact mitigation properties of polyurea coatings are discussed. Amini et al. [37, 38] investigated the effect of polyurea coatings on the fracture resistance of steel plates at high strain rates, determining that the front or back surface placement of polyurea promotes different response as shown in Figure 2.15. When placing the polyurea coating on the front surface or the impact loading surface it induced fracture in the steel plate. However, placing the polyurea coating on the back surface, the shockwave dissipated and caused no rupture to the steel plates. The fracture response of the steel plate when the polyurea is placed on the front surface is attributed to the high pressure wave that increases the polyurea's stiffness and creats a better impedance match between polyurea and the steel plate, allowing the shock wave to reach the steel plate and fracture it [37].Conversely, when polyurea is placed on the back side, the steel plate takes the initial shock

loading while the remaining stress is dissipated by the viscoelastic response of the coating via glass transition shift at high strain rates and shock wave dispersion through shear deformation [37,38].



Figure 2.15: Steel-polyurea bilayer specimens under pressure-pulse experiments (*Top*) Polyurea on the front surface (*Bottom*) Polyurea on the back surface [37].

Grujicic et al. [24] added that the temperature at which the impact occurs also determines the amount of energy dissipation in the polyurea coating. At temperatures much greater than the *Tg*, polyurea behaves in a rubber-like state, making it highly ductile and producing no noticeable energy dampening. However, if the temperature difference is minimal and still above the *Tg*, then polyurea goes under glass-like transformation, dissipating the impact energy in a viscous manner by spreading the impact force away from the target area through shear deformation [37-39].

Amini et al. [39] further showed through finite element analysis that the bonding between polyurea and steel substrates plays a huge role in the fracture resistance of the steel-polyurea bilayer. Afterwards, Jain et al. [40, 41] and Kim et al. [42], respectively, studied the dynamic tensile strength and dynamic fracture energy of composite/polyurea and steel/polyurea joints. The

findings reported that both the dynamic tensile and fracture strength of steel/polyurea joints were intrinsically higher when compared to the common high strength adhesive used in naval applications. Polyurea also showed exceptional adhesion when exposed to high levels of humidity, moisture, and temperature when compared to the current epoxies used in composite manufacturing [40-42].

Citron [43] further examined the use of polyurea liners to mitigate against dynamic impacts with impact durations ranging from 1-100 ms, by adding a thin polyurea sheet (1-3mm) to current foam systems in protective gear. This thin layer proved to lower the likelihood of injury by decreasing the transmitted forces felt in protective equipment such as football helmets, shoe soles, and hip-paddings. Gupta and Youssef [44] then optimized the bilayer system of polyurea sheets and foams by looking at the effect of thickness and polyurea placement within the foam system.

2.2.4 Modeling of Polyurea

Polyurea is often modeled by combining both the hyperelastic model for low strain rates and non-linear viscoelastic for high strain rates [45-51]. Li and Lu [48] proposed the use of the Ogden model for the unconfined hyperelastic properties given by:

$$\sigma = \sum_{i=1}^{n} \frac{2\mu_i}{\alpha_i} \left(\lambda^{\alpha_i} - 2\lambda^{-\alpha_i/2} + \lambda^{\alpha_i/4} \right) \tag{2.15}$$

where σ is the Cauchy stress in the loading direction, λ is the principal stretch ratio in the loading direction, and α and μ are parameters determined from experimental data. The non-linear viscoelastic model is usually represented as a Prony series (which was determined by the relaxation curve obtained by Knauss and Zhao [49]):

$$G_{ref}(t) = G_{\infty} + \sum_{i=1}^{n} G_i e^{-t/\omega_i} \quad (2.16)$$

where G is the relaxation modulus. By adding Equations (2.15) and (2.16) together, a rate-independent and rate-dependent model is used and shows good accordance with the experimental data, Figure 2.16.

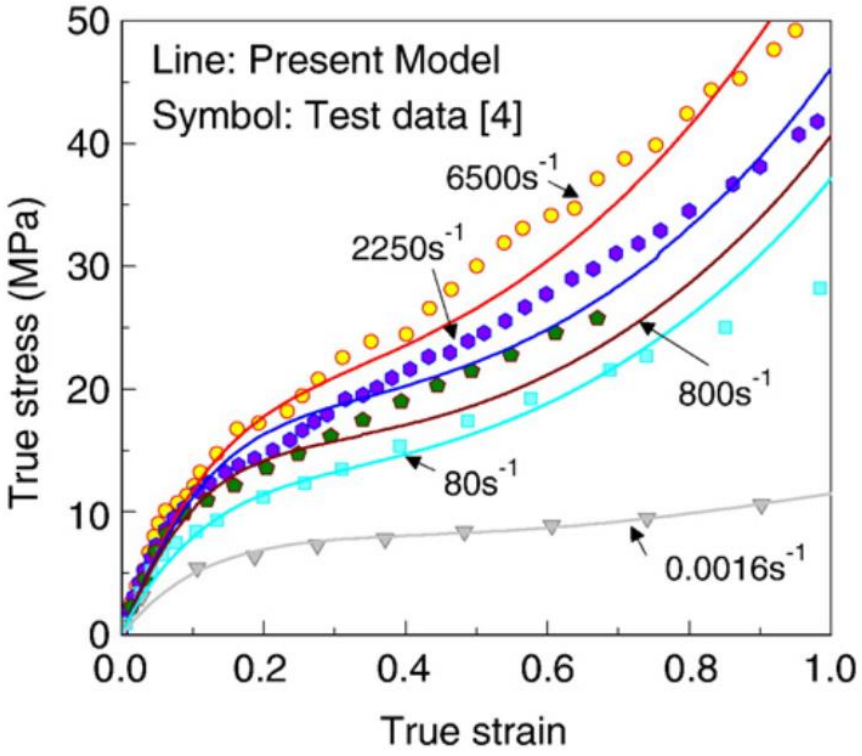


Figure 2.16: Li and Lua [48] model of polyurea behavior under varying strain rates.

Zhao et al. [50] further discovered that the time-temperature superposition (TTS) principle was applicable to polyurea for strains of the order of 3.8% or less and strain rates of up to 10^3 s^{-1}. Therefore, the viscoelastic properties of polyurea at various temperatures and strain rates can be obtained quasi-statically using time-temperature superposition shift. By using a ramp-time history to measure the relaxation data of polyurea samples at different temperatures, a master relaxation

curve was created [49]. Then, through the TTS shift process [50], the material's correction in modulus based on the temperature was deduced as a function of time. Figure 2.17 shows both the master relaxation curve and shift factor of function of time, respectively.

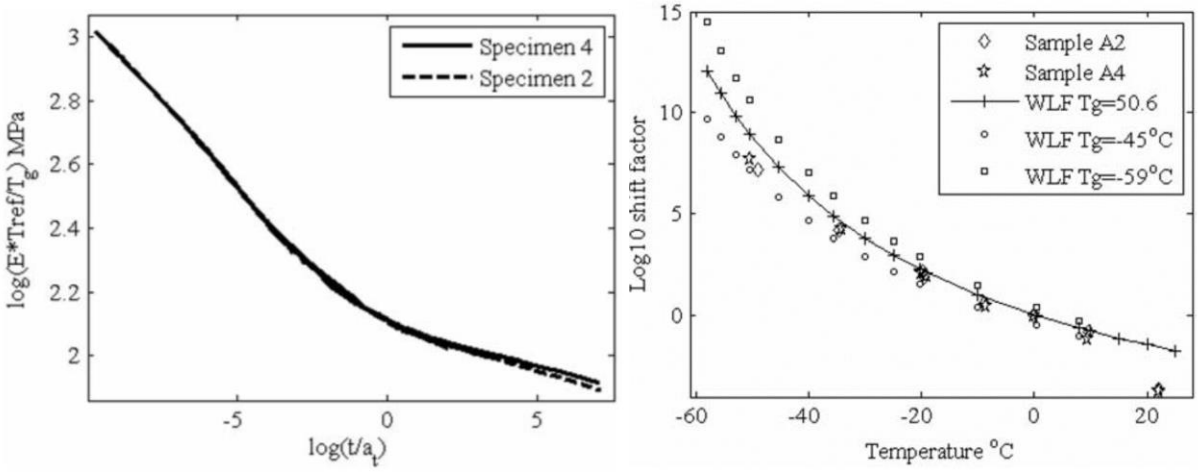


Figure 2.17: (*Left*) Master relaxation curve (*Right*) Shift factor as function of time [49].

Utilizing the Williams–Landel–Ferry (WFL) equation, the correction factor of polyurea based on temperature was determined to be

$$\log a_t = \frac{-8.86(T-T_S)}{101.6+(T-T_S)} \tag{2.17}$$

where a_t is the shift factor, *Ts* is the reference temperature defined as 50˚C above *Tg*.

Youssef and Gupta [51] extended the validity of using the TTS principle for polyurea for strain rates of up to 1.1×10^5 s^{-1}. The stress-strain behavior of polyurea obtained through the use of laser generated shockwaves was compared to that of a 2D FEM model. In the FEM simulation, polyurea was modeled in the same way as Zhao et al. [50] and Knauss and Zhao [49] did in their experiments. Youssef and Gupta [51] found that the TTS held for strain rates of up to 1.1×10^5 s^{-1},

for strains within the linear viscoelastic regime (see Figure 2.18**)**. This suggests that the high strain rate behavior of polyurea can modeled using data obtain under quasi-static conditions [51].

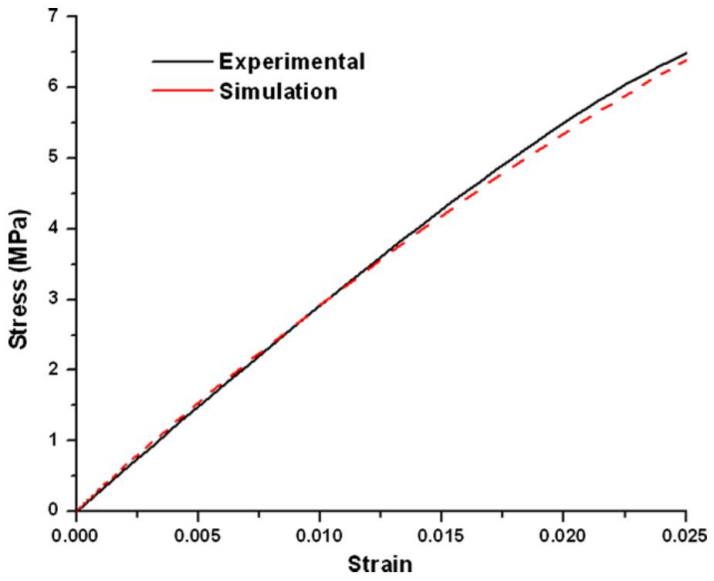


Figure 2.18: Comparison of experimental and modeled behavior of polyurea [51].

2.2.5 Concluding Remarks

The following summarizes the unique properties of polyurea:

1. The mechanical behavior of polyurea strongly depends on the stoichiometry, pressure, temperature, and strain rate.
2. Polyurea displays a highly non-linear strain rate dependent elastic behavior, hysteresis during unloading, and cyclic softening.
3. Polyurea exhibits a transition from rubber-like to glass-like behavior at strain rates of the order 10^3 s^{-1}.

4. The shearing resistance of polyurea is highly sensitive to pressure rather than shearing rate.
5. Polyurea has excellent impact mitigation and ballistic resistance due to glass transition shift at high strain rates, impedance mismatch, shock wave dispersion through shear deformation, and high incompressibility.
6. Polyurea displays superior adhesion properties under varying temperatures, relative humidity, and moisture.
7. Polyurea can be modeled using relaxation data through Prony series and TTS up to strain rates of $10^5 s^{-1}$.

Therefore, polyurea is an excellent candidate for foaming given its unique and superior properties over other elastomers.

CHAPTER 3

Tailoring the Rate-Sensitivity of Low Density Polyurea Foams through Cell Wall Aperture Size

3.1 Introduction

Elastomeric foams of varying densities are widely used in protective head and body gears and in a variety of mechanical, civil, and aerospace structures for protection against blast and impact loads [1-2]. Foams manage impact by undergoing large deformations under low stress by increasing the time over which the velocity of the incoming impact is arrested and by dissipating the impact energy through local viscoelastic or plastic crushing processes through bending, twisting, and buckling of the struts that form the skeleton of its structure [3-13]. The compressive stress-strain behavior of a typical viscoelastic or a plastic foam exhibits three distinct regions: (i) a linear elastic region associated with cell wall bending, (ii) a stress plateau region that results from continuous collapse of the foam's cell structure on itself through non-linear fully recoverable (viscoelastic foams) or irrecoverable (plastic foams) buckling of its struts, and (iii) a densification region where the already-collapsed cells begin to compress against each other to near full density, resulting in a steeply rising stress. The amount of energy absorbed or dissipated by the foam is roughly equal to the area under its stress-strain curve.

For a given foam thickness, which is typically constrained by the specific application, the design process reduces to determining the lowest density of the foam per unit volume that keeps the peak load below the injury threshold level without bottoming out. For head health applications, the peak transmitted stress must be kept below 1.5 MPa [14-15]. The manufacturing technology

has advanced significantly over the past two decades in that any polymer can be foamed into the desired density through control of process variables and by use of various surfactants, foaming and gelling agents. The industrial processes are also well developed to produce foams with *uniform* microstructures in large quantities at fairly low cost. Today foams are used in practically every industry. Despite their ubiquity and maturity, there are several areas where improvements in the foam technology can be made, especially those that pertain to impact applications, as discussed next.

Expanded polystyrene (EPS) based systems are lightweight (with densities on the order of 45-75 kg/m^3) and absorb impact energy through plastic crushing [9-11]. Because they are effective energy absorbers in small section thicknesses (less than 1"), they are widely used as liners in protective body and headgear systems, including commercial bicycle and motorcycle helmets. An advantageous property of EPS foams is the ability to keep the peak crushing stress below the injury threshold level by choosing an appropriate foam density. EPS72 with a density of 72 kg/m^3 is the most efficient in absorbing impact energy among all currently available foam systems at the stress level of 1.2 MPa [14]. A major drawback of EPS foams is that they do not recover after plastic crushing and therefore provide reduced protection during subsequent impacts which at times may occur in the same event. This single event constraint severely limits the use of EPS in sports.

Almost every current application utilizes foams with a *uniform* microstructure. Even with the choice of the lowest density these foams are not truly optimized. This is because the initial linear response and the plateau stress which determine the impact attenuation and momentum trapping properties of the foam depend strongly on the loading rate [3-13] which changes within the same impact event. The material strain rate is lower at the start of the loading as the foam cells start to collapse, and then builds up quickly during the densification process, and finally, reduces

significantly when the velocity of the impactor has slowed down substantially. One way to *further* optimize the foam's performance is to create a section with modulated stiffness or density to account for this varying material strain rate. Such a foam structure cannot be manufactured in a single low-cost manufacturing step. It would require lamination where foam layers of different density, stiffness, and thickness are stacked up in a specific order. In addition to being expensive, the lamination process is not easily scalable as required for production of high volume commodity products.

Finally, present viscoelastic foam pad systems are susceptible to temperature variations, becoming hard at cold temperatures and soft at high temperatures [17]. In both situations, the peak transmitted stress greatly exceeds the injury threshold design limit for injury. This is particularly true for high performance foams such as Poron-XRD that have their glass transition temperature, T_g, near 0°C and absorb energy through phase transformation. Ideal foam should have a T_g well below 0°C so that it can maintain its viscoelastic properties over a wide range of temperatures.

In this chapter, we present foams for impact applications that overcome the aforesaid shortcomings. First, they function effectively like foams with modulated stiffness and density even with their *uniform* microstructure. Second, they are made using polyurea (PU) with a T_g = -50°C and therefore able to maintain their ambient impact properties at low and high temperatures. Currently, PU elastomers are used in a wide range of applications for their unique impact mitigation capabilities, viscoelastic properties, moisture and chemical resistance, and thermal stability [29-44]. Finally, being viscoelastic, they recover fully after each impact, and quite remarkably, absorb more impact energy than EPS72 foam at strain rates greater than 2000 s^{-1} while still keeping the stress below the brain injury threshold level of 1.5 MPa. To our knowledge this

has never been accomplished by any viscoelastic foam. These properties are due to their unique microstructure and use of polyurea as the foaming polymer.

The foam comprises of large polyhedral cells (300 μm -500 μm) covered with perforated membranes with small apertures (20 μm-70 μm). This makes the foam strain rate sensitive as the rate at which the air escapes the cells through perforations depends upon the loading rate. Thus, even with their uniform microstructure, they behave effectively as an elastically modulated layered composite because the cells stiffen or soften in response to the changing loading rate within the same impact event. At lower strain rate, typically at the start of the loading event, big cells simply collapse with air escaping freely through tiny perforations. This limits excess buildup of stress like any other viscoelastic foam. As the loading proceeds, both strain rate and level of material stress increases. During this phase, the rate at which the air escapes the cells cannot catch up with the rate of loading. Consequently, the air that remains inside each cell acts to stiffen the cell while the air that escapes adds to viscoelastic damping. Finally, when the impactor velocity has substantially reduced and the strain rate has dropped, the remaining undeformed cells collapse slowly, giving plenty of time for the air to escape freely through tiny perforations. Each cell thus acts like a time-dependent viscoelastic damper on the microstructural scale. Therefore, our foams are able to manage the varying material strain rate that occurs within the same loading event without the need to modulate the material density or stiffness. In addition to the microstructure, energy is also dissipated by dynamic bending, twisting and rotation of the cell walls during impact like any other foam. However, in our foams, cell walls are made using the polyurea elastomer which itself is capable of absorbing the impact energy through sliding and stretching of its flexible molecular chains. The micro-phase segregation of hard and soft domains along with extensive hydrogen bonding present within the polyurea structure also grants it the ability to chemically tailor its

mechanical toughness, resiliency, and hardness [23-27]. The polyurea chemistry chosen for the foams presented here was already optimized for maximum energy dissipation [29-44].

The combined benefits of temperature stability and rate sensitivity over commercial foams was further demonstrated by integrating PU foams as liners into football and motorcycle helmets (Chapter 4) and as inserts into athletic shoes (Chapter 5). This chapter demonstrates the remarkable strain rate sensitive property of the foams by presenting stress-strain characteristics for two types of samples with very similar densities (280 kg/m^3 and 300 kg/m^3) but very different cell structures, under low ($\leq 10^{-1}$ s^{-1}), intermediate (10^1-10^2 s^{-1}), and very high ($\geq 10^3$ s^{-1}) strain rates.

3.2 Material Preparation and Characterization

Open cell polyurea foams were fabricated by mixing modified Methylene Diphenyl Diisocyanate (MDI) compound with oligomeric diamine with different mix ratios. Polyureas of this stoichiometry are known to have behaviors within the viscoelastic regime [29-44]. The mixture was stirred using a high rpm electric stirrer to introduce small air bubbles to create froth. Next, the PU mix was poured into a 90 mm x 90 mm x 90 mm mold and placed inside a vacuum oven that was preheated to 80 °C. The oven was slowly evacuated until a desired foam height was reached. The vacuum was then maintained at that pressure for 10 minutes so that it could support the cellular structure of the foam during curing. The density of the foam was controlled by adjusting the amount of air and frothing. To demonstrate the strain rate sensitive property, two types of samples with very similar densities (280 kg/m^3 and 300 kg/m^3) but very different microstructures were prepared using the same polyurea mix with a density of 1070 kg/m^3. Hereinafter these samples are referred to as PU280 and PU300, respectively. Figure 3.1 shows the scanning electron micrographs of these foams. Both foams consist of open spheroid cells with wall apertures (perforations). The

nominal cell size for both foams is about 550 μm, which is consistent with their similar densities. The wall aperture size is however substantially different, being 66 μm in PU280 and 20 μm in PU300. With their vastly different aperture sizes, these samples are ideal for demonstrating their critical role in making the foams strain rate sensitive in the manner discussed earlier.

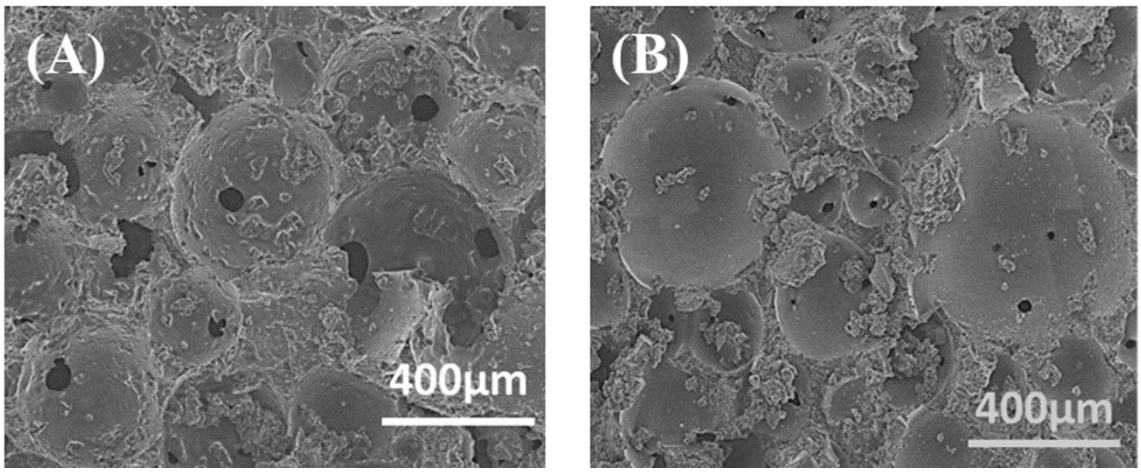


Figure 3.1: Scanning electron micrographs of the microstructure of (A) Polyurea Foam PU 280, and (B) polyurea foam PU300.

Expanded polystyrene (EPS) was chosen as a reference material to compare the behavior of PU foams especially at very high strain rates. EPS72 discs of 72 kg/m^3 density were obtained from the O'Neal Company. The SEM micrograph of EPS72 in Figure 3.2 shows that it comprises of uniformly distributed irregular polyhedral closed cells with a nominal cell size of 160 μm.

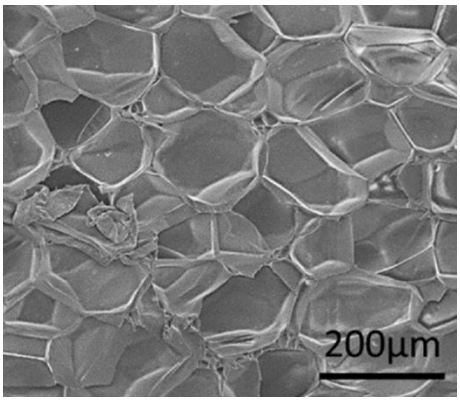


Figure 3.2: Scanning electron micrograph of the microstructure of expanded polystyrene foam EPS72.

3.3 Experimental Techniques

3.3.1 Low and Intermediate Strain Rate Testing

Low strain rate ($\leq 10^{-1}$ s^{-1}) compression tests were conducted using an Instron Micro-Tester (Model 5942) equipped with a 2 kN load frame. For these tests, disc samples of 28 mm nominal diameter and 10 mm thickness were cut from a large molded block. Samples were then compressed under stroke-control with cross-head velocities of 2.4, 24, and 240 mm/min in order to examine the material response over a range of quasi-static strain rates. These cross-head speeds yielded strain rates of $0.004s^{-1}$, $0.04s^{-1}$, and $0.4s^{-1}$, respectively. Force-displacement data obtained from the machine at each strain rate was converted into the stress-strain data using the sample dimensions.

Intermediate strain rate (10^{1}-10^{2} s^{-1}) compression tests were carried out using an Instron DynaTup (Model 8250) drop-weight impact tester. Specimens with aforesaid dimensions were tested by placing them on a 45 mm-diameter flat force plate and impacted using a 5.5 kg balanced mass attached to a 75 mm-diameter flat stainless steel indenter head. The transmitted force was measured using a force transducer (Kistler Instruments, Model 9041A) with a full scale output of

90 kN and sensitivity of 4.3 pC/N. Impact energy was varied by changing the drop height of the indenter head. The displacement of the top sample surface during impact was also measured using high speed photography. The recorded force-displacement data was converted into engineering stress-strain characteristics using the initial sample dimensions. The strain rate ($\dot{\varepsilon}$) was calculated using:

$$\dot{\varepsilon} = {d\varepsilon}/{dt} = \frac{d}{dt}\left(\frac{l-l_o}{l_o}\right) = \frac{1}{l_o}\left(\frac{dl}{dt}\right) = \frac{v}{l_o} \tag{3.1}$$

where v is the impact velocity and l_o is the specimen thickness. It should be noted that a constant strain rate is not attained in this experiment as the velocity of the falling mass is reduced during foam compression. However, the strain rate computed using the initial impact velocity and that calculated by differentiating the strain profile yielded only a 10% difference below 60% strain. Therefore, the stress-strain response up to 60% strain can be considered constant for all practical purposes. Data presented in this chapter were at strain rates of 100 s^{-1} and 200 s^{-1} are reported here.

3.3.2 High Strain Rate Testing

High strain rate ($\geq 10^3$ s^{-1}) deformation of foam samples was accomplished using a modified split-Hopkinson Pressure Bar (SHPB) setup at Caltech. The SHPB is perhaps the most widely used experimental apparatus for characterization of material behavior at strain rates greater than 10^3 s^{-1}. In this experiment, a sample is placed between incident and transmitted bars. A stress wave is generated inside the incident bar by striking its one end with a gas gun-propelled projectile bar. Due to the impedance mismatch between the sample and the incident bar, reflected and transmitted waves are generated when the incident wave strikes the sample. The incident, reflected, and transmitted waves are recorded using strain gauges and this information is used to generate the

stress-strain characteristics for the sample. Operation of the standard SHPB setup and related signal processing are well documented in the literature [52-56] so it will not be covered here. We will only discuss the modifications that were necessary for testing samples with very low density, modulus, strength, and acoustic impedance.

To ensure attainment of the dynamic equilibrium conditions [55], foam discs of 16.60 mm diameter and 1.88 mm thickness were used for testing. These were cut from the center of a large molded foam block. To enhance the amplitude of the transmitted signal, a hollow transmitted bar with an epoxied press-fit end cap having an outer diameter of 19.02 mm and an internal diameter of 17 mm was used. The striker and incident bars were solid as in the standard SHPB setup. Use of the hollow bar increased the transmitted wave amplitude by an order of magnitude. This appears to be an attractive technique to enhance the signal to noise ratio when studying materials that have both low strength and low impedance. In order to achieve mechanical equilibrium conditions in the very low strength foam samples it became necessary to shape the incident pulse as the standard square pulse of the SHPB setup resulted in premature failure of the sample prior to the establishment of the dynamic equilibrium conditions. The pulse shaper system used here consisted of a plastic polymer disc, multiple sheets of thin paper, and vacuum grease in accordance with previous studies [55-56]. Through experimentation, an incident pulse with a rise time longer than the time required to achieve dynamic equilibrium within the sample, was generated. The pulse shaping also alleviated any concerns regarding the effect of the endcap that was used on the hollow transmitted bar on perturbing the one-dimensional wave propagation conditions that are typically assumed in the SHPB experiments. High frequency filters were also used in signal processing to further alleviate this concern. Because of the aforesaid changes, including the use of the hollow transmitted bar, equations used to obtain the mechanical response of the deformed foam samples

differed from those derived by Kolsky [53]. For a sample of length L and cross-sectional area A_S, the stress (σ) and strain (ε) histories in the sample were determined using [56]:

$$\sigma(t) = \frac{A_T}{A_S} E \varepsilon_T(t) \tag{3.2}$$

$$\varepsilon = \frac{c_0}{L}\left(1 - \frac{A_I}{A_T}\right)\int_0^t \varepsilon_I(\tau)d\tau - \frac{c_0}{L}\left(1 + \frac{A_I}{A_T}\right)\int_0^t \varepsilon_R(\tau)d\tau \tag{3.3}$$

where, $c_0$is the wave speed in the bar, E is the elastic modulus of the bar material, $A_I$and A_T are the cross-sectional area of the incident and transmitted bars respectively, and ε_I and ε_T are the strain gauge-recorded stress pulse signals in the incident and transmitted bars, respectively.

3.4 Results

3.4.1 Low and intermediate strain rates

The stress-strain behavior of PU280, PU300, and EPS72 foams at low (0.004, 0.04, and 0.4 s^{-1}) and intermediate (100 and 200 s^{-1}) strain rates are shown in Figures 3.3, 3.4, and 3.5, respectively. Figure 3.6 displays the plateau stress and energy absorption as a function of strain rate. The plateau stress $\sigma_{(25\%)}$was measured as the peak stress at 25% compression and the energy absorption E was calculated using the widely acceptable method for foams [14] in terms of the densification strain $\varepsilon_D$as:

$$E = \sigma_{(25\%)}\varepsilon_D. \tag{3.4}$$

With increasing strain rate, all foams displayed an increase in the Young's modulus and plateau stress and a decrease in the densification strain. At low strain rates, this strain rate sensitivity is essentially controlled by the rate-dependent mechanical properties of the solid cell wall material. Following Ashby and Gibson [14], this can be modeled using a phenomenological relation relating

the stress σ to the relative density $\left(\rho_f/\rho_s\right)$ of the foam through two strain rate-dependent fitting constants *K* and *n* as

$$\sigma = KE_S\left(\frac{\rho_f}{\rho_S}\right)^n \tag{3.5}$$

where E_S and ρ_S are the Young's modulus and density of the solid polymer, and ρ_f is the density of the foam. The pair of fitting constants (*K*, *n*) for the PU foams presented here were determined to be (0.0172, 1.072), (0.0175, 1.032), (0.130, 0.711), (0.109, 1.667), and (0.961, 2.891) at strain rates of 0.004 s^{-1}, 0.04 s^{-1}, 0.4 s^{-1}, 3000 s^{-1}, and 5000 s^{-1}, respectively.

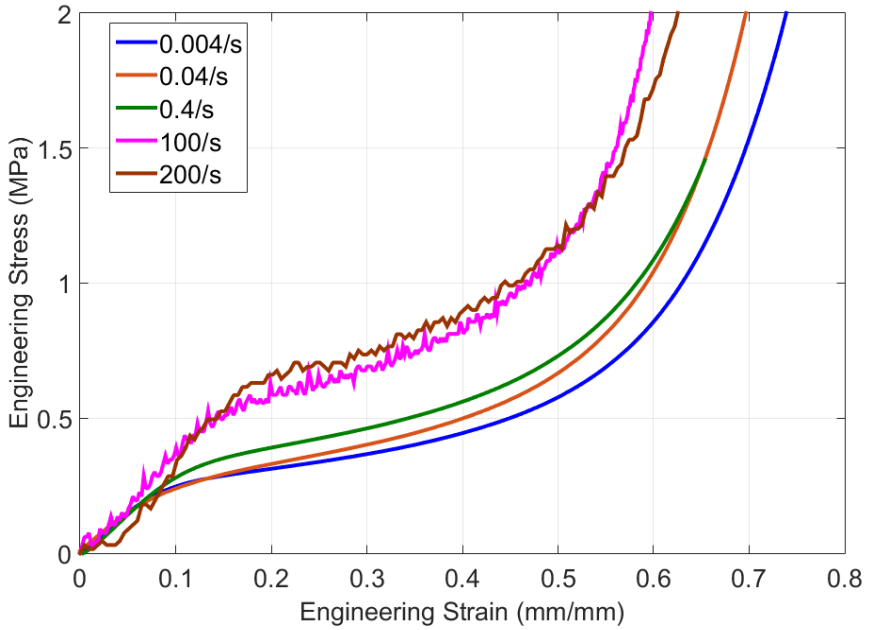


Figure 3.3: Stress-strain behavior of polyurea PU280 foam at quasi-static and intermediate strain rates.

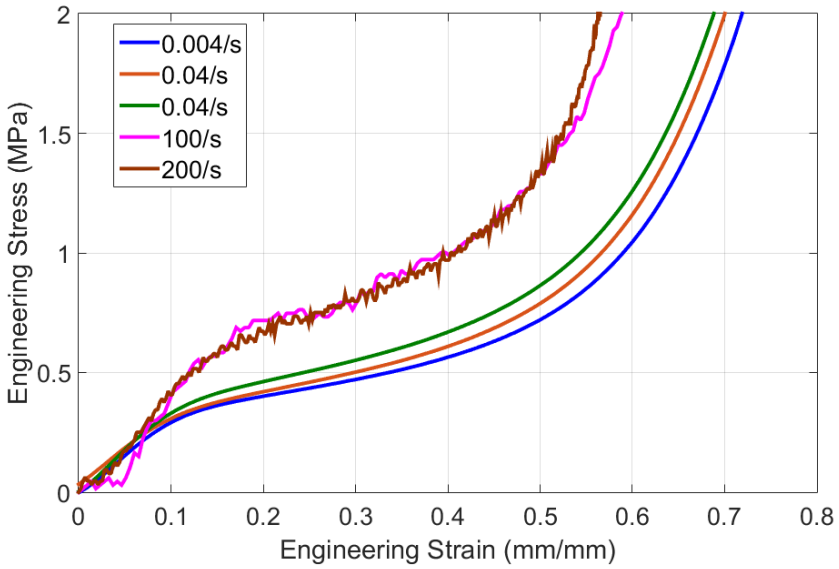


Figure 3.4: Stress-strain behavior of polyurea PU300 foam at quasi-static and intermediate strain rates.

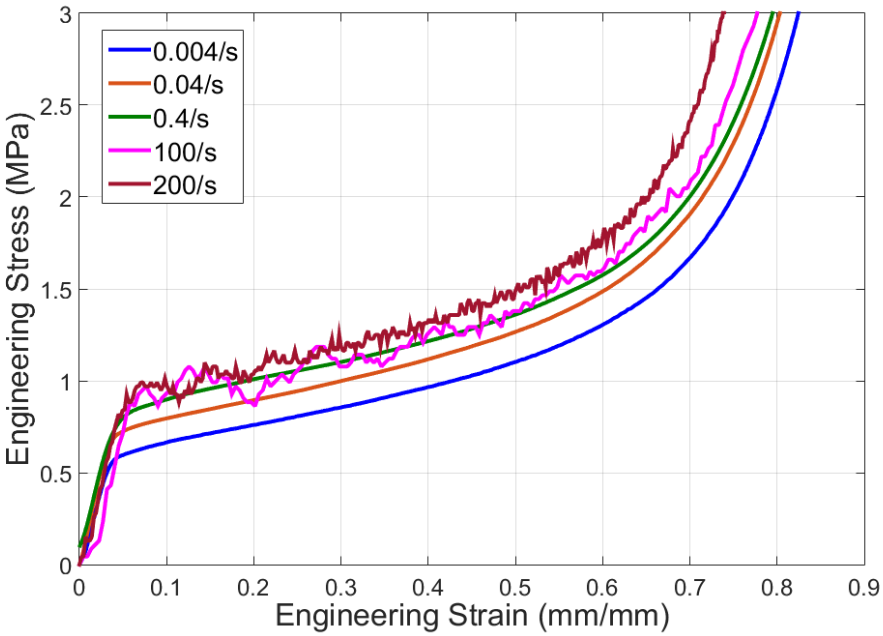


Figure 3.5: Stress-strain behavior of expanded polystyrene EPS72 foam at quasi-static and intermediate strain rates.

Figures 3.3-3.5 show that as the strain rate was increased into the intermediate range (100 s^{-1}-200 s^{-1}), PU foams exhibited a drastic increase in their stiffness and plateau stress whereas EPS72 displayed a fairly rate insensitive behavior. In the PU foams, this behavior partly stems from the very high strain rate sensitivity of the solid polyurea that forms their cell structure but more importantly it is related to the size of the cell wall apertures. The aperture size of PU280 (66 μm) and PU300 (20 μm) are quite different. They have negligible effect on their overall compressive stress-strain behavior at low rates of deformation ($\leq 10^{-1}$ s^{-1}) since the air can easily move out of the foam during quasi-static compression. At intermediate rates (10^{1}–10^{2} s^{-1}), however, the work required to drive the air out from the center of the foam cells through the small apertures starts to contribute to the strength of the foam. This is because the rate at which the air can escape from these tiny perforations is slower than the rate of loading which then leaves the air inside the cells, strengthening them, much like air or gas trapped inside a closed-cell foam system. This is the first time that the strain rate sensitivity has been imparted in such low density foams. Most low density foams are strain rate insensitive given their very large cell size (~500 μm) [14]. Here, the strain rate sensitivity is accomplished by having tiny apertures (~ 20 μm) while maintaining the low density through large cell sizes, similar to their predecessors. The stress-strain response of PU280 and PU300 foams at low and intermediate rates of deformation are comparable since both have similar relative density and their aperture sizes display similar degree of strengthening as both are big enough to dispel air that is needed to establish equilibrium with the rate of loading. This however changes at very high strain rates as discussed in the next section where PU300 displays a much stiffer response because of its substantially small aperture size. This strain rate strengthening mechanism is absent in the EPS as it has a closed-cell microstructure. The air trapped within the cells only contributes to the strength of the foam, independent of the strain

rate [14]. At these strain rates, EPS72 absorbs more energy per unit volume than both PU foams (Figure 3.6b) while maintaining its plateau stress below the brain injury threshold limit of 1.5 MPa [14-15]. Thus, plastic crushing is more efficient in absorbing energy than viscoelastic dissipation at these strain rates. This disadvantage of the viscoelastic foams is however overcome by the ability of the foams to recover fully after each impact, which is a requirement in protective head and body gears in sports.

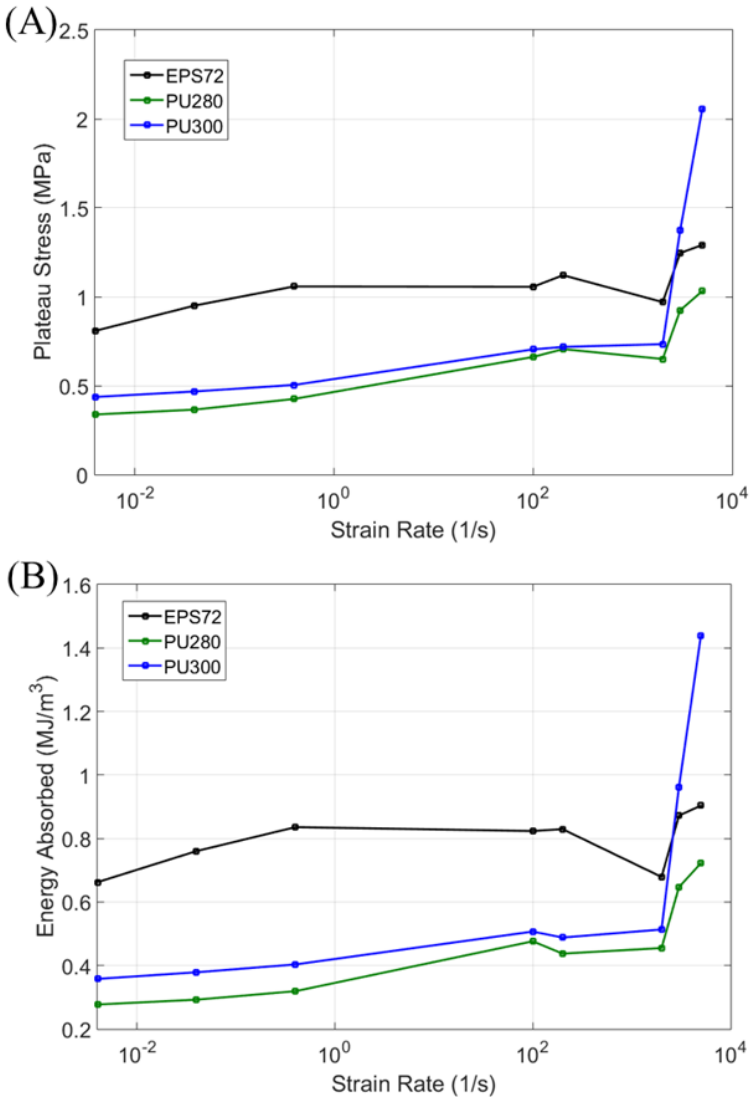


Figure 3.6: The plateau stress and energy absorption as a function of strain rate for expanded polystyrene EPS72 foam and polyurea foams PU280 and PU300.

3.4.2 High strain rate response

The typical stress-strain behavior of PU280, PU300, and EPS72 at high strain rates of 2000, 3000, and 5000 s^{-1} are shown in Figures 3.7, 3.8, and 3.9, respectively. In these tests, only small strains were achieved during dynamic compression. Therefore, only the initial plateau region of the stress-strain curves was successfully deduced. This was however sufficient to demonstrate the strain rate sensitivity of the foams and for estimating the energy absorption capabilities of the foams at high rates of loading. Figure 3.6 displays the plateau stress and energy absorption characteristics of both PU foams and EPS72 as a function of strain rate. For energy calculation, the same densification strain as measured for the intermediate strain rate regime was used. Data shows that EPS is still rate insensitive at these high strain rates with a consistent plateau stress of around 1.2 MPa. However, the difference in the strain rate sensitivity between PU280 and PU300 can be seen. PU280 tends to become strain rate insensitive at strain rates above $10^3\ s^{-1}$, while PU300 continues to exhibit an increase in the plateau stress with increasing strain rate. The aperture size of PU300 foam is three times smaller than PU280 and thus requires more force to expel air from the foam. Additionally, due to the small aperture size, air is not able to gush out of the cells as demanded by the rapidly increasing load. This data is remarkable in that foam of such a small density is able to increase its plateau stress by almost 308% over its quasi-static value. Such a large increase cannot be attributed solely to the strain rate sensitivity of the polyurea.

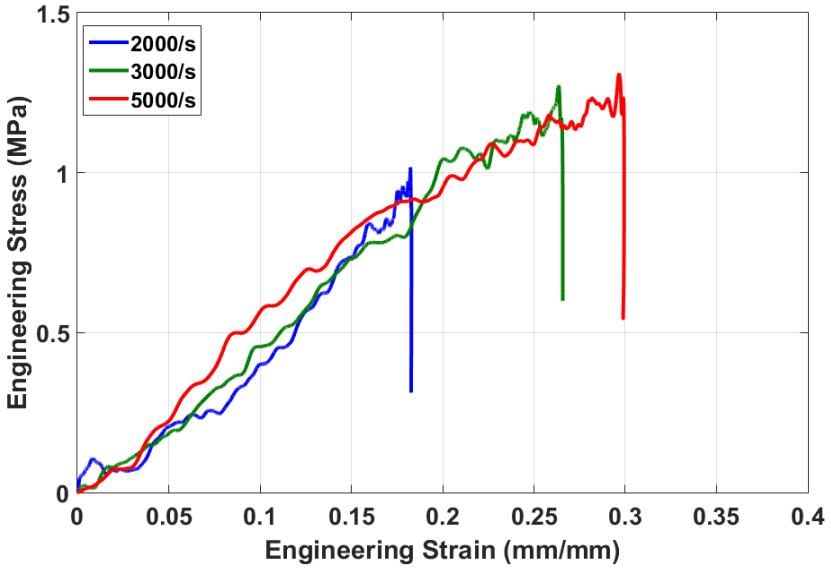


Figure 3.7: Stress-strain behavior of expanded polystyrene EPS72 foam at high strain rates.

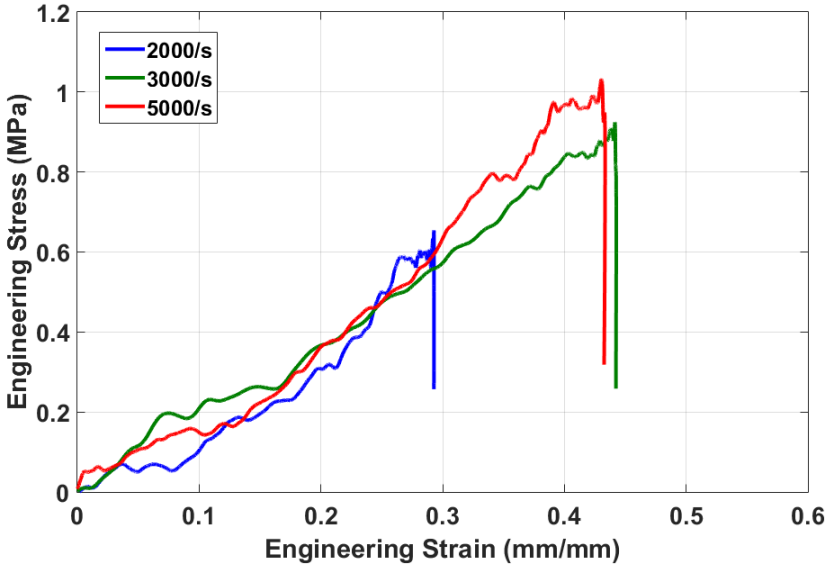


Figure 3.8: Stress-strain behavior of polyurea PU280 foam at high strain rates.

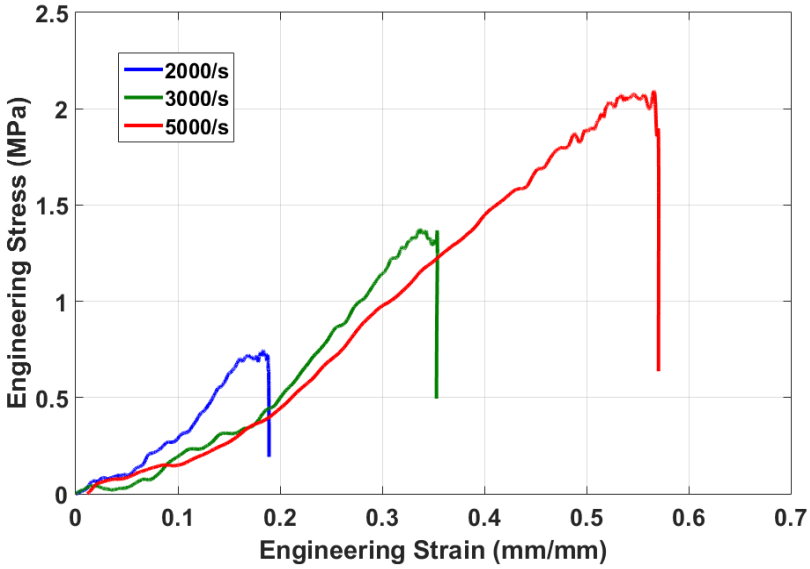


Figure 3.9: Stress-strain behavior of polyurea P300 foam at high strain rates.

The most remarkable property displayed by PU300 foam at high strain rate is that it absorbs more energy per unit volume than EPS72 while also maintaining the peak stress below the brain injury threshold of 1.5 MPa. This data when viewed in light of low and intermediate strain rate results conclusively demonstrates the rate sensitivity of the PU foams.

Following Ashby and Gibson [14], the aperture-related rate sensitivity of the plateau stress as uncovered in our experiments can be modeled through a phenomenological relationship, relating the plateau stress σ to the strain rate $\dot{\varepsilon}$ through the aperture size d as

$$\sigma = \frac{C\mu\dot{\varepsilon}}{1-\varepsilon}\left(\frac{L}{d}\right)^2 \tag{3.6}$$

where, C is a constant of order unity, L is the sample diameter, and μ is the viscosity of air. Figure 3.10 shows that this phenomenological relationship largely captures our data with an effective critical aperture size of 5.2 μm and 4.6 μm instead of 66 μm and 20 μm for PU280 and PU300, respectively. This is can potentially be attributed to the volume fraction of apertures present within

the PU foams and their random distribution (seen in Figure 3.1), which warrants further investigation.

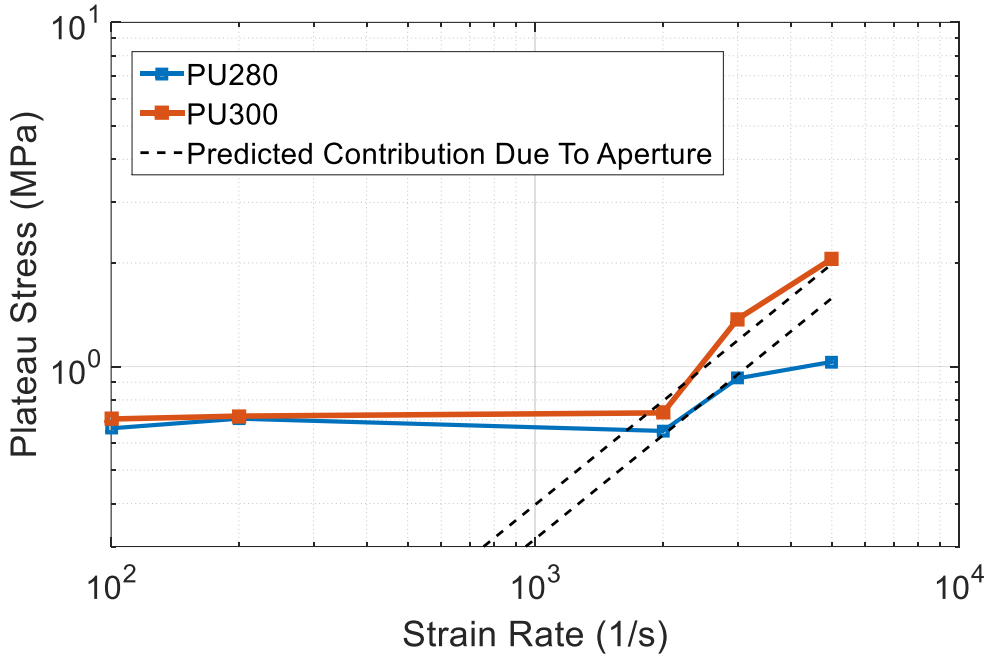


Figure 3.10: Strain-rate dependence of the plateau strength of PU foams. The broken lines are the predicted contribution to the plateau stress due to the aperture size effect, based on Equation (6).

3.5 Conclusions

Experimental compression tests on low density polyurea and EPS foams were conducted at low ($\leq 10^{-1}$ s^{-1}), intermediate ($\leq 10^{-1}$ s^{-1}), and high ($\geq 10^{3}$ s^{-1}) strain rate conditions. All foams exhibited an increase in Young's modulus, plateau stress, and decrease in densification strain under increasing strain, in agreement with the literature [7-13]. Under low and intermediate strain rates, EPS72 foam displayed greater energy absorption properties and higher plateau stresses than both PU280 and PU300. There is a greater energy dissipated in plastic deformation (crushing) in EPS than viscoelastic deformation in PU foams at low and intermediate strain rates. PU foams exhibit a higher strain rate sensitivity when increasing from low to intermediate strain rates. Additionally,

both PU280 and PU300 had similar compressive behavior at these strain rates. However, at high strain rates ($\geq 10^3\ s^{-1}$), the increase in strength provided by the small aperture size became more apparent. PU280 foam's plateau stress became less sensitive to strain rate above 3000 s^{-1}, while PU300 continued to display strain rate sensitivity up to 5000 s^{-1}. This increase in the strength, provided by the cell wall aperture, also increases the energy absorption properties of the PU foams and makes them comparable to EPS. Thus, polymer foams can be manufactured with large cell sizes ($\geq$ 400 μm) and small aperture diameters ($\leq$ 66 μm) to make them both low density and highly strain rate sensitive to absorb more energy than EPS. However, unlike EPS foams which are irreversible crushed after each impact PU foams recover fully after each impact and thus have multiple hit capabilities. This will allow these materials to have a wide range of military and aerospace applications, especially in advance armors and protective body and headgears that are subjected to blast shockwaves and impact from space debris and hypervelocity projectiles that emanate from IEDs.

CHAPTER 4

Impact Attenuation of Viscoelastic Polyurea Foam Liners in Helmets

4.1 Introduction

In contact and motocross sports (e.g., America football, hockey, soccer, and off-road motorcycle racing) the most prevalent type of head injury is mild traumatic brain injury (concussion) [57-64]. This is attributed to the high rates of head collisions with the ground or between players. The detrimental effects of concussive as well as repetitive sub-concussive head impacts have shown to cause impairments in neurocognitive skills such in alertness, memory recall, and attention [57,57,64]. Thus, the safety and health concerns of amateur and professional athletes have led researchers to develop energy absorbing foams (e.g. vinyl nitrile and thermoplastic polyurethane) for protective head and body gears [60,64].

In the previous chapter, we presented polyurea-based strain rate sensitive viscoelastic foams that became increasingly more efficient in dissipating the impact energy as the loading rate was increased. In this study, the combined benefits of temperature stability and rate sensitivity of low density (≤ 200 kg/m^3) viscoelastic polyurea based foams are demonstrated by integrating them as liners into football and motorcycle helmets. Football and motocross helmet drop tests were investigated using the National Operating Committee for Standards in Athletic Equipment (NOCSAE) standards [64-65] and Federal Motor Vehicle Safety Standards (FMVSS) 218, respectively.

4.2 Materials

Open cell polyurea foams were fabricated by mixing modified Methylene Diphenyl Diisocyanate (MDI) compound with oligomeric diamine with different mix ratios. Polyureas of this stoichiometry are known to have behaviors within the viscoelastic regime [29-51]. It consisted of preparing the B-side of the mix by taking the oligomeric diamine polyol and mixing it with appropriate amounts of deionized water, surfactants, cross-linkers, and catalysts to control the gelling and foaming reactions so as to obtain a free-rise foam of predetermined density. The A-side of the mix was the as-received modified Methylene Diphenyl Diisocyanate (MDI). The A and B sides were mixed in 1:4 weight ratio and poured into a 90 mm x 90 mm x 90 mm mold. The rise ratio of the foam was between 7 and 8. Because of the high reaction exotherm, no curing was needed after the completion of the foaming and gelling reactions. The foam was completely tack free after 3 minutes. The entire polyurea foam block was removed from the mold, with sections cut from the center of the molded block to prepare specimens for mechanical testing, and characterization of physical and microstructural properties.

Block samples with densities of 98, 170, and 230 kg/m^3 were manufactured, having much lower densities than that of solid polyurea elastomers (1070 kg/m^3). These densities were chosen because they fall within range used in protective helmets [60]. Three specimens were prepared for each sample-type to study the statistical variation. PU foams will be referred as PU98, PU170, and PU 230 for densities of 98, 170, and 230 kg/m^3, respectively. Scanning electron micrographs (SEM), shown in Figure 4.1, present the microstructures of PU98, PU170, and PU230. PU foams consist of spheroid open cells with cell wall apertures (perforations). The nominal cell sizes are 1000 μm, 600 μm, and 400 μm for PU98, PU170, and PU230, respectively. The nominal cell apertures are 300 μm, 200 μm, and 105 μm for PU98, PU170, and PU230, respectively.

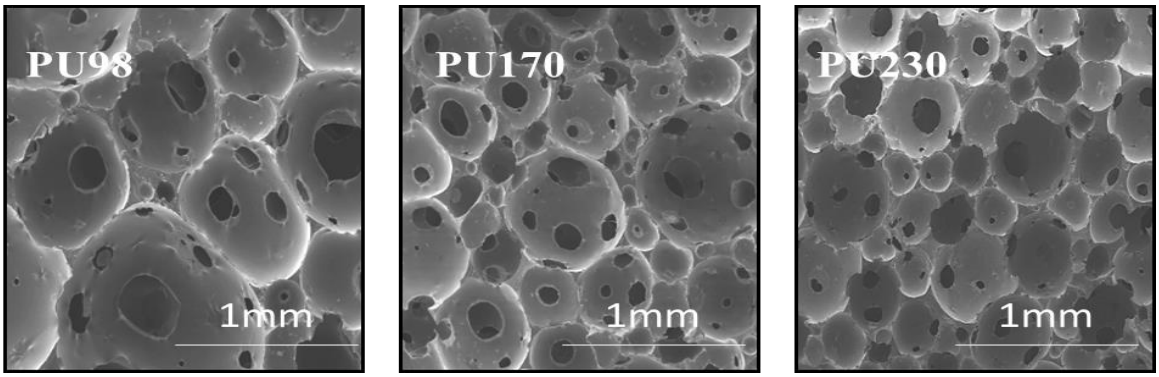


Figure 4.1: SEM images of the microstructure of PU Foams.

Closed cell vinyl nitrile VN600 (111 kg/m^3) foam was obtained from Riddell. In Figure 4.2**,** the SEM micrograph of VN600 is shown having uniformly distributed irregular polyhedral closed cells with a nominal size of 150 µm. The widely used VN600 foam was chosen as a reference material to compare the impact attenuation in football helmets to the PU foams developed for this study.

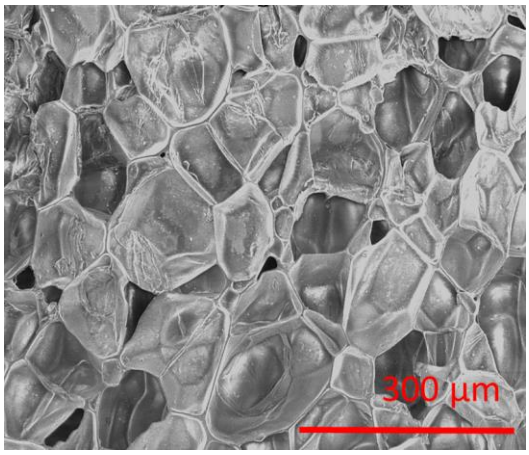


Figure 4.2: SEM image of the microstructure of VN Foam.

4.3 Experimental Procedures

4.3.1 Compression tests

Low strain rate ($\leq 10^{-1}$ s^{-1}) compression tests were conducted using an Instron Micro-Tester (Model 5942) equipped with a 2 kN load frame. For these tests, disc samples of 28 mm nominal diameter and 10 mm thickness were cut from a large molded block. Samples were then compressed under stroke-control with cross-head velocity of 24 mm/min in order to examine the material response over a range of quasi-static strain rates. These cross-head speed yielded a strain rate of $0.04s^{-1}$. Force-displacement data obtained from the machine was converted into the stress-strain data using the sample dimensions.

Intermediate strain rate (10^{1}-10^{2} s^{-1}) compression tests were carried out using an Instron DynaTup (Model 8250) drop-weight impact tester. Specimens with aforesaid dimensions were tested by placing them on a 45 mm-diameter flat force plate and impacted using a 5.5 kg balanced mass attached to a 75 mm-diameter flat stainless steel indenter head. The transmitted force was measured using a force transducer (Kistler Instruments, Model 9041A) with a full scale output of 90 kN and sensitivity of 4.3 pC/N. Impact energy was varied by changing the drop height of the indenter head. The displacement of the top sample surface during impact was also measured using high speed photography. The recorded force-displacement data was converted into engineering stress-strain characteristics using the initial sample dimensions. The strain rate ($\dot{\varepsilon}$) was calculated using:

$$\dot{\varepsilon} = d\varepsilon \big/ dt = \frac{d}{dt}\left(\frac{l - l_o}{l_o}\right) = \frac{1}{l_o}\left(\frac{dl}{dt}\right) = \frac{v}{l_o} \tag{4.1}$$

where v is the impact velocity and l_o is the specimen thickness. It should be noted that a constant strain rate is not attained in this experiment as the velocity of the falling mass is reduced during foam compression. However, the strain rate computed using the initial impact velocity and that calculated by differentiating the strain profile yielded only a 10% difference below 60% strain. Therefore, the stress-strain response up to 60% strain can be considered constant for all practical purposes. Data presented in this paper was at a strain rate of 200 s^{-1} is reported here.

4.3.2 NOCSAE Standard Tests

Two helmets were tested using the NOCSAE Football Helmet standard test [65-66], shown in Figure 4.3, at the Dynamic Research, Inc. located in Torrance, California. Polyurea foam material was placed inside a Riddell Revolution (large/varsity) helmet shell from which the original Riddell foams (vinyl nitrile-VN600 with density of 111 kg/m^3) were removed. The polyurea foams were of the same thickness (28 mm) and geometry, thus fit perfectly inside the shell (Figure 4.4). A brand new Riddell Revolution helmet containing VN600 foam with identical shell material and geometry was used as a control. The two helmets were dropped using a NOCSAE medium headform (4.9 kg) from heights ranging from 1 to 5 feet even though the standard testing only requires dropping from 5 feet. Lower drop height tests were motivated by the fact that there are over 200 hits during a regular NFL season that correspond to the lower energy [64]. Therefore, it is important that the helmet performs adequately at lower energies as well. All impact tests were done on the crown location (top) of the helmet and dropped on a ½ inch MEP pad.

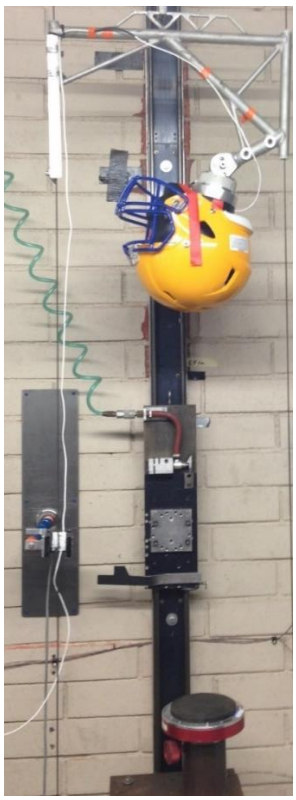


Figure 4.3: NOCSAE standard impact test setup for football helmets.

Additionally, low and intermediate impact velocity tests ranging from 1 to 4 feet were conducted at cold (-15° C), ambient (25° C), and hot (50° C) temperatures. In these temperature tests, the best performing PU foam was chosen and used to compare against the Riddell VN600 foam. The foam thicknesses were cut down to 22.2 mm (7/8 in) to the see the effect of thickness on the impact attenuation properties as well.

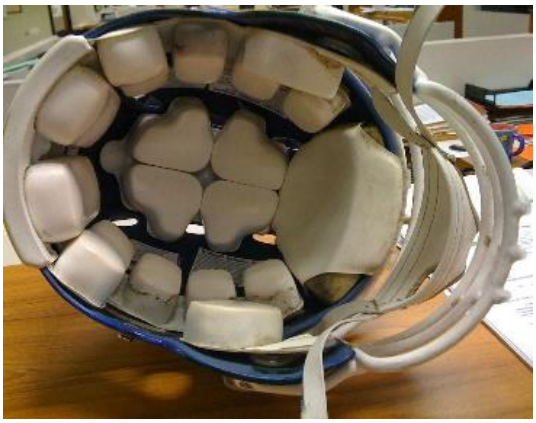


Figure 4.4: PU98 foams inside the Riddell football helmet.

4.3.3 Severity Index and Head Injury Criteria

The National Operating Committee for Standards in Athletic Equipment (NOCSAE) was established to decrease the likelihood of football related head injuries (e.g. traumatic brain injury, skull fracture, and loss of consciousness) by implementing a helmet certification drop test (described in previous section) which simulates severe head impacts during actual play. This test criterion was based on the Wayne State University Tolerance Curve (WSUTC) on animal concussion and cadaver skull fracture tests [67].

The two most used metrics which quantify the severity of a given impact based on the WSUTC are the Gadd Severity Index (GSI) and the Head Injury Criterion (HIC) [68-71]. The GSI is based on a linear approximation of the slope of the WSUTC curve using a log-log plot [68] and it is calculated as

$$GSI = \int_0^T a(t)^{2.5}\, dt \tag{4.2}$$

where $a(t)$ is the linear acceleration of the headform's center of gravity in gs (1g= 9.8 m/s^2) and T is the impact duration in seconds. The GSI should not exceed 300 for impact velocities of (3.4 m/s) and never exceed 1200 for any given impact [65-66]. Subsequently, the HIC is based on choosing the limits of integration for the given linear acceleration-time curve of the headform's center of gravity during impact test which maximizes the HIC function [69] given by

$$HIC = \left\{ (t_2 - t_1) \left[\int_{t_1}^{t_2} \frac{a(t)}{(t_2 - t_1)} dt \right]^{2.5} \right\}_{\max} \tag{4.3}$$

where $a(t)$ is the linear acceleration of the headform's center of gravity (g), t_1 and t_2 are the limits of integration in seconds. In general, the maximum time limit of integration for HIC that is used is $t_2 - t_1 = 15\ ms$. The HIC value should be limited to 600 for moderate injury and 1000 for severe injury. Currently, the onset of MTBI have been found to be correlated with a GSI of 300 and HIC of 250 [4,6,29]. Thus, analyzing both metrics independently will be used to analyze the performance of the helmets with either VN or PU pads.

4.3.4 Federal Motor Vehicle Safety Standards (FMSS) Liner Tests

Motor vehicle (e.g. motorcycles, dirt-bikes, all-terrain quad bikes) helmets are made of a hard protective outer shell which distributes the impact force over a larger area and are lined with an energy absorbing material that reduce force that reaches the head. Federal Motor Vehicle Safety Standards (FMVSS) 218 establishes requirements for the minimum impact attenuation a helmet

must meet in order to protect the head from impact shock related injuries such as skull fracture or brain injury.

Skull-caps using 6 mm thick polyurea foam PU98 (98 kg/m^3) sections were placed on the 5 kg DOT size-C dummy headform as shown in Figure 4.5. PU98 foam was chosen as it outperformed PU170 and PU230 in the previous helmet experiments. The skullcaps provide an additional protective layer as well as a better fit between the helmet and the head of the user. Motorcycle helmets with an expanded polystyrene (EPS) foam liner of density 52 kg/m^3 were provided by O'Neal Motocross Company and placed on the headform. The headform/skull-cap/helmet combination was dropped from a height of 1.93m (6 m/s) onto a flat steel anvil as per the FMVSS 218 test standard and impacted with two successive identical impacts within a 90 second interval. The vertical acceleration of the headform was measured using a single linear accelerometer that is instrumented within the headform. Tests were conducted at the ACT Labs in Los Angeles, CA. Additionally, widely used D3O polymer material (1100 kg/m^3) was tested for comparison against the polyurea skullcap while a helmet without a skull-cap was tested as a control sample.



Figure 4.5: (Left) 5 kg DOT size-C dummy headform, (Middle) 6 mm thick skull-cap, and (Right) Motorcycle Helmet.

4.4 Results and Discussion

4.4.1 Compression Test Results

Figures 4.6 and 4.7 show the stress-strain behaviors of the PU foams (PU98, PU170, and PU230) along with VN600 at quasi-static ($\dot{\varepsilon} = 0.04s^{-1}$) and dynamic ($\dot{\varepsilon} = 200s^{-1}$) strain rates, respectively. An increase in Young's modulus, plateau stress, and a decrease in densification strain can be observed with increasing density and deformation rate in the stress-strain behavior of the PU foams. This behavior partly stems from the very high strain rate sensitivity of the solid polyurea that forms their cell structure but more importantly it is related to the size of the cell wall apertures as explained in Chapter 3. The aperture size have negligible effect on their overall compressive stress-strain behavior at low rates of deformation ($\leq 10^{-1}$ s^{-1}) since the air can easily move out of the foam during quasi-static compression. At intermediate rates (10^{1}–10^{2} s^{-1}), however, the work required to drive the air out from the center of the foam cells through the small apertures starts to contribute to the strength of the foam. This is because the rate at which the air can escape from these tiny perforations is slower than the rate of loading which then leaves the air inside the cells, strengthening them, much like air or gas trapped inside a closed-cell foam system.

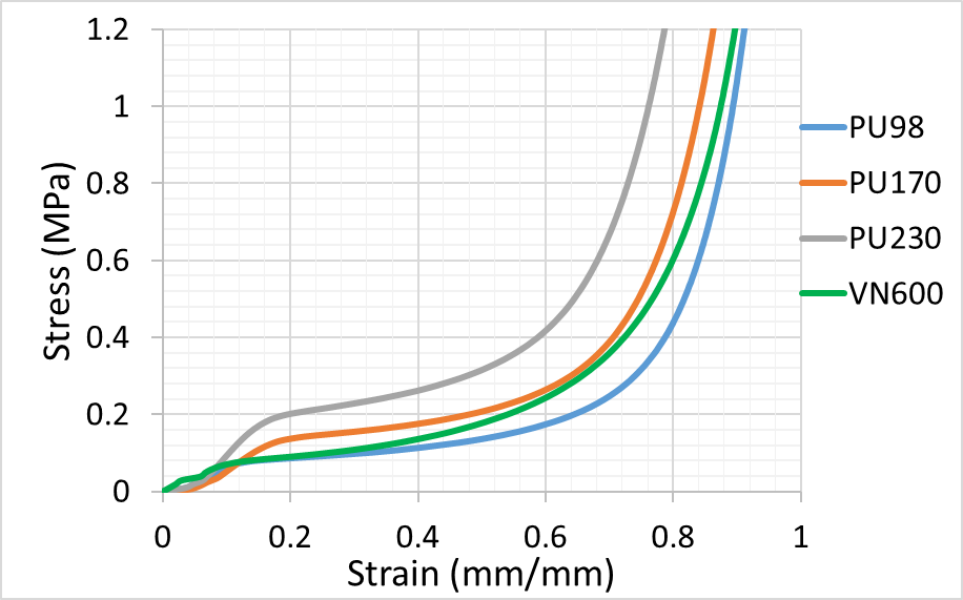


Figure 4.6: Engineering stress-strain behavior of PU98, PU170, PU230, and VN600 under quasi-static deformation rate of 0.04 s^{-1}.

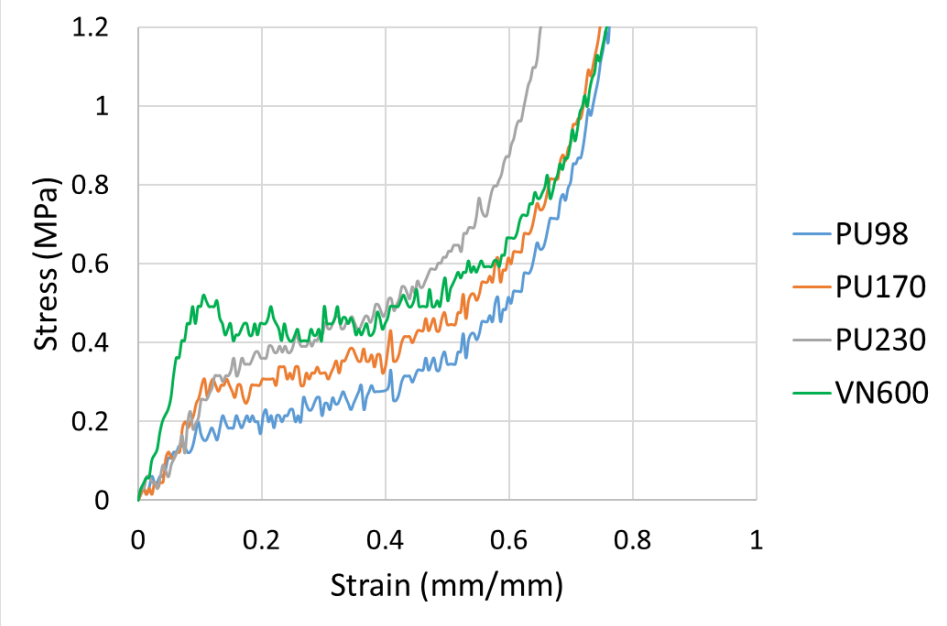


Figure 4.7: Engineering stress-strain behavior of PU98, PU170, PU230, and VN600 under dynamic deformation rate of 200 s^{-1}.

The stress-strain behavior of VN600 is similar to that of PU98 up to 30% strain under quasi-static deformation rate. Beyond 30% strain, the air pressure within the closed cells of the VN foam begins to contribute to the plateau strength. Unlike the open cell structure of the PU foams which allow the air to move freely within the foam, the compression of the fluid inside the closed cell requires larger stresses to continue to collapse the foam. Thus, the VN600 foam has higher plateau stress after 30% strain than PU98.

Although the quasi-static and dynamic compressive behavior of the PU and VN foams gives great insight into their mechanical behavior and energy absorption capabilities, it is difficult to determine which foam will perform the best in a given helmet application since the helmet shell itself absorbs some of the incoming impact. Thus, specific NOCSAE and FMVSS standard testing was conducted to see the actual performance of the helmet/foam system. Here, the optimal foam will be the one which reduces the transmitted impact gs felt by the headform and minimize the severity of the impact using GSI and HIC criteria.

4.4.2 NOCSAE Helmet Test Results

Table 4.1 provides the headform's responses using PU foams in the Riddell Revolution helmet. The impact velocity, peak head gs, GSI, and HIC values are reported for drop heights of 3 and 5 feet. PU98 foam had the lowest reported peak gs as well as GSI and HIC values when compared to PU170 and PU230. Although, PU98 foam has the lowest density of the PU foams, it performs the best within the Riddell helmet. This can be attributed the foam thickness and foam impacted area which dictate the performance of the helmet/foam system [60]. Thus, the density of PU98, geometry, and dimensions of the foam within the Riddell helmet attenuates impacts better than

higher density foams of same geometry and size. In the 3-foot drop tests, the GSI values are below 300 and HIC below 250 for all PU foams. This is a great indicator that at lower impacts, they can possibly provide adequate protection against MTBI injuries. Additionally, the peak gs were all under the peak threshold of 125g and thus can provide protection against TBI impact as well. Since PU98 performed the best, it was further tested along with VN600 for comparison. This will compare the potential for using PU foams in current football helmets and other blunt head protective equipment which use hard outer shell.

Table 4.1: Headform's impact velocity, peak head gs, GSI, and HIC values using PU Foams.

Foam Material	3 ft. Drop Height (3.7 m/s)			5 ft. Drop Height (4.8 m/s)		
	Peak g	GSI	HIC	Peak g	GSI	HIC
PU98	52.9	151	136	83.3	398	352
PU170	64.5	202	180	105.2	565	492
PU230	70.4	234	202	115.2	640	553

Table 4.2 shows the peak gs, GSI, and HIC response of the NOCSAE headform using PU98 and VN600 pads in Riddell Revolution helmet from 1 foot to 5 feet drop height. On an average, the PU98 foam liner represents a 22% reduction in peak gs, 26% reduction in GSI, and a 25% reduction in HIC values across the board. Figure 4.8 shows a typical acceleration versus time curve comparing PU98 and VN 600 at 5 ft. drop height. The reduction in peak gs and GSI values, can lead to a 15-25% reduction in concussion risk based on the Pellman curve [61-63]. This a significant improvement over current VN foam technology. Most importantly, PU98 foam outperforms the VN600 foam at all drop heights. Since large number of helmet impacts are actually at lower heights and velocities, PU foams can perform better under repetitive sub-concussive and concussive hits than VN foams.

Table 4.2: Headform's impact velocity, peak head gs, GSI, and HIC values comparing PU with VN Foams.

Drop Hg. ft.	Impact Vel. ft/s	Peak g			SI			HIC		
		VN600	PU98	% red.	VN600	PU98	% red.	VN600	PU98	% red.
1	6.8	27.6	25.0	9.4	33	25	24.2	30	23	23.3
2	9.8	50.8	39.3	22.6	107	81	24.3	94	74	21.3
3	12.0	70.6	52.9	25.1	217	151	30.4	190	136	28.4
4	14.0	84.6	65.5	22.6	344	249	27.6	304	222	27.0
5	15.7	103.0	83.3	19.1	517	398	23.0	459	352	23.3

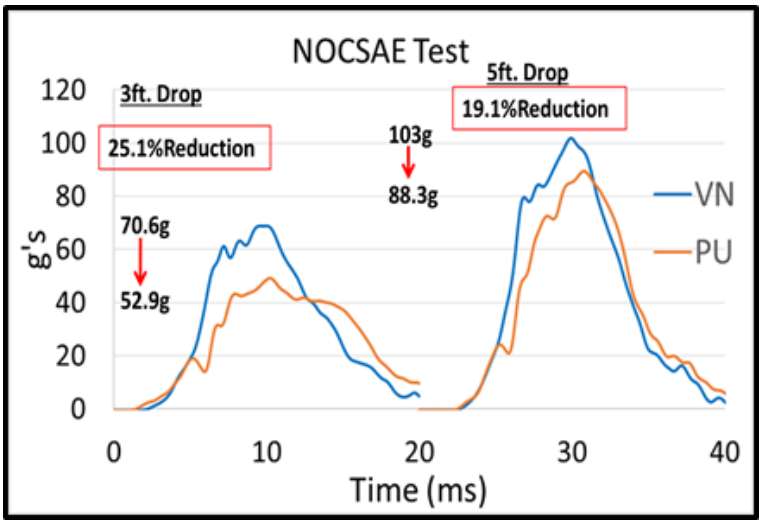


Figure 4.8: Head Acceleration of NOCSAE tests using polyurea foams compared to VN.

The dissipation of the impact energy in the PU foams start at the molecular level through reversible viscoelastic shear deformations between the hard and the soft phases of the polyurea structure when the micrometer-sized struts, beams, and thin plates of the foam cellular structure buckle, bend, and twist to generate very large local shear strains during foam compression. This intrinsic molecular-level shear dissipation process in polyurea foams is synergistically coupled to an additional energy and momentum trapping mechanism that includes controlled collapse of a novel cell microstructure that comprises of very large cells (300 to 500μm), each covered with a

perforated membrane with apertures 20 to 70 μm in diameter (Figure 4.1). At very low strain rates, air escapes easily from large cells through perforations, allowing easy collapse of the microstructure to limit the peak force below the injury threshold levels. At higher velocity impacts or higher strain rates, air starts to provide viscoelastic damping and substantial strengthening to the cell walls as its rate of escape through tiny perforations cannot catch up with the higher rate of loading. Consequently, the same low density material can now support a much higher dynamic load without the need to increase the density of the material. Every other commercially available foam today requires a substantial increase in the density (or reduction in cell size with higher thickness of cell walls) to support the enhanced dynamic loads that arise at higher strain rates. Thus, this microstructure makes the polyurea foams "strain rate dependent," with the performance becoming better at increasing strain rates and thus, it is able to outperform VN foams at every impact velocity.

Table 4.3: Headform's impact velocity and peak head gs comparing PU and VN Foams at different temperatures.

Drop Height ft. (m)	Impact Velocity ft/s (m/s)	Peak g – Ambient (23°C)			Peak g – Cold (-15°C)			Peak g – Hot (50°C)		
		VN600	PU98	% red.	VN600	PU98	% red.	VN600	PU98	% red.
1	6.8	61.0	50.0	18.0	97	78	19.6	55	54	1.8
2	9.8	79.0	75.0	5.1	153	113	26.1	77	74	3.9
4	14.0	132	130	1.5	229	156	31.9	178	143	19.7

Table 4.3 shows the temperature effect on the peak gs experienced by the headform's center of gravity at drop heights of 1, 2, and 4 feet. For these temperature tests, the foam thicknesses were

reduced to 7/8 of an inch, to examine the effect of foam thickness as well. At ambient temperatures (23°C) the PU98 foam reduced the peak gs by as much as 18% when compared to VN600. At cold temperatures (-15°C) PU98 foam reduced the peak gs by an average of 25.8% when compared to VN600 across all drop heights. Furthermore, at hot temperatures (50°C), PU98 reduced the peak gs by as much as 19.7% when compared to VN600. This a significant improvement in the impact attenuation of VN foams at low and hot temperatures. Viscoelastic foam systems are susceptible to temperature variations, becoming harder at cold temperature as well as softer at high temperatures, which in turn effects their energy dissipation performance. However, the glass transition temperature of polyurea is -50°C and thus it retains its superior impact properties over a range of temperatures (-15°C to 50°C). This is in contrast to commercially available high performance foams such as VN600 that have the glass transition temperature near 0°C and absorb energy through phase transformation at ambient conditions but significantly stiffen up at lower temperatures. Additionally, the reduction in padding thickness (from 28mm to 22.2mm) increased the peak gs for both VN and PU foam at ambient conditions when compared to values in Table 4.2. This shows how thickness effects the performance of the helmet/foam system as well as temperature. Thus, the foam padding material, the thickness, and temperature effect the impact mitigation properties of a helmet/foam system.

4.4.3 FMVSS Liner Test Results

The use of polyurea foam resulted in a head acceleration of 147g (179g). When the same helmet was impacted for a second time, a head acceleration of 177g (202g) was recorded. The values in parenthesis are for the control without the use of any skullcap. The corresponding head

accelerations for the best performing gel material that outperformed the VN foams and few other commercially available foams was 160g and 195g for the first and second hits respectively. Therefore, polyurea based foams perform much better as liners than conventional materials currently used.

4.5 Conclusions

On average, a 22% reduction in peak gs, 26% reduction in GSI, and a 25% reduction in HIC values were found for PU98 foam when compared to widely used vinyl nitrile foam, VN600 (density of 111 kg/m^3), at thicknesses of 28 mm under ambient conditions from 1 ft. to 5 ft. drop heights. Under reduced liner thicknesses (22.2 mm), PU98 foam reduced the peak gs by as much as 18% under ambient conditions(23°C), 25.8% under cold temperatures (-15°C), and 19.7% under hot temperatures(50°C) when compared to VN600 at drop heights of 1 to 4 feet. Thus, polyurea based foams show promise in the reduction of head injuries when used as foam liners football helmets while also being lighter than current VN foam technology by 11.7%. It is emphasized that the performance of the helmet/foam system reported here are a strong function of foam liner density and thickness while the temperature stability is dependent on the intrinsic glass transition temperature of the polymer.

CHAPTER 5

Shock Attenuation Properties of Polyurea Based Foams for Midsoles in Footwear

5.1 Introduction

Sports like basketball and soccer involve repeated foot-ground impacts. The peak forces experienced in these sports as well as in everyday activities (e.g., walking and running) have been found to be in excess of 2 times the body weight of the person as shown in Figure 5.1 [2, 72-74]. The amplitude and duration of the impact are a function of body mass [72], running style (e.g. rear-foot strike versus mid-foot strike) [72-74], running velocity [72-73], and ground surface [2]. In addition, the impact generates a stress wave that is transmitted up the body through the musculoskeletal system, often referred to as body shock loading.

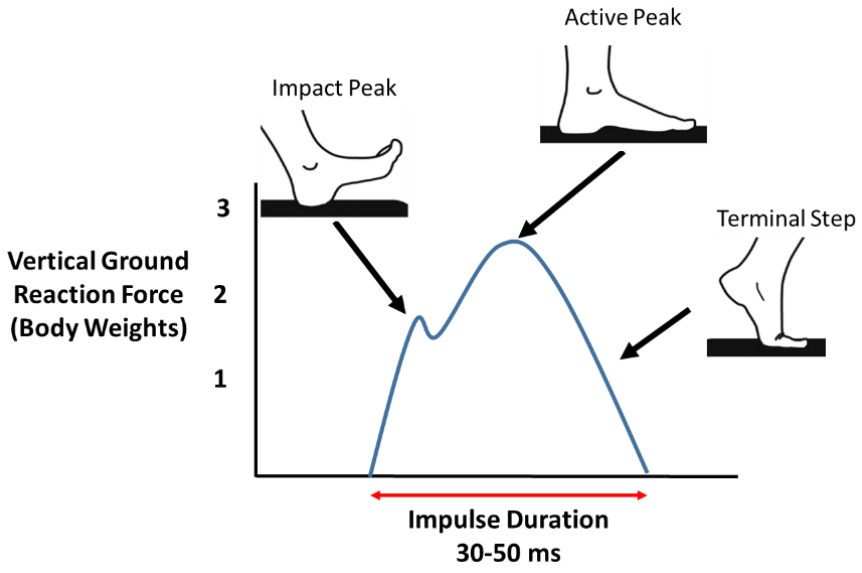


Figure 5.1: Typical ground reaction force while running [2].

The initial peak loading upon impact can lead to heel and subtalar joint injuries, while the transmitted stress wave can lead to severe injuries in the lower body extremities (e.g. lower back, knee, and hip joints). More specifically, the repetitive impacts can cause stress fractures, plantar fasciitis, and shin splints [75]. It can also deteriorate the articular cartilage in knee and hip joints which can develop into osteoarthritis. Thus, polymeric foams are extensively used in shoes to mitigate against dynamics loads generated by the impact between the foot and the ground surface.

The cushioning properties of the midsole as well as its thickness play a major role in the shock absorbing capabilities of shoes [14, 17, 76-78]. The energy absorption provided by the ability of the foam to undergo large deformations under low stresses, reduces the transmitted impact forces to the asset. In addition, the compliance of the foam material distributes the forces over a larger area, reducing the plantar pressures at the foot-foam interface [79]. Another important property that influences the shock attenuation of repeated impacts is the dampening properties of the foam material which characterized by peak forces that are transmitted to the asset and the energy return or rebound energy, the percentage of the input energy that is returned and not dissipated as heat. The higher return energy values indicate higher rebound and resiliency in the material, meaning it will recover faster for a given impact condition.

Most midsoles in running shoes and other athletic footwear consist of either ethylene vinyl acetate (EVA) or thermoplastic polyurethane (TPU) foams with densities ranging from 130 – 250 kg/m^3 [15, 80]. Both foam technology provides adequate shock attenuation and durability as midsole materials at low densities and thus are widely used in industry. Currently, polyurea elastomers are used in a wide range of applications such as coating and liners for their unique rate-dependent viscoelastic properties [29, 32-33], impact and dynamic properties [34-39], and

temperature stability [27]. Moreover, thin (1.5-2 mm) polyurea dense films have been found to dramatically increase the impact attenuation of low density bilayer foam systems [44]. Therefore, polyurea is an excellent candidate for foaming, given its superior mechanical and impact properties over other elastomers.

The purpose of this study was to investigate whether low density polyurea foams are applicable as midsoles in athletic footwear. The impact attenuation and rebound energy (resiliency) properties of polyurea foams and polyurea foam/polyurea film bilayers are investigated according to the American Society for Testing and Materials (ASTM) test methods F1976 [81] and D3574 [82] and were compared with currently used EVA and TPU foam technology at similar densities.

5.2 Materials and Methods

5.2.1 Materials

Open cell polyurea (PU) foams were fabricated by mixing Isonate® 143L (modified Methylene Diphenyl Diisocyanate (MDI) compound made by DOW Industrial) with Versalink® PI000 (oligomeric diamine made by AirProduct Inc) in a 1:4 ratio, this polyurea stoichiometry behaves in the viscoelastic regime [29-44]. The mixture was stirred using a high rpm electric stirrer to introduce small air bubbles (physical blowing agent) and create a polyurea froth. Next, the PU mix was poured into a 90 mm x 90 mm x 90 mm mold and placed in a vacuum oven at 80˚C. Slow vacuum was pulled until the desired foaming height was reached. The pressure inside the vacuum supports the cellular structure as it is curing for 24 hours. The density of the PU foams were controlled by adjusting the amount of foaming for a given constant amount of mixture. Block samples with densities ranging from 140 kg/m^3 to 230 kg/m^3 were manufactured. These densities

were chosen because they fall within range used in various impact applications with impulse duration in the 1 – 100 ms such as in shoe-soles [80]. Three specimens were prepared for each sample-type to study the statistical variation. The polyurea foams of densities 140 kg/m^3, 170 kg/m^3, 200 kg/m^3, and 230 kg/m^3 will referred to as PU140, PU170, PU200, and PU230, respectively. SEM images of the PU foams can be seen in Figure 4.1 of the previous chapter.

Polyurea dense films were manufactured following the same 1:4 ration of Isonate® 143L to Versalink® PI000. The mixture was stirred and placed in a 250 x 250 x 2 mm mold plate and placed in a vacuum to remove any air bubbles present. Next, the polyurea film was placed in an oven at 80˚C for 24 hours for the film to cure. The density of the polyurea film was measured to be 1073 kg/m^3.

Polyurea foam samples were tested along with commonly used Ethylene-vinyl acetate (EVA) with densities of 180 kg/m^3 and 200 kg/m^3 which will referred to EVA1 and EVA2, respectively. In addition thermoplastic polyurethane (TPU) foams with densities of 200 kg/m^3 and 220 kg/m^3 were also tested for comparison and referred to as TPU1 and TPU2, respectively. The bilayer systems were made by using spray adhesive to join the 2 mm polyurea dense film on top of the designated foam.

5.2.2 Quasi-static Compression Tests

Compression experiments were conducted on cylindrical specimens with section thicknesses of 10 mm and diameters of 27.65 mm. Low strain rate ($\leq 10^{-1}$ s^{-1}), compression tests on PU specimens were conducted on a 2 kN load frame (Instron Micro-Tester, Model 5942) equipped with a force transducer and displacement measuring device. Displacement controlled compression were used

with cross-head velocity of 2.4 mm/min in order to examine the material response over quasi-static strain rate. Force-displacement data was obtained and converted to stress-strain data using sample dimensions.

5.2.3 Impact Attenuation Tests

Impact mitigation properties of all PU foams and bilayer foam systems were characterized following the American Society for Testing and Materials (ASTM) test method F1976 [81], an impact attenuation test for athletic footwear. The mass, contact area and impact energy of the standard test are based on research into the dynamics of foot impact. The ASTM F1976 tests were carried out using a drop-weight impact tester (Instron DynaTup, Model 8250), which is capable of discreetly raising an interchangeable weight to various heights as shown in Figure 5.2. Specimens of 75 x 75 x 20 mm sections were tested by placing them on a 45 mm-diameter flat force plate and impacted using an 8.5kg balanced mass attached to a 75 mm-diameter flat stainless steel indenter head. The standard requires an impact energy of 5.0 Joules (J), typical for running shoes. 7.0 J tests were also conducted, which represents higher impacts such as in basketball shoes. The transmitted force, which determines the peak shock of the impact, was measured over time by using a force transducer (Kistler Instruments, Model 9041A) with full scale output of 90 kN and sensitivity of 4.3 pC/N. Additionally, the displacement was measured optically as the indenter head contacts the specimen, using high speed photography. Thus, the force-displacement data was also obtained for each given impact. The force-time data was then used to analyze the peak force and time duration of the impact. The force-displacement data analysis will be explained in the following section. Note that the polyurea dense film was placed on the top orientation, meaning, it is on the side which is getting impacted by the falling mass.

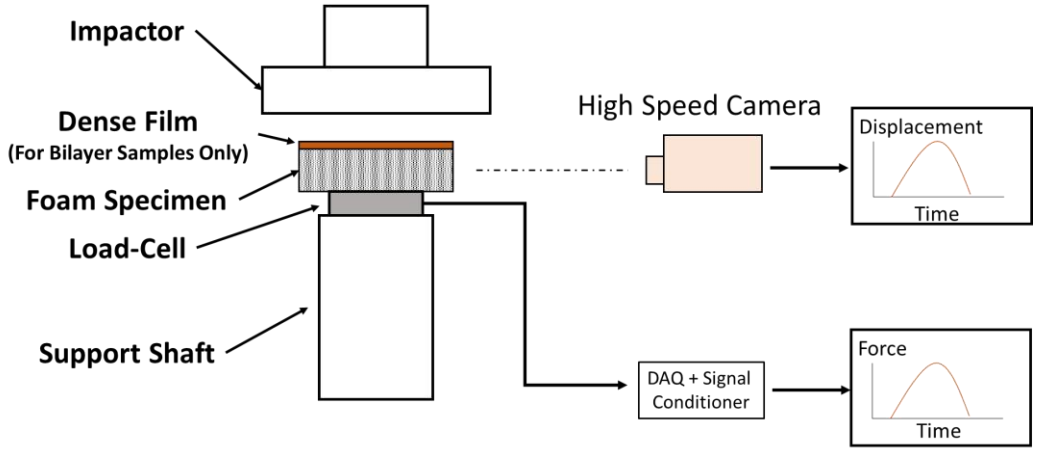


Figure 5.2: Drop-weight tower for impact tests.

5.2.4 Relative Rebound Energy and Maximum Displacement

The relative rebound energy or the resiliency (the instantaneous feel/bounciness) of the foam samples and bilayer systems were tested and measured according to ASTM-D3574 [82]. The relative rebound energy was measured by dropping a 16 mm diameter steel ball from a height of 500 mm. The maximum rebound height (h_{final}) was measured and recorded. The relative rebound energy is thus calculated as a percentage of the rebound height over the initial drop height as shown

$$E_{RR} = \frac{h_{final}}{500mm} \times 100 \tag{5.1}$$

The goal of a foam is to attenuate an impact by reducing the transmitted force while maximizing the rebound energy (minimizing the energy loss). Essentially, you want a foam to recover quickly and transmit back the compressional energy to the runner for better efficiency during running or walking.

Another important quantity for comparing the cushioning properties of different midsole foam materials is to examine the maximum deflection at 5 J impact energy. The maximum deflection determines how much the user's center of gravity will change during walking or running. Although there is much debate as to the effect of efficiency and oxygen consumption during running as a function of vertical displacement of the center of gravity of the runner, the energy required to displace the center of gravity is definitely of importance. Therefore, examine how much the foam material will displacement is important in energy required for the person to keep he displacement in a preferred state.

5.3 Results and Discussion

5.3.1 Quasi-Static Compression Results

In Figure 5.3, the stress-strain behavior of the PU foams at a quasi-static strain rate of .004 s^{-1} are shown. The stress-strain behavior of all the PU foams follow an initial linear response due to elastic bending of the cell walls followed by a stress plateau region due to elastic buckling of the cell walls. Next, the stress increases rapidly under small strains. Here, the foam's cellular structure is fully collapsing and the cells begin to compress into one another, acting as a dense material, thus the stiffness increases rapidly. Furthermore, it can be observed that the elastic modulus and stress plateau regions increase while the densification strain decreases with an increase in foam density. Using similar empirical formulations to that of Gibson and Ashby [14], the following empirical relationships were obtained:

$$\frac{E_f}{E_s} = 1.21\left(\frac{\rho_f}{\rho_s}\right)^{2.91} \tag{5.2}$$

$$\frac{\sigma_{pl}}{E_s} = .333\left(\frac{\rho_f}{\rho_s}\right)^{3.34} \tag{5.3}$$

$$\varepsilon_D = .937 - .1.22\left(\frac{\rho_f}{\rho_s}\right) \tag{5.4}$$

where E_f is the Young's modulus, ρ_f is the density, $\sigma_{Pl}$is the plateau stress, and ε_D is the densification strain of the polyurea foams. The E_s is the Young's modulus and $\rho_s$is the density of the solid polyurea film which were 90 MPa and 1070 kg/m^3, respectively. It is important to note that these values represent only empirical relationship for open-cell PU foams manufactured here with densities ranging from 140 kg/m^3 to 230 kg/m^3 under a strain rate of 0.004 s^{-1}.

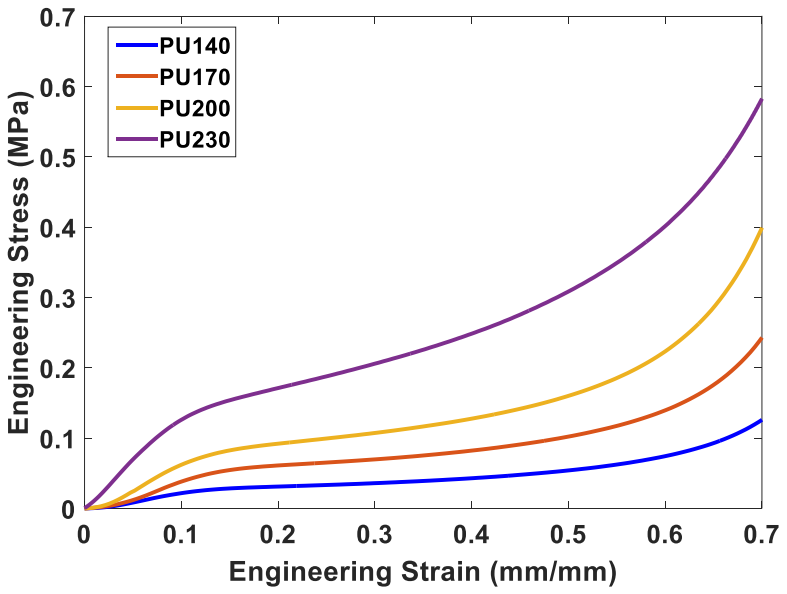


Figure 5.3: Stress-strain behavior of PU foams at a strain rate of 0.004 s^{-1}.

5.3.2 Shock Attenuation Results

Figures 5.4 and 5.5 show the average force-time curves for foam only specimens. Fig. 5.4 shows the force-time curves at an impact energy of 5 J while Fig. 5.5 is at an impact of 7 J using an 8.5 kg weight following ASTM F1976. At an impact energy of 5 J and 7 J, the peak transmitted force for each of the PU foams is well below the peak forces that EVA and TPU specimens transmit (Fig. 5.4B). For example, at a 5 J impact energy, PU170 results in a peak force of 0.60 kN while EVA and TPU foams had an average peak force of about 0.85 kN. This represents a 28.6% reduction in the amplitude of the force that is transmitted to the asset. This is great improvement in shock attenuation properties over current advanced foams. Thus, polyurea foams have a great potential in decreasing the transmitted forces felt by the asset during foot-ground impacts Additionally, at the 7 J impact, the PU foams show a reduction in impact force ranging from 6.0% to 36.9%, depending on PU and EVA or TPU foam chosen. Even at higher energy impacts, polyurea foams show to outperform current EVA and TPU foam technologies of similar densities by large margins.

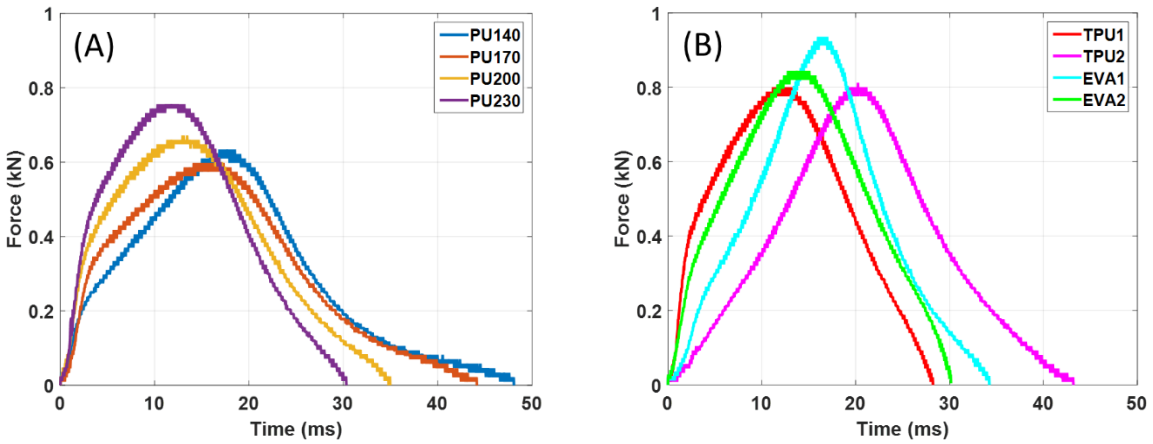


Figure 5.4: Force-time curves at 5 J impact for (A) PU foams and (B) EVA and TPU foams.

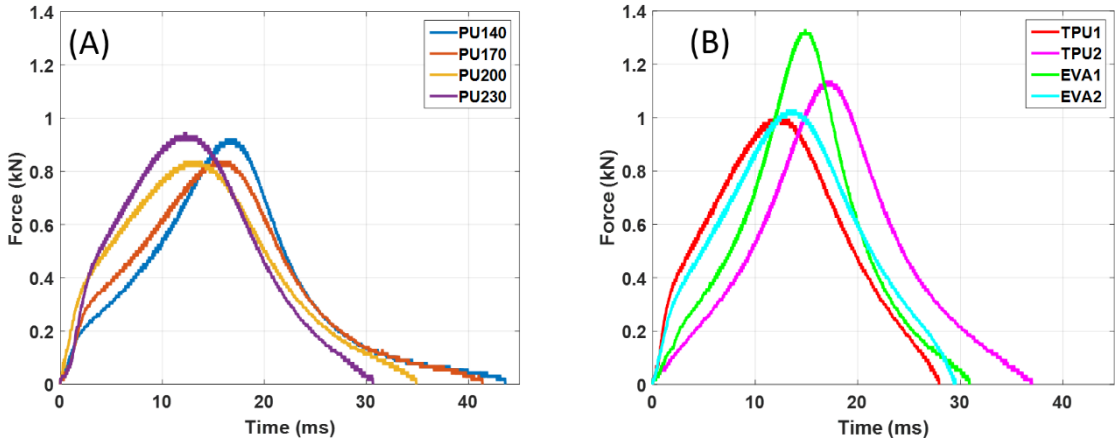


Figure 5.5: Force-time curves at 7 J impact for (A) PU foams and (B) EVA and TPU foams.

Figures 5.6 and 5.7 show the average force-time curves for bilayer foam specimens at 5 J and 7 J impacts, respectively. As mentioned, the bilayer consists of placing a 2 mm dense layer of dense polyurea on top of the foams. This was motivated by the fact that most athletic shoes consist of dense shoe-sole inserts for additional comfort and protection. The impact results indicate that the addition of the thin film of polyurea increase the stiffness of the foam system, but does not dramatically change the peak transmitted forces when going from foam to bilayer as shown in Figure 5.8.

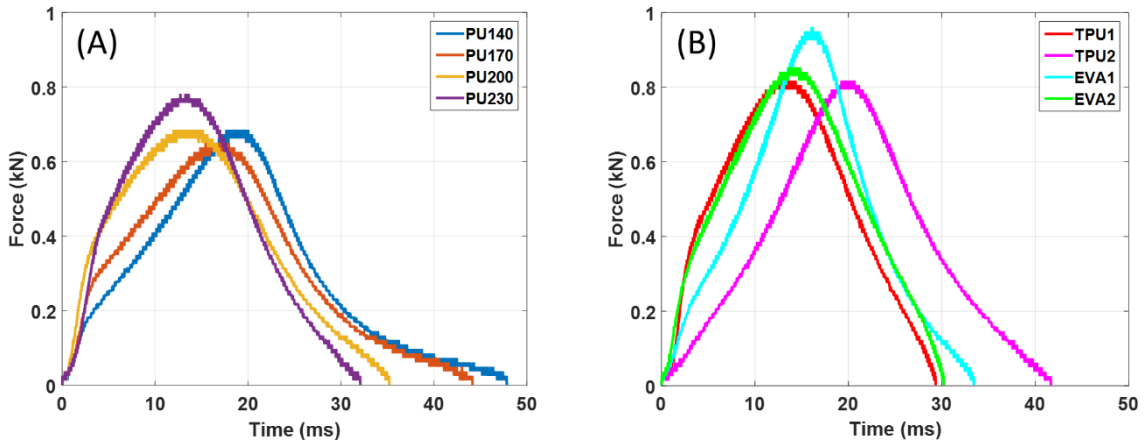


Figure 5.6: Force-time curves at 5 J impact for (A) PU foams and (B) EVA and TPU foams with polyurea dense film.

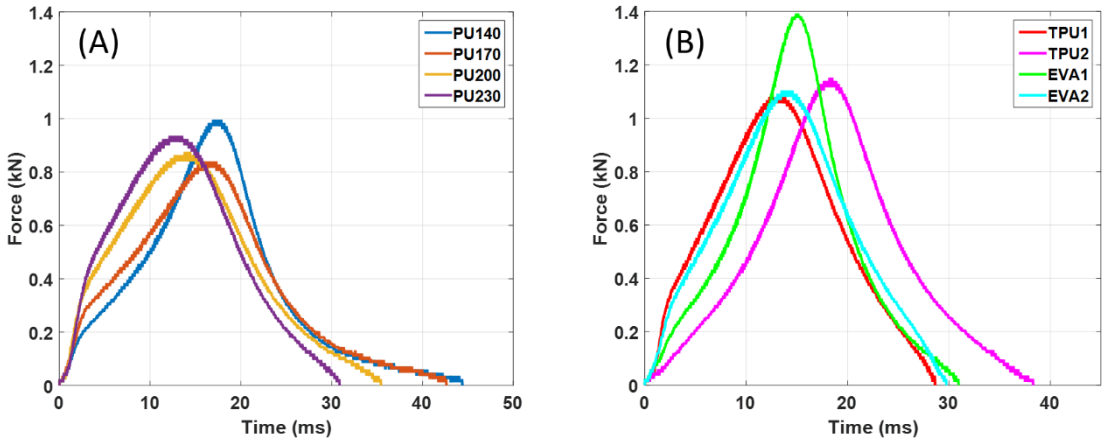


Figure 5.7: Force-time curves at 7 J impact for (A) PU foams and (B) EVA and TPU foams with polyurea dense film.

The average increase in peak force was 5.2% for the PU foams and 1.7% for EVA and TPU foams when the dense polyurea film as added. Although there is a greater stiffening in the PU foam bilayer systems, they still reduced the transmitted forces by as much as 32.4% at 5 J and 39.7% when compared to commercially available EVA and TPU foams that are currently used in the shoe industry. The drastic change in peak forces when adding the dense polyurea film was not

seen here as reported in Gupta and Youssef [44]. The reason is that the thickness and stiffness of the foams tested here are essentially optimized for this type of impact. Therefore, the addition of a dense polymer film will not contribute to the overall attenuation or a major change in pulse duration of the impact. However, as discussed in the following section, the dense polyurea film will indeed effect the rebound energy and displacement of the bilayer foam system.

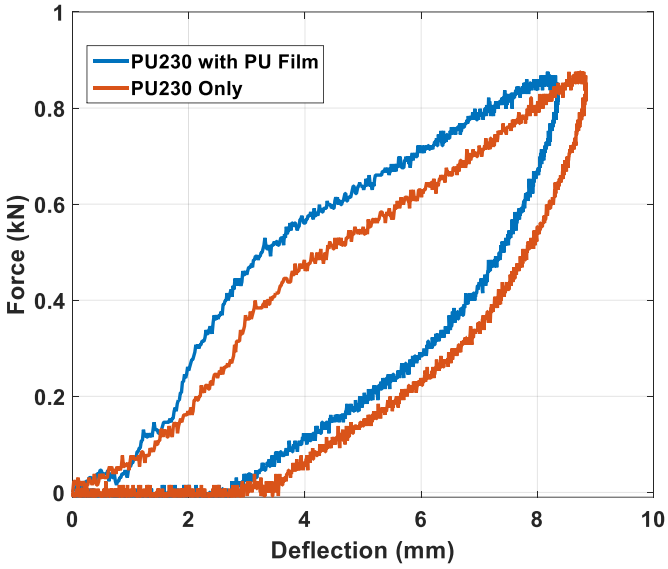


Figure 5.8: Typical force-deflection for PU foams at 5 J impact energy.

5.3.3 Rebound Energy and Displacement Results

In Figure 5.9 the relative rebound energy for PU, EVA, and TPU foams and their respective bilayers (addition of polyurea dense film) are shown. The relative rebound of the PU foams were found to increase with increasing density. The average relative rebound energy of the PU and PU foam bilayers was 35.1% and 41.5%, respectively. The EVA foams and EVA/PU Film bilayer show an average relative rebound energy of 56.3% and 57.0%, respectively. The TPU and TPU/PU film bilayer foams have an average relative rebound energy of 56.25% and 55.75%, respectively.

This means that for a given impact, the EVA and TPU foams are more elastic, meaning they can bounce back/recover faster and return back more of the stored compressional energy. Thus, there is a trade off in rebound energy and impact mitigation properties. The higher rebound energy in EVA and TPU foams result in higher impact forces as seen in previous Figures 5.4 and 5.5. The addition of polyurea dense film increases the relative rebound of the polyurea foams by 18%, making the rebound properties much closer to EVA and TPU foams. For EVA and TPU foams, the addition of the polyurea dense film does not change its rebound capabilities. Since EVA and TPU foams are quite efficient alone, the addition of the polyurea film decreases its rebound efficiency.

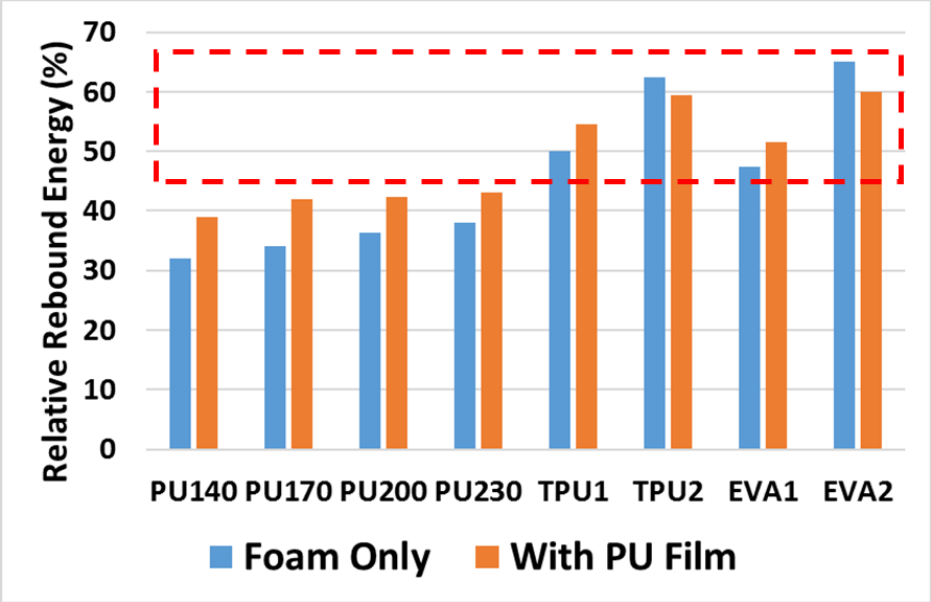


Figure 5.9: Relative rebound energy values for foam and bilayer samples.

Therefore, the addition of polyurea dense layer to the polyurea foams, the rebound energy (recovery and resiliency) are much closer to that of EVA and TPU foams. This additionally, makes

polyurea film/polyurea foam based systems attractive as midsoles in shoes since they provide much greater impact attenuation while providing similar recovery and resiliency as current foams.

Lastly, the max displacement in the foams and bilayer foam systems at a 5 J impact are shown in Figure 5.10. The results indicate that the maximum deflection in the polyurea foams fall within the range of both EVA and TPU foams under identical impact conditions. In addition, the polyurea dense layer decreases the displacement in the overall foam system by an average of 4%. Therefore, polyurea foams and polyurea film/polyurea foam bilayers can be used to adequately reduce the displacement of the midsole foam. This means that the addition of a dense layer or the use of polyurea bilayer systems can make the user's center of gravity moves less when walking or running, making it person potentially conserve additional energy.

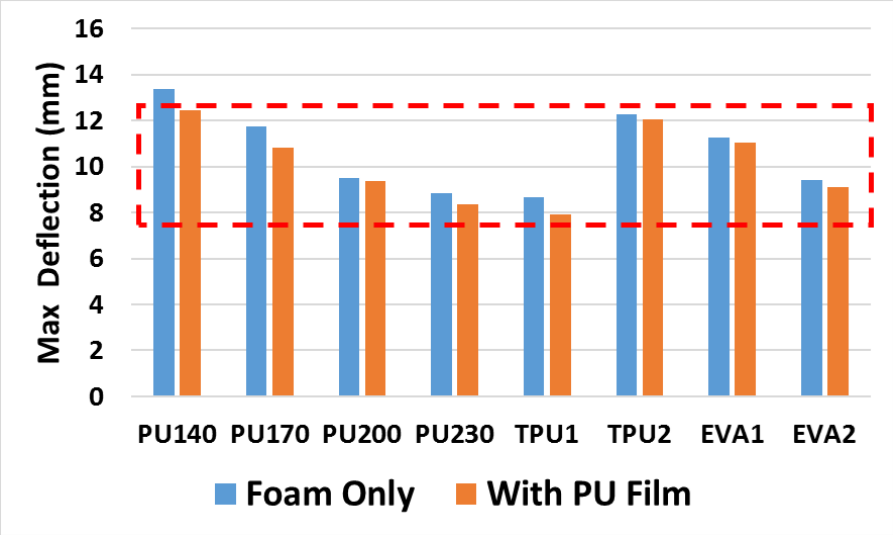


Figure 5.10: Maximum deflection of foam and bilayer system at a 5J impact energy.

5.4 Conclusions

In this study, the use of low density polyurea foams and polyurea film/foam bilayer systems as midsoles for footwear were examined. We have developed PU foams which yields the perfect balance between rebound and impact mitigation properties. In sections of 20 mm thicknesses, this material outperformed EVA and TPU foams of the same thickness in the ASTM F1976 standard shoe industry test by a significant margin. Further, polyurea film/foam bilayer systems showed the potential for an increase in rebound energy without sacrificing its impact mitigation properties. In addition, the polyurea dense film is able to reduce the amount of displacement within the foam system by making it stiffer as seen Figure 5.8. Therefore, polyurea foams and polyurea foam/film bilayers show a great potential in shock attenuation for midsoles.

CHAPTER 6

Mechanical Properties of Newly Developed Polyurea Based Foams

6.1 Introduction

In previous work, the stress-strain behavior on low density polyurea foams were conducted at low ($\leq 10^{-1}$ s^{-1}), intermediate ($\leq 10^{-1}$ s^{-1}), and high ($\geq 10^{3}$ s^{-1}) strain rate conditions. All foams exhibited an increase in Young's modulus, plateau stress, and decrease in densification strain under increasing strain. In addition, the energy absorption capabilities and temperature stability of polyurea foams were investigated under impact (drop-tower experiments and NOCSAE/FMVSS helmet standards). In this chapter, the effect of density on the mechanical foam properties (tensile strength, elongation, resiliency, compression set, tear strength, and hardness) are presented and compared to their widely used thermoplastic polyurethane counterparts. Test were conducted according to ASTM-D3574 [82] in order to better understand the behavior and performance of polyurea foams.

6.2 Materials

Polyurea foams of densities ranging from 120 kg/m^3 to 290 kg/m^3 where manufactured. SEM images of the PU foams can be seen in Figure 4.1. For foam manufacturing details, please refer to Chapter 5.2.

To determine PU's relative beavhior, thermoplastic polyurethane foams (TPU) were chosen as a reference material due to their heavy commercial presence. TPU foams with densities ranging from 150 kg/m^3 to 300 kg/m^3 were obtained commercially.

6.3 Experimental Methods

Each of the following tests was carried out as outlined in the ASTM- D3574 [82]. Three specimens were used to measure each property. The average values were calculated and recorded.

6.3.1 Hardness

The surface hardness of the PU and TPU foams were measured using an Asker C durometer. The sample dimensions for the hardness tests were 75 x 75 x 25 mm. The durometer has held in the center of the samples, away from the sample edges. Next, the durometer's pointer was pushed straight down, until the flat end of the durometer was in contact with the foam. The hardness value was measured and recorded within 1s of indentation as shown in Figure 6.1. Hardness is an important factor in cushioning, comfort level since it correlates to the amount of deflection for a given force and on how "hard" it feels.



Figure 6.1: Indentation test of PU foam using Asker C durometer.

6.3.2 Tensile Strength and Elongation

The tensile strength and elongation on all specimens were measured using a 2kN load frame (Instron Micro-Tester, Model 5942) equipped with a force transducer and displacement measuring device. Displacement controlled tension was used with a cross-head speed of 500 mm/min. Force-displacement data was obtained and converted to engineering stress-strain data using initial sample dimensions (Seen in Figure 6.2). The maximum stress and strain obtained were recorded as the tensile strength (MPa) and elongation (as a percent), respectively.

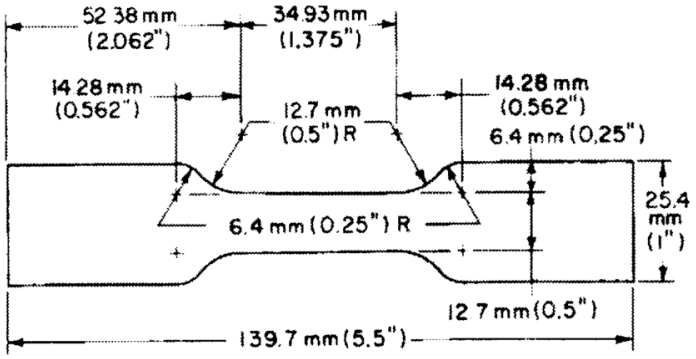


Figure 6.2: Tension specimen dimensions [82].

6.3.3 Compression Set

The compression set is the ability of a foam to return to its original thickness after being compressed over a specified amount of time and temperature. Compression set values indicate the percentage of the foam which did not recover, thus giving insight into the degredation of the material. Specimens were cut down to 50 mm x 50 mm x 25 mm blocks. The samples were compressed between two parallel plates, where the surface are of the plates were larger than that of the samples as shown in Figure 6.3. The samples were compressed to 50% of the initial thickness for 24hrs at 50˚C. The samples were then cooled allowed to recover for 30 minutes and the final thickness was measured and recorded. The compression set was calculated using following formula:

$$Compression\ Set\ \% = \left[\frac{t_o - t_f}{t_o}\right] x\ 100 \tag{6.1}$$

Where t_o is the original thickness and t_f is the final thickness.

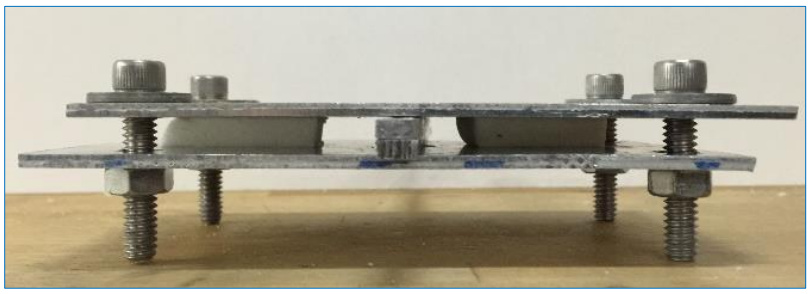


Figure 6.3: Compression set test set-up.

6.3.4 Resiliency

Resiliency is measured by dropping a 16 mm diameter steel ball from a height of 500 mm (Figure 6.4). The maximum rebound height of the steel ball after its impact with the foam is measured and

recorded. Resiliency is thus calculated as a percentage of the rebound height over the initial drop height. This test measures the instantaneous feel and bounciness of the foam or how active/response the foam behaves.

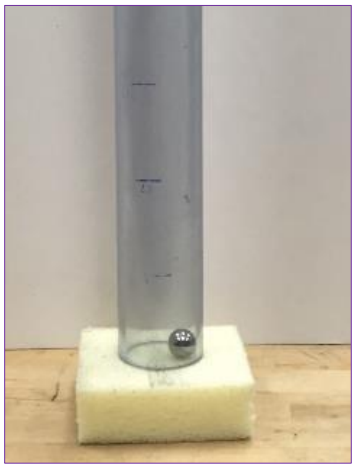


Figure 6.4: Resiliency test showing steel ball and plastic tube for measuring the rebound height.

6.3.5 Tear Strength

Tear strength measures the materials resistance to tearing and it is measured as a force per unit length (the thickness of the specimen). Two types of tear tests were conducted: the die-c and split tear test, with appropriate sample dimensions [82]. Figure 6.5 shows the different specimen shapes for split and die-c tear tests. In the split tear, a rectangular specimen with a center cut along its length is prepared, while in a die-c tear test, the specimen is cut into a C-shape. In both tests, the ends are clamped and pulled apart. In both cases, the tear strength can be calculated from the following expression:

$$Tear\ Strength = F/T \tag{6.2}$$

where F is the maximum force (N) recorded and T is the average thickness (mm) of the specimen. It is important to note that the die-c test refers to the force per thickness required for tear initiation, while the split tear refers to the force per thickness required to continue tearing the sample.

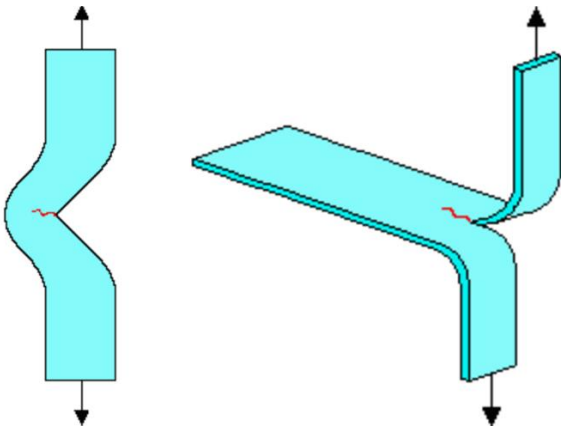


Figure 6.5: Tear strength specimens (*Left*) Die-C (*Right*) Split.

6.4 Results and Discussion

Figure 6.6 shows the effect of density on the hardness of PU and TPU foams. As the density increases, the hardness increases linearly for both PU and TPU having very similar properties. Lower density foams have larger cell sizes and thinner cell walls. In return, they are much easier to buckle and bend since they consist of mostly long and slender structures. Therefore, when indenting the foam with a durometer tip, it will see less resistance under compression and record lower hardness values.

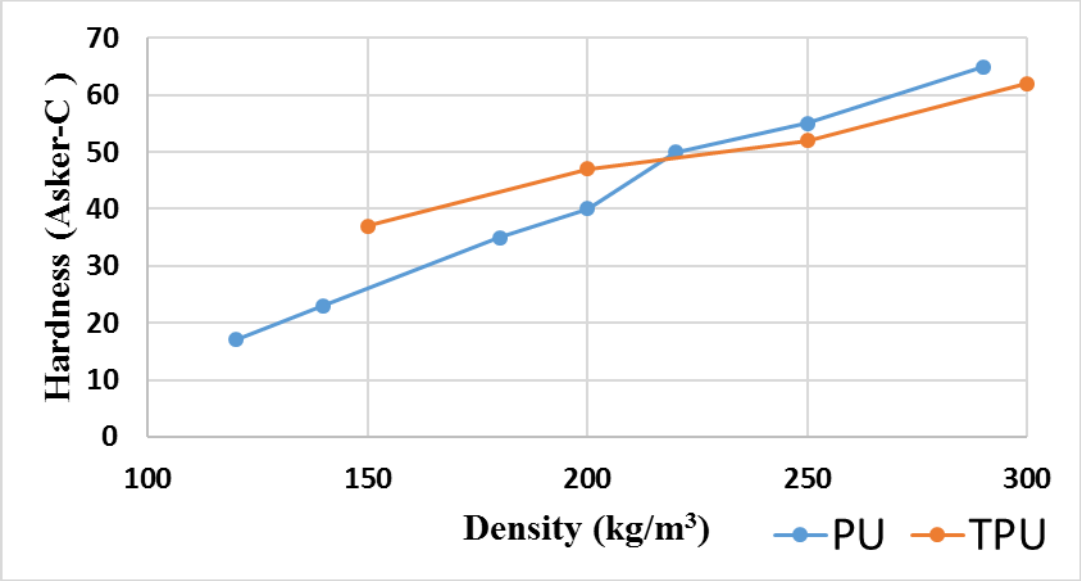


Figure 6.6: The effect of density on the hardness of PU and TPU foams.

The tensile strength of PU and TPU foams scale linearly with density while displaying similar strength values, as shown in Figure 6.7. In Figure 6.8 the elongation of both foam types are shown to be almost 300% at densities greater than or equal to 180 kg/m^3. At densities below 180 kg/m^3, PU foams display much lower elongation behavior (about 150%), while TPU foams retain their elongation.

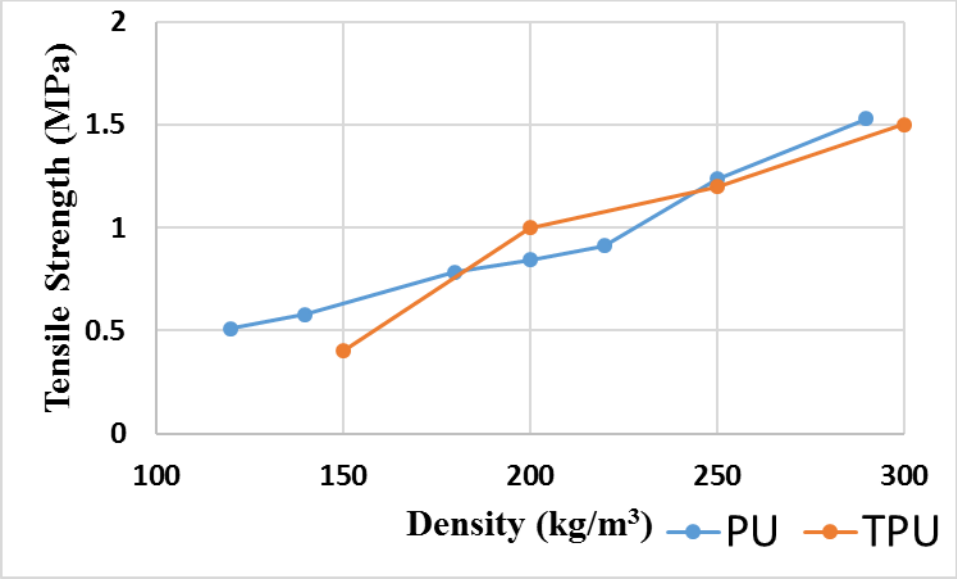


Figure 6.7: The effect of density on the tensile strength of PU and TPU foams.

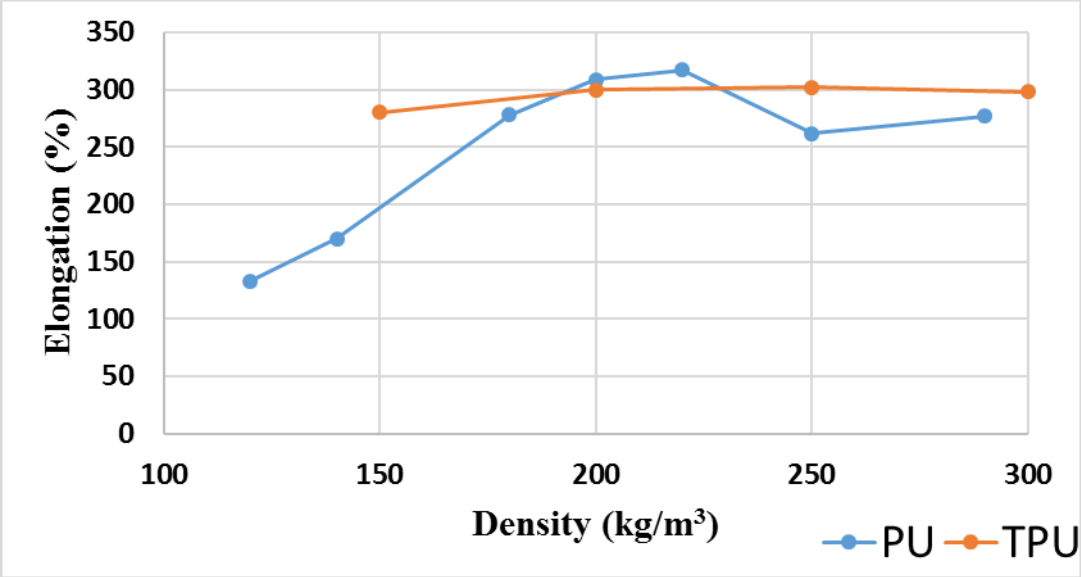


Figure 6.8: The effect of density on the elongation of PU and TPU foams.

One important indicator that corresponds to the degradation behavior of polymer foams under high temperature is the compression set, the percentage of foam thickness that does not

recover over prolonged compression). PU foams are far superior in their ability to recover to their original thickness than their TPU counterparts that experience greater inelastic behavior at elevated temperatures as shown in Figure 6.9. The compression set values for PU foams range from 7% to 35% at 50˚C, which is 40 to 85% less than TPU foams. The very low T_g of the polyurea (below -50 ˚C) and the stability of its hard and soft polyurea domains at elevated temperatures allow for the novel polyurea foams operate over a very wide range of temperature conditions. For the aformentioned reasons, the polyurea foams are able to recover from prolonged compression loadings under high temperatures when compared to other commercial foams. The resiliency in PU and TPU foams can be seen in Figure 6.10. The resiliency in both PU and TPU range from 32% to 40%, showing similar responsiveness/bounciness within the foam.

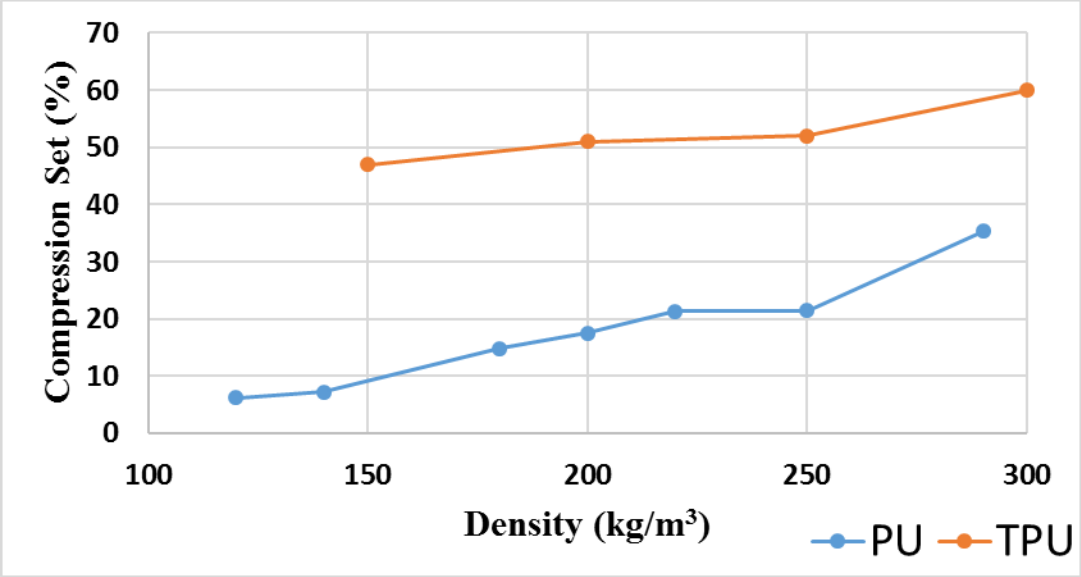


Figure 6.9: The effect of density on the compression set of PU and TPU foams.

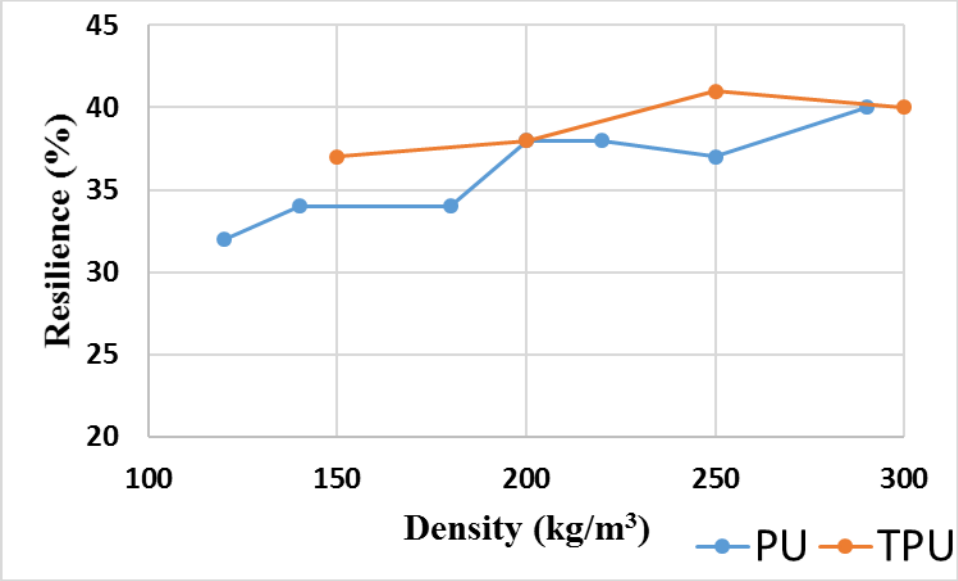


Figure 6.10: The effect of density on the resiliency of PU and TPU foams.

Figures 6.11 and 6.12 show a linear increase in split tear and die-c tear strength as a function of density in PU and TPU foams, respectively. It is observed that the die-c tear strength values are higher than split tear results. Interestingly, the die-c strength of both PU and TPU foams are very similar across all densities, however, PU foams have a higher split tear strength at densities above 180 kg/m^3. Therefore, it requires greater force per a given thickness of material to continue to tear the PU foams apart than TPU. The resultant values for all the mechanical properties of PU and TPU foams can be seen in Tables 6.1 and 6.2, respectively.

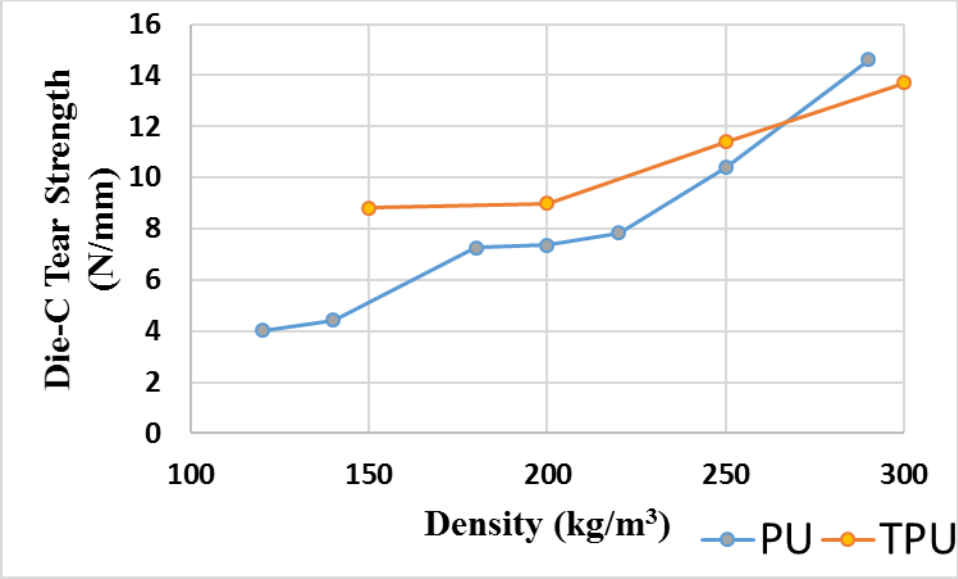


Figure 6.11: The effect of density on the Die-C tear strength of PU and TPU foams.

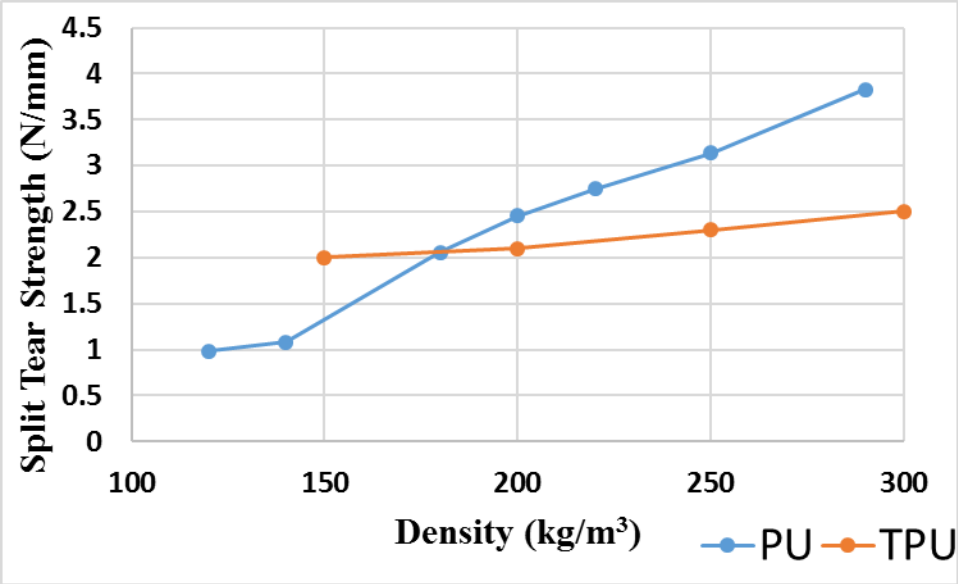


Figure 6.12: The effect of density on the Split Test tear strength of PU and TPU foams.

Table 6.1: The effect of density on the mechanical properties of PU foams.

Property	Density of Polyurea Foams (kg/m^3)						
	120	**140**	**180**	**200**	**220**	**250**	**290**
Hardness (Asker-C)	*17*	*23*	*35*	*40*	*50*	*55*	*65*
Tensile Strength (MPa)	*0.51*	*0.58*	*0.78*	*0.84*	*0.91*	*1.24*	*1.53*
Elongation (%)	*133*	*170*	*278*	*309*	*317*	*262*	*277*
Compression Set (%)	*6.2*	*7.2*	*14.8*	*17.5*	*21.3*	*21.5*	*35.3*
Resilience (%)	*32*	*34*	*34*	*38*	*38*	*37*	*40*
Die-C Tear Strength (N/mm)	*4.02*	*4.41*	*7.25*	*7.35*	*7.84*	*10.39*	*14.61*
Split Tear Strength (N/mm)	*0.98*	*1.08*	*2.06*	*2.45*	*2.75*	*3.14*	*3.82*

Table 6.2: The effect of density on the mechanical properties of TPU foams.

Property	Density of TPU Foams (kg/m^3)			
	150	**200**	**250**	**300**
Hardness (Asker-C)	*37*	*47*	*52*	*62*
Tensile Strength (MPa)	*0.4*	*1*	*1.2*	*1.5*
Elongation (%)	*280*	*300*	*302*	*298*
Compression Set (%)	*47*	*51*	*52*	*60*
Resilience (%)	*37*	*38*	*41*	*40*
Die-C Tear Strength (N/mm)	*8.8*	*9*	*11.4*	*13.7*
Split Tear Strength (N/mm)	*2*	*2.1*	*2.3*	*2.5*

6.5 Conclusion

The effect of density on the mechanical properties of polyurea foams were examined and compared to commercially available thermoplastic polyurethane foam counterparts. The hardness, tensile strength, elongation, resiliency, and tear strength for PU and TPU foams increase linearly with density while displaying very similar behavior. However, the compression set for PU foams are 40% to 80% less than their TPU counter parts. This is due to the low T_g of the polyurea (below -50˚C) and intrinsic the stability of its hard and soft polyurea domains at elevated temperatures.

Therefore, polyurea has the potential to replace TPU foams where both temperature stability and impact absorption (discussed in previous chapters) are needed, without compromising other mechanical properties such as strength and resiliency.

CHAPTER 7

Temperature-Stable, Novel, Viscoelastic, Composite Polyurea Foams for Impact Management

7.1 Introduction

In a previous chapters (Chapters 3-6), we presented polyurea-based strain rate sensitive viscoelastic foams that became increasingly more efficient in dissipating the impact energy as the loading rate was increased. Tests done using the Split-Hopkinson Bar setup showed that they dissipated more energy than the EPS72 foam at strain rates greater than 2000 s^{-1} while maintaining the peak stress below 1.5 MPa. With a T_g of -50°C, they were also able to maintain their ambient impact properties at low (-15°C) and high temperatures (50°C). These foams were however unable to outperform EPS72 foam at lower strain rates that are typically encountered in sports and by riders in motorcycle and bicycle accidents.

The purpose of this chapter is to introduce a composite foam concept that combines the novel microstructure of the previously developed PU foams with an open lattice structure with a network of mm-size struts to result in impact properties better than EPS72 even at lower rates of loading. These foams are viscoelastic and recover fully after each impact. The composite foam also inherits the low T_g and moisture and chemical resistance of the PU foam component. With these attributes, the composite foams presented here represent a major advance in this field and can potentially replace EPS foams that are ubiquitously used in a wide range of applications and industries.

The manufacturing and stress-strain characteristics for these composite foams is presented below under low ($\leq 10^{-1}$ s^{-1}) and intermediate (10^{1}-10^{2} s^{-1}) strain rates, and their performance compared with EPS72 and Poron320 foams to bring out the claimed advantages.

7.2 Material Preparation and Characterization

The composite foam was fabricated by taking a preform of polymer lattice that consisted of an open network of 2 mm-size struts (Figure 7.1) and foaming it through its open spaces. The raw materials for the free-rise foam component were prepared first. It consisted of preparing the B-side of the mix by taking the oligomeric diamine polyol and mixing it with appropriate amounts of deionized water, surfactants, cross-linkers, and catalysts to control the gelling and foaming reactions so as to obtain a free-rise foam of predetermined density. For the composite foams discussed here, a foam density of 112 kg/m^3 was selected. The A-side of the mix was the as-received modified Methylene Diphenyl Diisocyanate (MDI). The A and B sides were mixed in 1:4 weight ratio and poured into a 90 mm x 90 mm x 90 mm mold. Prior to cream time, which for this foam mix was 20 s, a slab of preformed lattice was lowered and fully submerged into the mix. The polyurea foam then rose through the open lattice spaces filling them completely. The rise ratio of the foam was between 7 and 8. Figure 7.2 shows the foaming and infiltration process of the preformed polymer lattice. Because of the high reaction exotherm, no curing was needed after the completion of the foaming and gelling reactions. The foam was completely tack free after 3 minutes. The entire composite foam block was removed from the mold, with sections cut from the center of the molded block to prepare specimens for mechanical testing, and characterization of physical and microstructural properties.

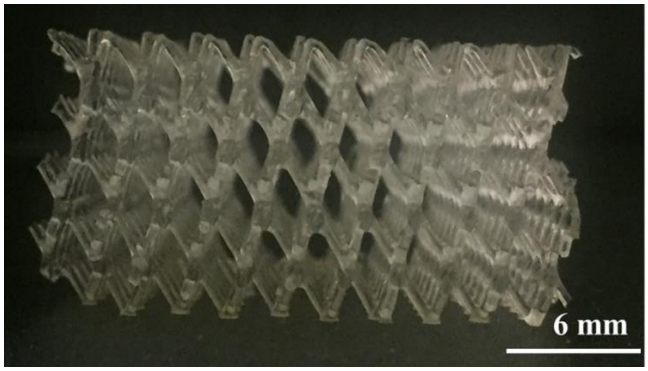


Figure 7.1: Preform polymer lattice.

The densities of the PU foam, lattice, and the final composite polyurea foam (CPF240) were measured to be 112 kg/m^3, 135 kg/m^3, and 240 kg/m^3, respectively. The density of the solid polyurea that formed the skeleton of the PU foam was 1070 kg/m^3.

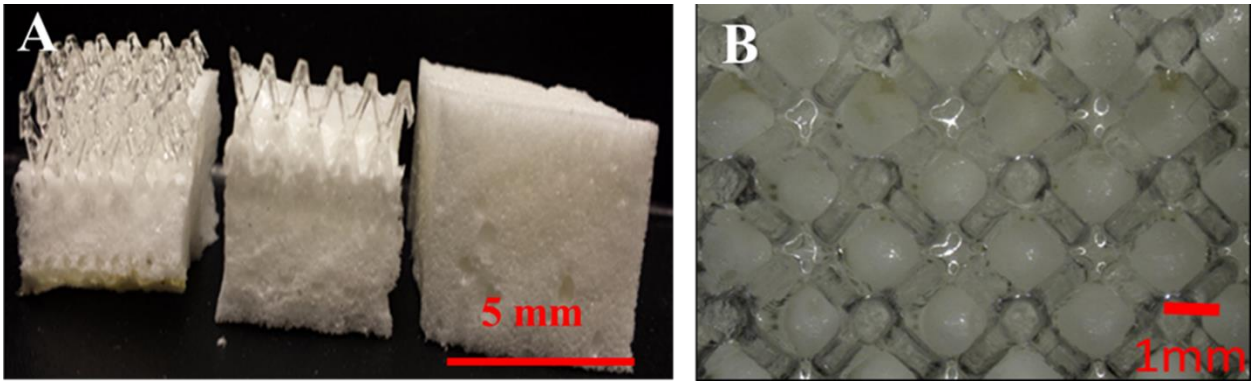


Figure 7.2: Foaming of preform lattice material to create composite polyurea foam (**A**) Side-view (**B**) Top-view.

The CPF240 samples were examined under a scanning electron microscope (SEM) prior to mechanical testing. Figure 7.3a shows the micrograph of a sectioned CPF240 sample. The dense shaded regions are sections through the lattice struts. The micrograph shows a complete filling of the lattice spaces by the PU foam, with strongly bonded interfaces. As discussed later, this is the

key to the composite foam's performance as the PU foam prevents instantaneous elastic buckling of the lattice struts by supporting them from both above and below. The struts continue to bend and deform gracefully in the post-buckle region, and in turn, relieves the pressure on the PU foam underneath. Thus, unlike traditional foams, composite foams have uniformly distributed regions that undergo tensile stretching even under uniaxial compression loading. On the continuum scale, this results in making the PU foam component more efficient in addition to dissipating energy through the post-buckled deformation of the struts.

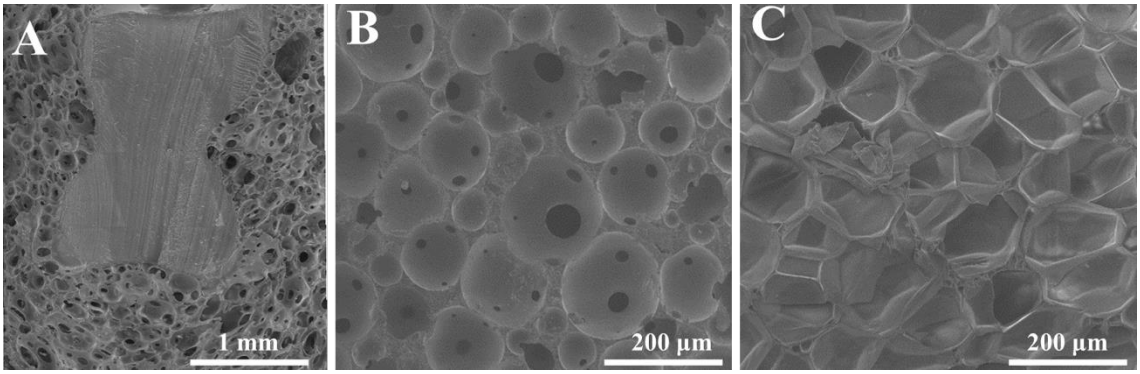


Figure 7.3: SEM Images of (A) CPF240 (B) Poron320 and (C) EPS72.

For comparing the performance of the CPF240 foams, EPS72 and Poron320 were chosen as representative foams that absorb energy through plastic crushing and phase transformation, respectively. EPS72 discs were obtained from the O'Neal Company while Poron320 was obtained commercially. Figures 7.3b and 7.3c show the SEM micrographs of these reference foams. EPS72 comprises of uniformly distributed irregular polyhedral closed cells with a nominal cell size of 160 µm whereas Poron320 has a uniform open cell size of 130 µm.

7.3 Experimental Methods and Procedures

7.3.1 Low and Intermediate Strain Rate Testing

Low strain rate ($\leq 10^{-1}$ s^{-1}) compression tests were conducted using an Instron Micro-Tester (Model 5942) equipped with a 2kN load frame. For these tests, disc samples of 28 mm nominal diameter and 10 mm thickness were cut from a large molded block. Samples were then compressed under stroke-control with a cross-head velocity of 24 mm/min in order to examine the material response over a quasi-static strain rate. These cross-head speed yielded a strain rate of 0.04 s^{-1}. Force-displacement data obtained from the machine was converted into the stress-strain data using the sample dimensions.

Intermediate strain rate (10^{1}-10^{2} s^{-1}) compression tests were carried out using an Instron DynaTup (Model 8250) drop-weight impact tester. Specimens with aforesaid dimensions were tested by placing them on a 45 mm-diameter flat force plate and impacted using a 5.5 kg balanced mass attached to a 75 mm-diameter flat stainless steel indenter head. The transmitted force was measured using a force transducer (Kistler Instruments, Model 9041A) with a full scale output of 90 kN and sensitivity of 4.3 pC/N. Impact energy was varied by changing the drop height of the indenter head. The displacement of the top sample surface during impact was also measured using high speed photography. The recorded force-displacement data was converted into engineering stress-strain characteristics using the initial sample dimensions. The strain rate ($\dot{\varepsilon}$) was calculated using Equation (7.1):

$$\dot{\varepsilon} = d\varepsilon / dt = \frac{d}{dt}\left(\frac{l - l_o}{l_o}\right) = \frac{1}{l_o}\left(\frac{dl}{dt}\right) = \frac{v}{l_o} \tag{7.1}$$

where v is the impact velocity and l_o is the specimen thickness. It should be noted that a constant strain rate is not attained in this experiment as the velocity of the falling mass is reduced during foam compression. However, the strain rate computed using the initial impact velocity and that calculated by differentiating the strain profile yielded only a 10% difference below 60% strain. Therefore, the strain rate up to 60% strain can be considered constant for all practical purposes. Data presented in this paper was gathered at a strain rate of 200 s^{-1}.

Impact experiments were conducted over a range of impact energies, from 5 J to 25 J in 5 J increments, at ambient (23°C) temperature. The tests at 15 J were repeated at cold (0°C) and hot (40°C) temperatures. In addition, they were impacted 3 times within a 30 s interval under ambient conditions to examine their multi-hit capability and subsequent recovery.

7.3.2 Reduction of Data: Energy Absorption Diagrams

An important part of the foam selection process is to keep the peak stress below a threshold level. For example, for head health applications, it must be kept below the brain injury threshold of 1 MPa [14]. To assist in this selection process, the strain energy density (*W)* for various foams is plotted as a function of the stress so that the user can select foam with the maximum energy density for the selected threshold stress. Another way to assist in this selection process is to plot the cushioning efficiency (*CE*) of the foam, defined as W/σ, as a function of the stress. When plotted, *CE* displays a peak at a specific stress; meaning that beyond this stress, *W* increases only slightly while the stress increases significantly. Therefore, for a threshold stress, foam with the maximum *CE* can be chosen. It is important to measure *W* and *CE* under the prevailing temperature and strain rate conditions in service as both of these parameters greatly influence the underlying stress-strain

characteristic of the foam material. In this paper we present the stress-strain characteristics for the CPF material over a wide range of strain rates and temperatures because the potential applications span several fields. We also compare their performance with EPS72 and Poron320 by carrying out industry standard impact tests where the foam selection is based on the lowest transmitted force (or acceleration) as the height and the weight of the falling impacter head are selected to mimic the worse impact experienced in that application. The NOCSAE football helmet and the DOT Helmet Standards are examples of such tests.

7.4 Results

7.4.1 Stress-Strain Characteristics

Figures 7.4 and 7.5 show the stress-strain behaviors of the CPF240 material along with two of its constituents (lattice-PL135 and polyurea foam-PU112) at quasi-static ($\dot{\varepsilon} = 0.04s^{-1}$) and dynamic ($\dot{\varepsilon} = 200s^{-1}$) strain rates, respectively. Figures 7.6 and 7.7 compare the CPF240 data with the EPS72 and Poron320 data at these two strain rates. Several features are noteworthy. First, CPF240 displays an almost linear stress-strain behavior all the way up to the densification region at the quasi-static strain rate. Thus, it does not display the classical plateau region exhibited by most foams. Under dynamic conditions (Figure 7.5), however, the material develops a plateau albeit in a somewhat serrated manner. The post-peak slopes of these serrations represent stable post-buckling behavior of the lattice struts and development of both compression and tension regions within the PU112 component. The PU foam sections that support the lattice struts from the top and prevents their instantaneous buckling, undergo tensile stretching, something that does not happen

during the compression loading of regular single-component foams. This also shields the PU foam regions that are underneath the struts and prevents their complete densification during loading. This interaction between the foam and struts is realized in Figure 7.5 through the formation of serrations. Complete densification occurs when the struts have completely buckled and the foam underneath is fully compressed. This occurs at a strain level of 72% as depicted by the flat region of the stress-strain characteristic in Figure 7.5. Beyond this strain, the stress rises rapidly, signaling full densification. It is noteworthy that at this stage the PU foam has regions that are under extreme tension and compression, and together, they provide a substantial restoring force to the buckled struts to assist in their snapping back once the impacter velocity has reduced to zero at the point of maximum foam compression. This is consistent with a significant reduction in the impulse time when compared to other foams as discussed below.

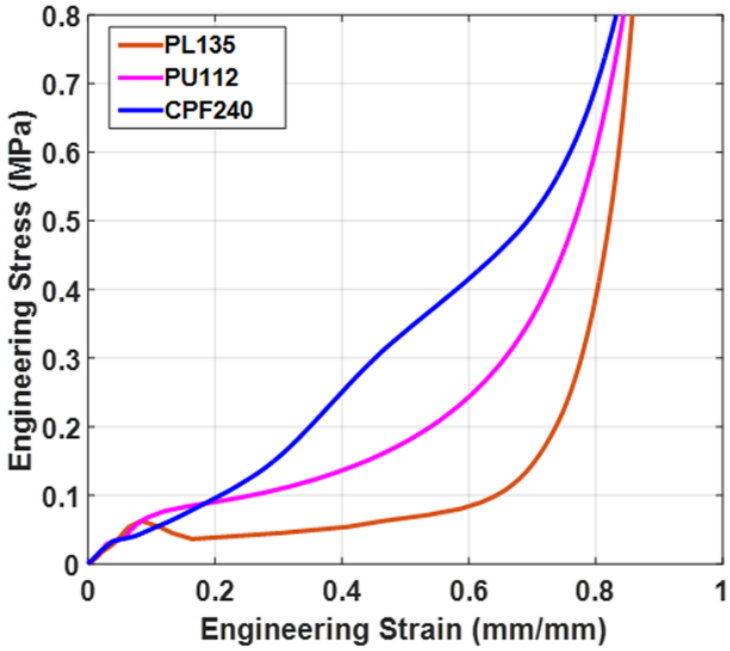


Figure 7.4: Quasi-static ($\dot{\varepsilon} = 0.04s^{-1}$) compressive stress-strain behavior of preform lattice-PL135, polyurea foam-PU112, and composite polyurea foam-CPF240.

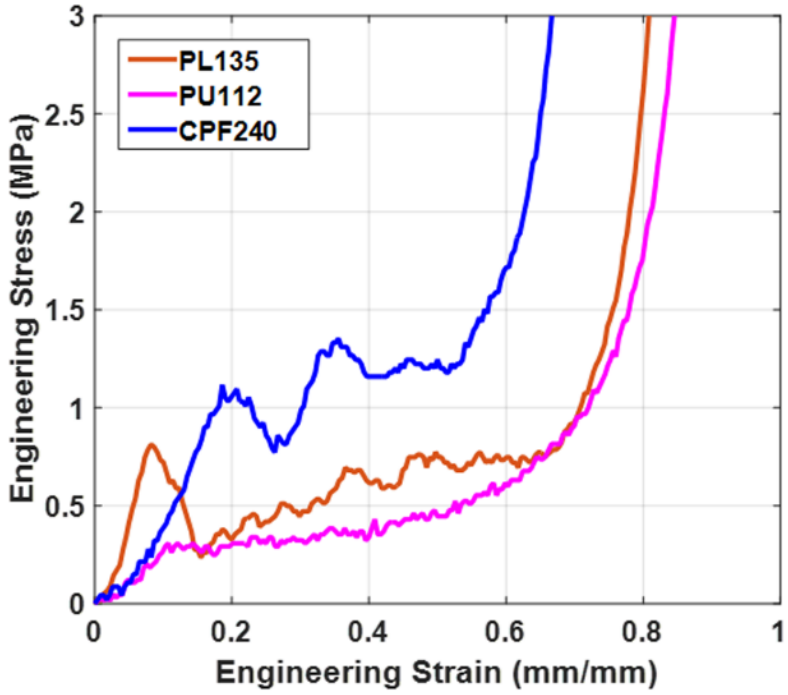


Figure 7.5: Dynamic ($\dot{\varepsilon} = 200s^{-1}$) compressive stress-strain behavior of preform lattice-PL135, polyurea foam-PU112, and composite polyurea foam-CPF240.

7.4.2 Strain Rate Effects

Figures 7.6 and 7.7 compare the CPF240 stress-strain characteristics with those of EPS72 and Poron320 at quasi-static ($\dot{\varepsilon} = 0.04s^{-1}$) and dynamic ($\dot{\varepsilon} = 200s^{-1}$) strain rates, respectively. Both CPF240 and Poron320 display a significant increase in both initial stiffness and plateau stress at the dynamic strain rate to result in their stress-strain characteristics similar to that of EPS72. This is remarkable as both Poron320 and CPF240 are viscoelastic and recover (see data below) fully after each impact whereas EPS absorbs energy through irreversible plastic crushing of its closed cells. They do so while keeping the peak stress below 2 MPa. Specifically, EPS72 and CPF240

have a plateau stress of about 1.0 MPa while Poron320 is around 1.5 MPa. The densification strain is 67%, 72% and 80% for Poron320, CPF240, and EPS72, respectively. The rate sensitivity of Poron320 comes from the shift in its *Tg* associated with strain rate based on the Time-Temperature Shift principle. It absorbs substantial energy as it undergoes rubbery-to-glassy phase transition. Since the transformation is reversible, upon unloading, the material recovers to its original state. This mechanism does not operate below *Tg* as the material already transforms into its hard glassy state. Since *Tg* for this material is between 0 and 5 °C, the material cannot be used for most sports and protective headgear applications. The strain rate sensitivity of the CPF240 material is intrinsically related to the microstructure of its PU112 foam component and as discussed later below operates well below freezing temperature because of its very low T_g. The microstructure comprises of large 300 to 500 μm polyhedral cells covered with perforated membranes with small apertures (47 μm nominal diameter). This makes the CPF240 strain rate sensitive as the rate at which the air escapes the cells through perforations depends upon the loading rate. At lower strain rate, typically at the start of the loading event, big cells simply collapse with air escaping freely through tiny perforations. This limits excess buildup of stress like any other viscoelastic foam. As the loading proceeds, both strain rate and level of material stress increases. During this phase, the rate at which the air escapes the cells cannot catch up with the rate of loading. Consequently, the air that remains inside each cell acts to stiffen the cell while the air that escapes adds to viscoelastic damping. Finally, when the impactor velocity has substantially reduced and the strain rate has dropped, the remaining undeformed cells collapse slowly, giving plenty of time for the air to escape freely through tiny perforations. Each cell thus acts like a time-dependent viscoelastic damper on the microstructural scale. Therefore, the PU foam is able to manage the varying material strain rate that occurs within the same loading event or different applications without the need to

modulate the material density or stiffness. In addition to the microstructure, energy is also dissipated by dynamic bending, twisting and rotation of the cell walls during impact like any other foam. Since the cell walls are made using the polyurea elastomer it adds further to the total energy absorption as it is by itself capable of absorbing the impact energy through sliding and stretching of its flexible molecular chains. The micro-phase segregation of hard and soft domains along with extensive hydrogen bonding present within the polyurea structure also grants it the ability to chemically tailor its mechanical toughness, resiliency, and hardness [29-44]. The polyurea chemistry chosen for the PU112 component was already optimized for maximum energy dissipation [29-44]. This strain rate strengthening mechanism is absent in the EPS as it has a closed-cell microstructure. The air trapped within the cells only contributes to the strength of the foam, independent of the strain rate [14]. This can be seen from Figures 7.6 and 7.7 which shows the same stress-strain behavior at both strain rates. It appears that the unique microstructure of newly developed composite polyurea foams essentially accomplishes the same stress-strain behavior as EPS and Poron technology, but without the material crushing or undergoing the phase shift.

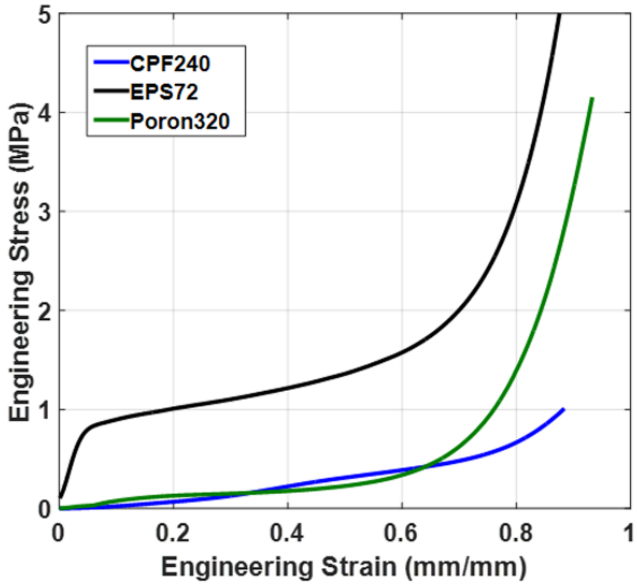


Figure 7.6: Quasi-static ($\dot{\varepsilon} = 0.04s^{-1}$) compressive stress-strain behavior of CPF240, EPS72, and Poron320.

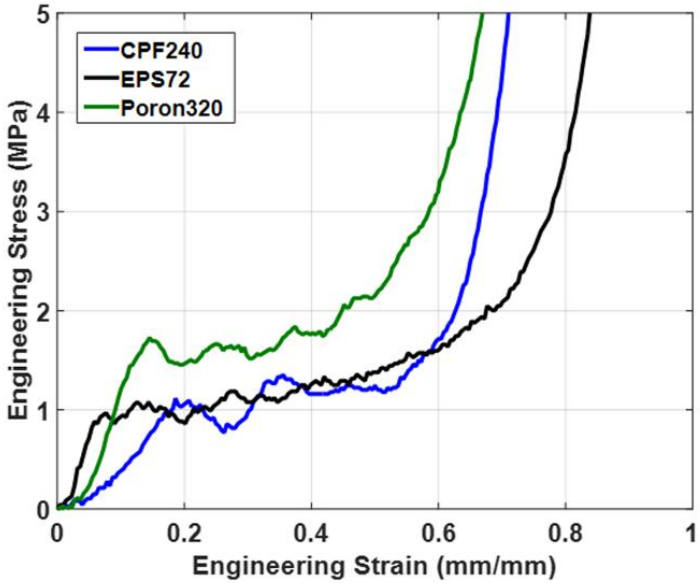


Figure 7.7: Dynamic ($\dot{\varepsilon} = 200s^{-1}$) compressive stress-strain behavior of CPF240, EPS72, and Poron320.

7.4.3 Energy Absorption Results

Figures 7.8 and 7.9 shows the plots of *W* and *CE* as a function of stress for the CPF240, EPS72, and Poron320 materials. Under quasi-static compression rates (Figures 7.8A and 7.9A), EPS72 has the highest energy absorption and cushioning efficiency compared to CPF240 and Poron320 at stresses ranging from 0.9 to 1.5 MPa. This however changes at the higher strain rate of 200 s^{-1} where both these foams display much higher energy absorption and cushioning efficiency at stress levels of 0.9 to 1.5 MPa and become comparable in performance to EPS72. It is noteworthy that such rates of loading are typically experienced in daily impacts and cover all contacts in sports and accidents and thus comparison of the impact data at these loading rates is most interesting. Figures 8B and 9B show that CPF240 absorbs the most energy at stress levels of 0.9 to 1.5 MPa.

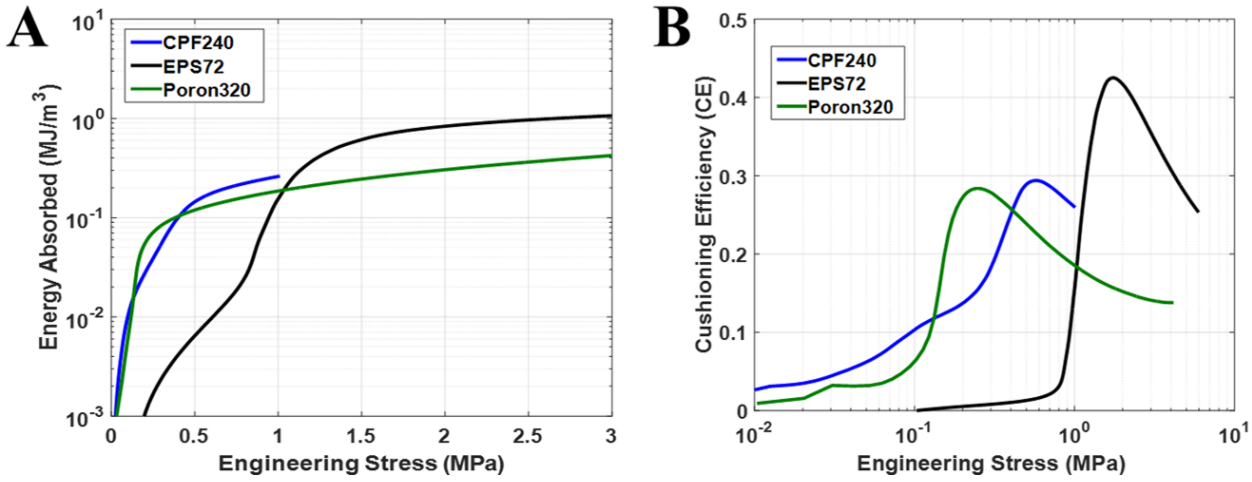


Figure 7.8: Quasi-static ($\dot{\varepsilon} = 0.04s^{-1}$) (A) energy absorption-W and (B) cushioning efficiency-CE as a function of stress for CPF240, EPS72, and Poron320.

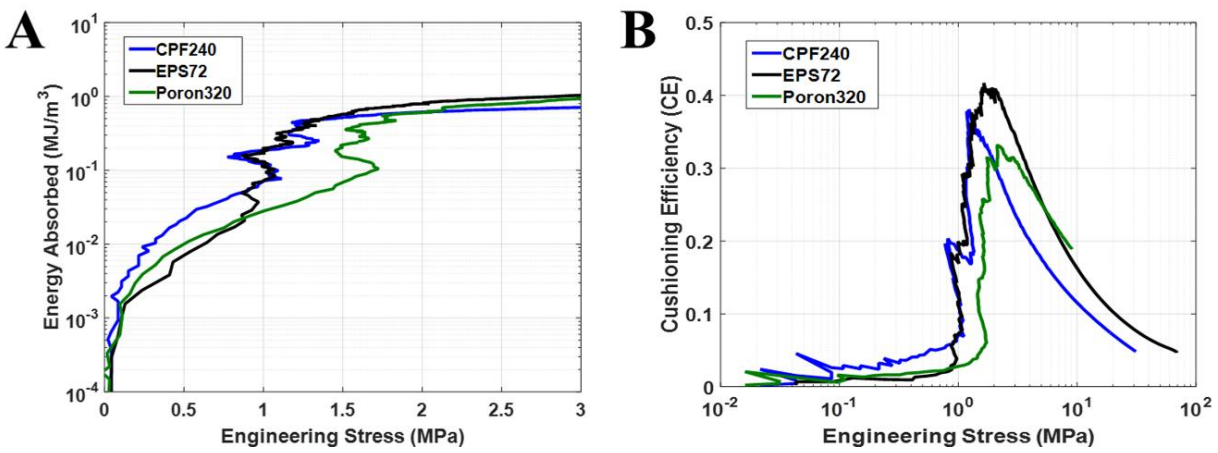


Figure 7.9: Dynamic ($\dot{\varepsilon} = 200s^{-1}$) (A) energy absorption-W and (B) cushioning efficiency-CE as a function of stress for CPF240, EPS72, and Poron320.

7.4.4 Impact Test Results

Figure 7.10 shows the average stress-time response for CPF240, EPS72, and Poron320 at different impact energies. The impact drop tower measures the transmitted force over time, however, they were converted to stress-time curves based on the impact area. This made it easier to interpret the results, compare the material performance with injury thresholds, and allowed correlating the impact energy from our tests to those used in the NOCSAE and DOT industry standard tests by matching the same level of local material stress.

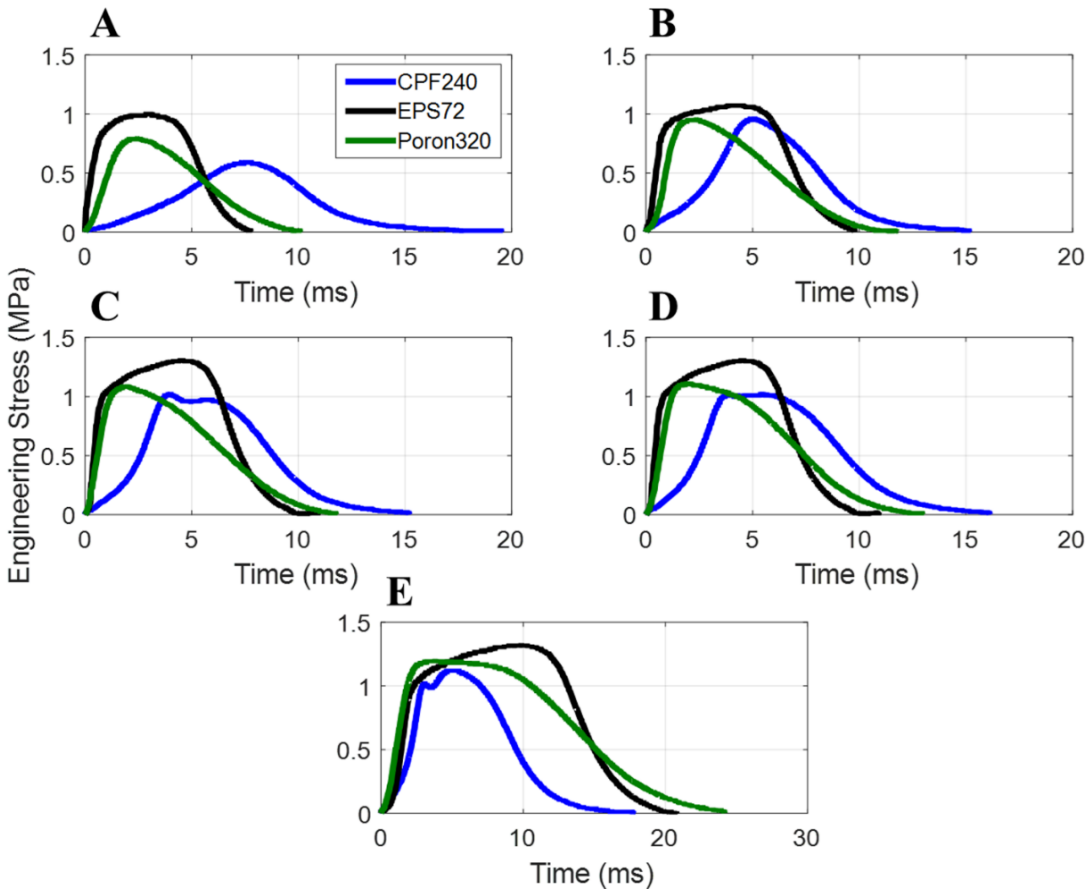


Figure 7.10: Stress-time history of CPF240, EPS72, and Poron320 samples impacted by (A) 5 J (B) 10 J (C) 15 J (D) 20 J and (E) 25 J energy.

In general, as the impact energy increases, the response of all foams tested displayed similar peak stresses with increasing impact duration which varied from foam to foam. The impact duration increases with impact energy as the material has not fully densified at lower energies. Interesting CPF240 displays the shortest impact duration. This, as discussed above, is related to the additional restoring force provided to the deformed struts of the lattice by the PU foam section that supports it from the top. These sections of the PU foam undergo maximum tensile stretching when the impacter comes to rest at the peak stress. This restoring force adds directly to that provided by the compressed section of the foam that is directly beneath the strut, and also to the

intrinsic elastic snapback that results from the elasticity of the deformed strut. Low impact duration means that CPF240 will be more effective in mitigating injuries based on the well-known Lebow study [67] and various severity indices that relate the potential of injury to both the peak stress and duration of loading.

Plots in Figure 7.10 also show that the CPF240 has a longer rise time to the peak transmitted stress compared to EPS72 and Poron320. This can be attributed to the decrease in stiffness of the composite foam under initial compression as seen in its stress-strain behavior (Figure 7.5). This is related to the compliance of the very large struts that start to deform at much lower stress levels. The slow buildup of stress is also advantageous as the body or brain is not subjected to very high stresses instantly as occurs with EPS72 and Poron320 foam materials.

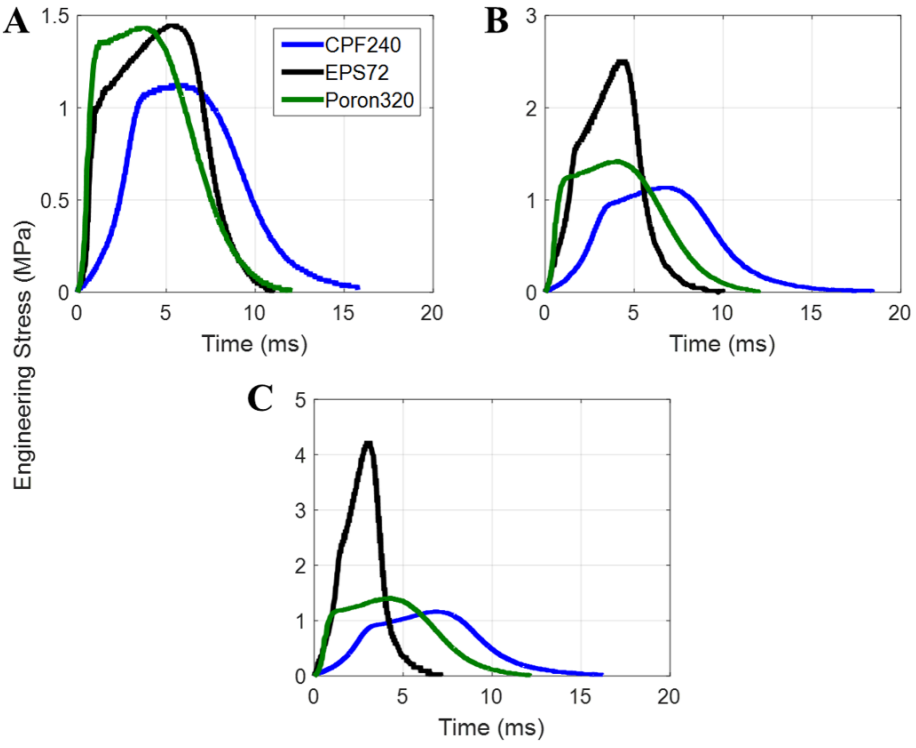


Figure 7.11: Stress-time history of CPF240, EPS72, and Poron320 samples impacted by 15 J energy (A) 1st hit, (B) 2nd hit, and (C) 3rd hit.

The peak transmitted stress at all impacted energy levels were lowest for CPF240 and were all below 1.5 MPa. EPS material absorbs energy through plastic crushing and therefore it cannot be re-used after first impact as its microstructure cannot recover to its un-deformed state. Quite remarkably the viscoelastic composite polyurea foam is able to absorb the same energy using the same section thickness and is also able to recover fully. This is demonstrated in Figure 7.11 which displays the impact data under multiple hit conditions. Data was gathered by hitting the same spot two additional times. The peak force for the composite polyurea foam and Poron material remains essentially unchanged whereas EPS stress increases significantly after the first hit. The multiple hit capability of the composite polyurea foam while absorbing impact energy at the same level as EPS material is truly a major advance. While Poron320 also has this advantage it unfortunately loses its energy absorption capability at moderately low temperatures. Figure 7.12 shows the results for impact test performed at different temperatures. At 0°C the Poron320 transmits a higher stress of 6.28 MPa compared to its room temperature value of 1.44 MPa whereas the peak stress for CPF240 rises from 1.13 MPa to 2.46 MPa, respectively. It is noteworthy that this increase in stress by the CPF240 comes from the lattice material having a much higher Tg. This can be easily circumvented by also making the lattice using the polyurea elastomer. Figure 7.12 also shows that Poron320 also falls apart at higher temperature of 40°C, tripling the transmitted stress over its ambient value. The lack of temperature stability prohibits use of Poron320 in most head health and body protection applications that requires performance over a range of temperature conditions.

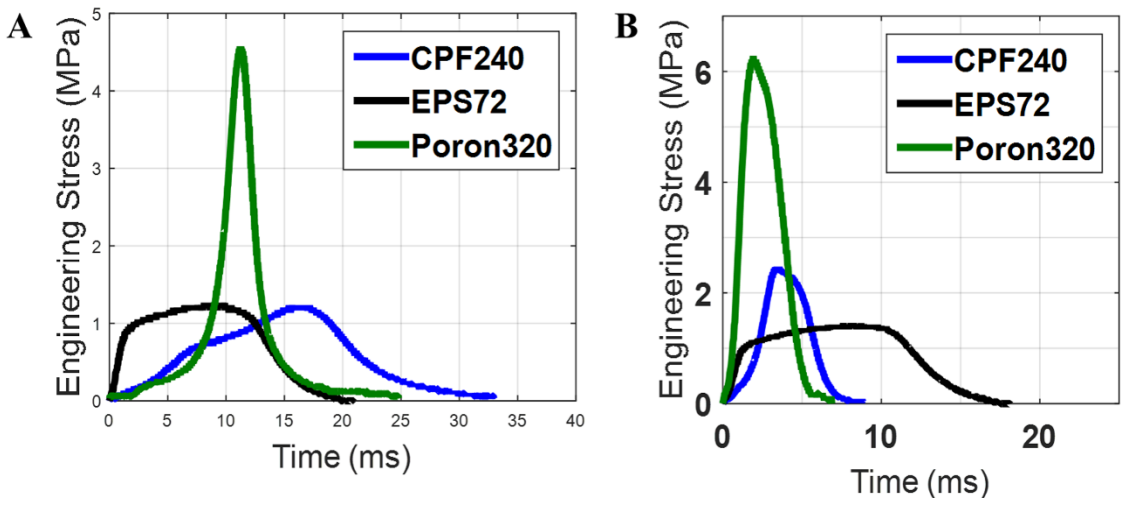


Figure 7.12: Stress-time history of CPF240, EPS72, and Poron320 samples impacted by 15 J energy at (A) 40°C and (B) 0°C.

Based on the above results, the composite polyurea foams presented here could potentially replace ubiquitously used EPS and Poron320 as it absorbs more impact energy at relatively low density in same section thicknesses while keeping both the peak stress and impulse duration low compared to its peers. Most importantly all this comes with low and high temperature stability and multiple-hit capability.

7.5 Conclusions

A new composite foam concept that involves infiltrating a polyurea-based foam through an open 3D lattice structure was introduced. A CPF240 sample with a density of 240kg/m^3 was chosen as a representative to discuss their stress-strain characteristics, energy absorption capabilities, and cushioning efficiency. Data was presented at quasi-static and dynamic strain rates using an Instron load frame and a drop tower facility, respectively. Results were compared with EPS72 (expanded

polystyrene foam with a density of 72 kg/m^3) and Poron320 (density of 320 kg/m^3) foams that represent high performance benchmarks for foams that absorb impact energy through plastic crushing and phase transformation mechanisms, respectively.

At loading rate of 200 s^{-1}, that are typically encountered in contact sports and accidents, CPF240 dissipated most energy and displayed the highest cushioning efficiency while still keeping the peak stress below the brain injury threshold level of 1.5 MPa. However unlike EPS72 which is a single-hit material as it undergoes irreversible plastic crushing after first impact, CPF240 recovers fully after each impact. While Poron320 provided similar energy absorption and multi-hit capability, it underperformed at low (0°C) and high temperatures (40°C) where the peak transmitted stress values were 6.28 MPa and 4.57 MPa, respectively, and thus making it inappropriate for head health applications where temperature stability is a major requirement. Remarkably, at both these temperatures, the peak transmitted stress of CPF240 were 2.46 MPa and 1.23 MPa, respectively. This temperature stability comes from the extremely low *Tg* of polyurea that forms the major component of the CPF240 composite foam. In fact, the deterioration in its impact properties at these extreme temperatures is due to the relatively high *Tg* of the polymer used for making the micro-lattice. This can be easily addressed by using polyurea to make the lattice which we plan to do in future work.

The unusual properties of the composite polyurea foam are a direct result of its novel microstructure that allows several energy absorbing mechanisms to operate synergistically and sequentially at varying length scales. Deformation at the largest scale involves the struts of the lattice that deform early in the loading history because of their compliance. As load increases, their increasing deformation is resisted by not only the polyurea foam that is directly underneath the

struts but most importantly the foam that supports it from the top. This allows for a stable post-buckling behavior of the struts and development of a uniformly distributed compression and tension regions inside the PU foam. Development of tension zones is unique to such foams. As already discussed, within these zones, the perforated cell wall structure of the PU foam acts as a set of microstructural viscoelastic dampers and makes the material strain-rate sensitive. This is the main energy dissipation mechanism. Lastly, the molecular structure of the polyurea elastomer participates in the energy dissipation process through relative shear sliding of its hard and soft segments, a process that becomes important when the microstructural elements within the PU foam cells bend, twist, and buckle at higher levels of densification strain. The restoring force on the deformed struts at the peak load when the indenter comes to a full stop is also significantly higher compared to regular foams especially because of the development of the tension regions. This is realized in the measured impact load-time histories with much shorter impulse durations especially at higher loads and impact energies. The combination of low peak stress and impulse duration is significant in the injury biomechanics field as the potential to cause bodily injuries increases with higher stress and longer impulse durations.

The composite concept allows tuning of the microstructure through proper choice of the lattice and PU foam components such that the peak stress can be limited to a predetermined threshold level, such as demonstrated here using the CPF240 foam which keeps the peak stress below the brain injury threshold limit of 1.2 MPa.

CHAPTER 8

Modeling the Compressive Stress-Strain Behavior of Polyurea Foams

8.1 Modeling of Cellular Solids

The compressive stress-strain behavior of a typical viscoelastic or a plastic foam exhibits three distinct regions: (i) a linear elastic region associated with cell wall bending, (ii) a stress plateau region that results from continuous collapse of the foam's cell structure on itself through non-linear fully recoverable (viscoelastic foams) or irrecoverable (plastic foams) buckling of its struts, and (iii) a densification region where the already-collapsed cells begin to compress against each other to near full density, resulting in a steeply rising stress. The amount of energy absorbed or dissipated by the foam is roughly equal to the area under its stress-strain curve. Therefore, predicting the compressive stress-strain behavior at different deformation rates is very important when dealing with impact applications.

8.1.1 Quasi-static Models

The most used and known stress-strain model for cellular solids under compression was presented by Gibson and Ashby [14]. The Gibson and Ashby model represents the foam's linear elastic, stress plateau, and densification regions by

$$\sigma = E\varepsilon \qquad when \quad \sigma \leq \sigma_{yield} \tag{8.1}$$

$$\sigma = \sigma_{yield} \qquad when \ \varepsilon_{yield} \leq \varepsilon \leq \varepsilon_D \left(1 - D^{-1/m}\right) \tag{8.2}$$

$$\sigma = \sigma_{yield}\ \frac{1}{D}\left(\frac{\varepsilon_D}{\varepsilon_D-\varepsilon}\right)^m \qquad when\ \varepsilon > \varepsilon_D(1-D^{-1/m}) \tag{8.3}$$

where E, σ_{yield}, and ε_D are the linear elastic Young's modulus, the initial plateau stress, and the densification strain, respectively, while D and m are curve fitting terms based on the densification strain. Although this model is widely used due to its simplicity, the drawback is that it discretizes the stress-strain behavior into three separate equations and it is non-continous at the boundaries of each region. In addition, the Gibson and Ashby model considers the plateau stress to be constant, when in most cases it's not.

Rusch [4-6] builds upon the idea that the stress is a product of the linear elastic region and the buckling-plateau region as follows

$$\sigma = E\varphi(\varepsilon) \qquad where\ \ \varphi(\varepsilon) = m\varepsilon^{-n} + r\varepsilon^{s} \tag{8.4}$$

where E is the Young's modulus and $\varphi(\varepsilon)$ is a shape function representation of the compressive strain during the plateau and densification region. This model is able to unify all three compressive regions into a single constitutive equation with a non-constant plateau stress, however, its drawback is that it does not accurately predict the densification region [13]. Liu and Subhash [83] suggested a six-term model to better accommodate the densification region given by

$$\sigma(\varepsilon) = A\frac{e^{\alpha\varepsilon}-1}{B+e^{\beta\varepsilon}} + e^{C}(e^{\gamma\varepsilon}-1). \tag{8.5}$$

While Avalle et. al [13] presented a five-term model as follows:

$$\sigma(\varepsilon) = A(1-e^{-\left(\frac{E}{A}\right)\varepsilon(1-\varepsilon)^m}) + B\left(\frac{\varepsilon}{1-\varepsilon}\right)^n \tag{8.6}$$

where A, B, and E are dependent on density, while m and n are not. More recently, Goga [84] described a new phenomenological model for foam materials using mechanical components such as springs and dashpots. The purpose of this model was to create a model to predict the stress-strain curve for polyurethane foam where each parameter is a function of density and correlates with the mechanical properties of the foam. Goga [84] foam model can be seen in Figure 8.1**.** The overall stress-strain behavior is captured by

$$\sigma(\varepsilon,\dot{\varepsilon}) = e^{\frac{-K\varepsilon}{C\dot{\varepsilon}}}\left(-1+e^{\frac{K\varepsilon}{C\dot{\varepsilon}}}\right)C\dot{\varepsilon} + \varepsilon K_P + \varepsilon\gamma(1-e^{\varepsilon})^n. \tag{8.7}$$

Although the models presented above are able to describe the entire nonlinear stress-strain characteristic of foam materials under large deformations, they does not include the effect of strain rate due to dynamic loading.

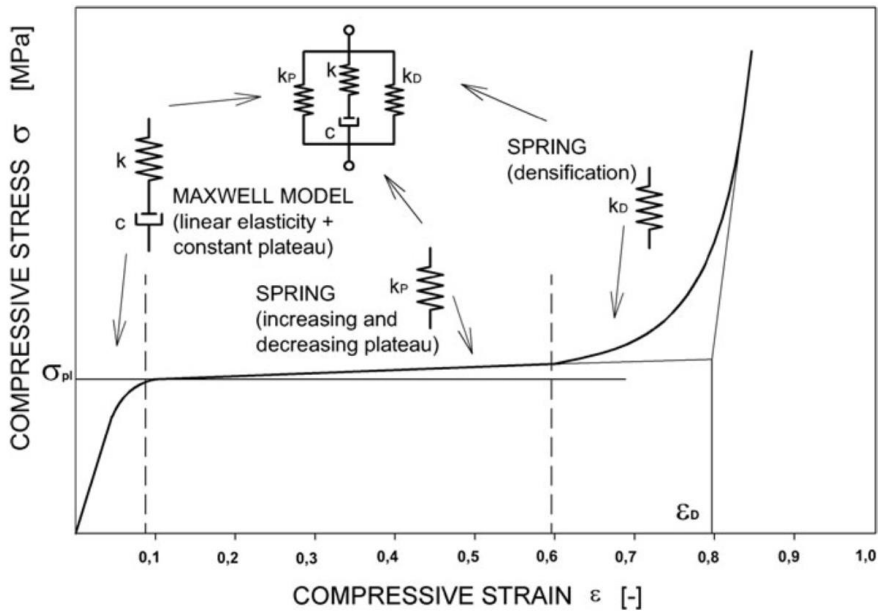


Figure 8.1: Stress-strain behavior of Goga foam model [84].

8.1.2 Dynamic Models

Although the previous models can be used to adequately represent the nonlinear stress-strain behavior of polymeric foams, they do not account for dynamic loadings. Nagy et al. [3] proposed a strain rate sensitive constitutive equation where the strain rate effect follows a power law model given by

$$\sigma = f(\varepsilon)\left(\frac{\dot{\varepsilon}}{\dot{\varepsilon}_0}\right)^{a+b\varepsilon} \tag{8.8}$$

where $f(\varepsilon)$ is any stress-strain shape function at a reference strain rate, $\dot{\varepsilon}_0$, while a and b are fitting constants by plotting multiple strain rate data in a log-log plot.

For low-density elastic polymeric foams subjected to high deformation rate impact loading, Jeong et al. [7] proposed a seven-parameter strain rate sensitive equation given by:

$$\sigma = \left\{A\left(1 - e^{-(E/A)\epsilon(1-\epsilon)^m}\right) + B\left(\frac{\epsilon}{1-\epsilon}\right)^n\right\}\left\{1 + (\mathrm{a} + \mathrm{b}\epsilon)\ln\left(\frac{\dot{\epsilon}}{\dot{\epsilon_0}}\right)\right\} \tag{8.9}$$

where the first five, E, A, B, m, and n are dependent on density while the remaining two parameters, a and b represent the strain rate sensitivity of the foam material. This strain rate function is able to describe the log-log plot of the stress versus strain rate as a nonlinear relationship, unlike previous models.

8.1.3 Chapter Objectives

In this chapter, we use the Goga [84] and Jeong [7] phenomenological foam models to compare the curve fit of the experimental compressive strain rate behavior of the newly developed polyurea foams under quasi-static and dynamic loadings.

8.2 Materials

Block samples of polyurea foams with densities of 140, 180, and 200 kg/m^3 were manufactured and are referred to as PU140, PU180, and PU200, respectively. Specimens were cut in cylindrical shapes having a 27.65 mm diameter and 20 mm thickness. Three specimens were prepared for each sample-type for studying the statistical variation. Please refer to Chapter 3.2 for details on foam manufacturing.

8.3 Experimental Methods

Low strain rate ($\leq 10^{-1}$ s^{-1}) and intermediate strain rate (10^{1}-10^{2} s^{-1}) compression tests were carried out according to Chapter 3.3.

8.4 Results and Discussion

8.4.1 Stress-strain Results

Figures 8.2-8.4 show the compressive stress-strain behavior at increasing deformation rates for 140, 180, and 200 kg/m^3 specimens, respectively. The quasi-static strain rates obtained were .004,

.04, and .4s^{-1}, while the dynamic strain rate obtained was 60s^{-1}. An increase in Young's modulus, plateau stress, and decrease in densification strain under increasing strain rate are observed.

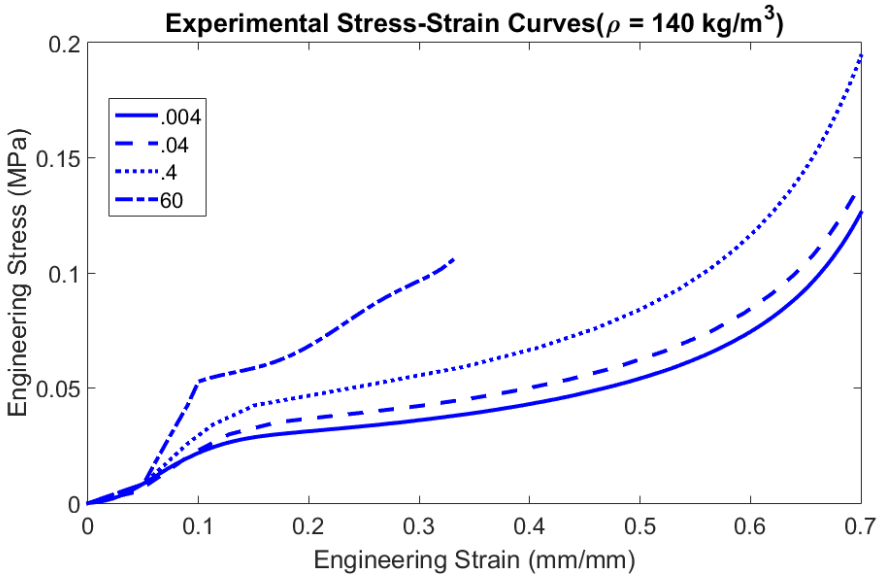


Figure 8.2: Stress-strain behavior of PU foam with density of 140 kg/m^3 at increasing strain rates.

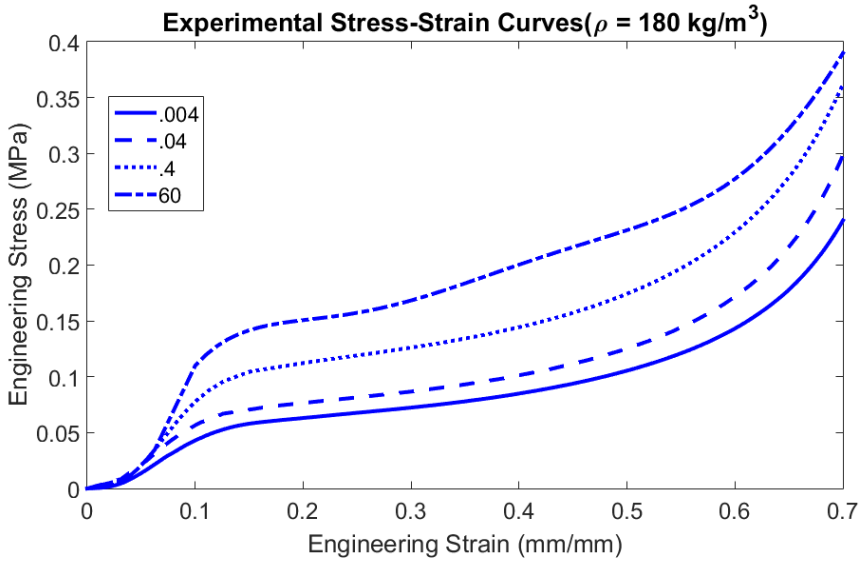


Figure 8.3: Stress-strain behavior of PU foam with density of 180 kg/m^3 at increasing strain rates.

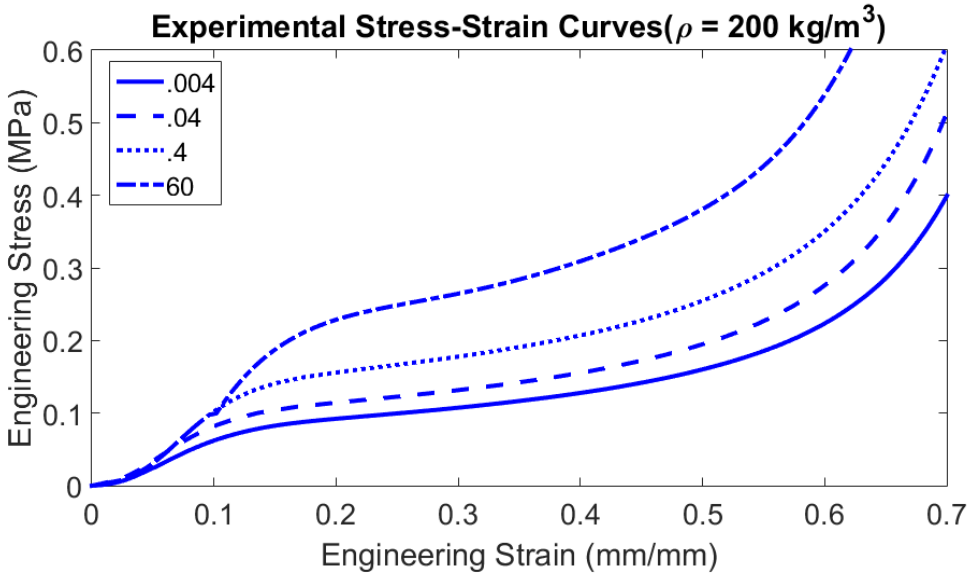


Figure 8.4: Stress-strain behavior of PU foam with density of 200 kg/m^3 at increasing strain rates.

8.4.2 Goga Foam Model Results

Figures 8.5-8.7 show the stress-strain behavior for experimental (blue line) versus Goga model (red dash line) for PU140, PU180 and PU200, respectively. The values corresponding to the Goga model are shown in Table 8.1. In general, the Goga model fits the experimental data very well. The energy per unit volume (area under the stress-strain curve) was calculated using the Goga model and compared with a numerical integration of the experimental curve. The difference in calculated energies ranged from 2-7%. The Goga model is therefore accurate in fitting the experimental data. From Table 8.1, the K and Kp values can be shown to correspond directly to the Young's' Modulus, and the slope of the plateau stress of the PU foams with calculated differences less than 5%, respectively. Therefore, the Goga model parameters are good indicators

of the foam properties. This is attributed to the use of mechanical components in its derivation, which directly correlates with the foam properties. The drawback is that the model does not consider strain rate. Table 8.1 shows that for each foam density and deformation rate, different parameters are needed. Hence, the model is only able to predict the compressive behavior under a constant strain rate.

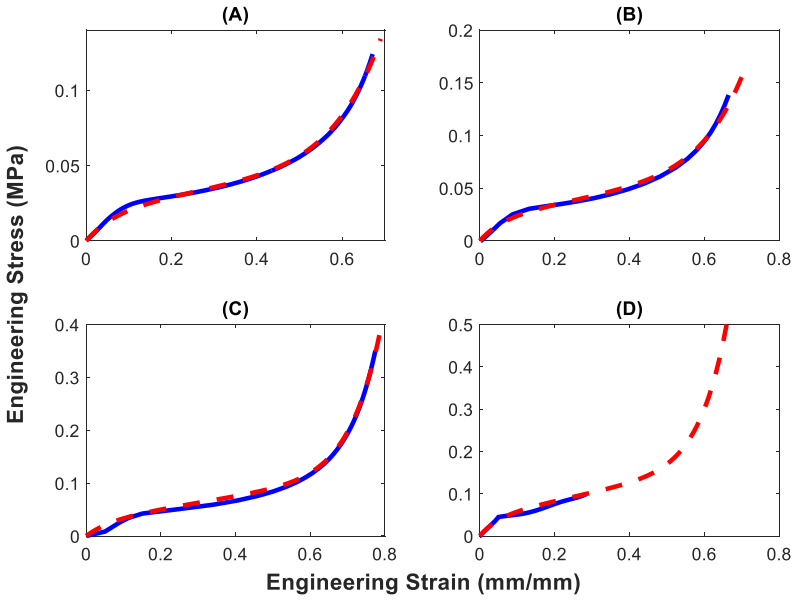


Figure 8.5: PU-140 kg/m^3 experimental data vs. Goga model (A) .004 (B) .04 (C) .4 (D) 60 s^{-1}.

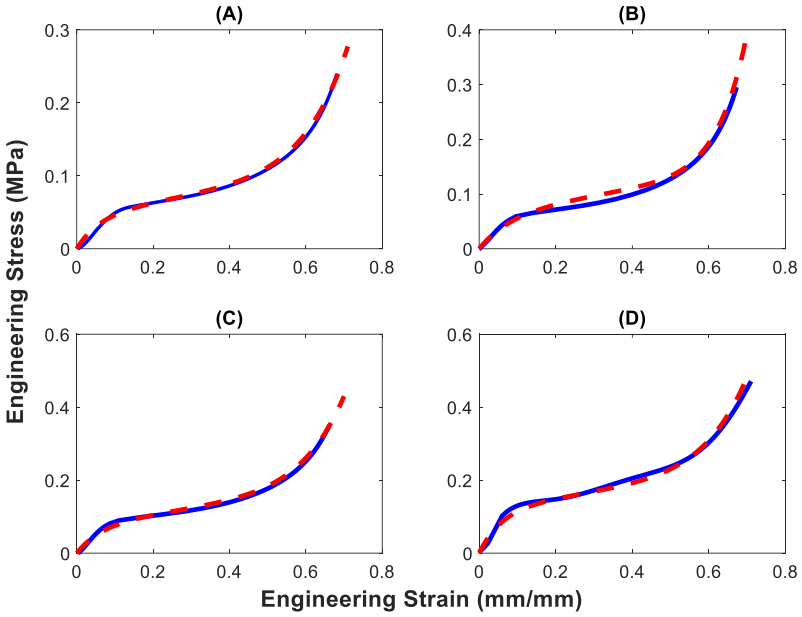


Figure 8.6: PU-180 kg/m^3 experimental data vs. Goga model (A) .004 (B) .04 (C) .4 (D) 60 s^{-1}.

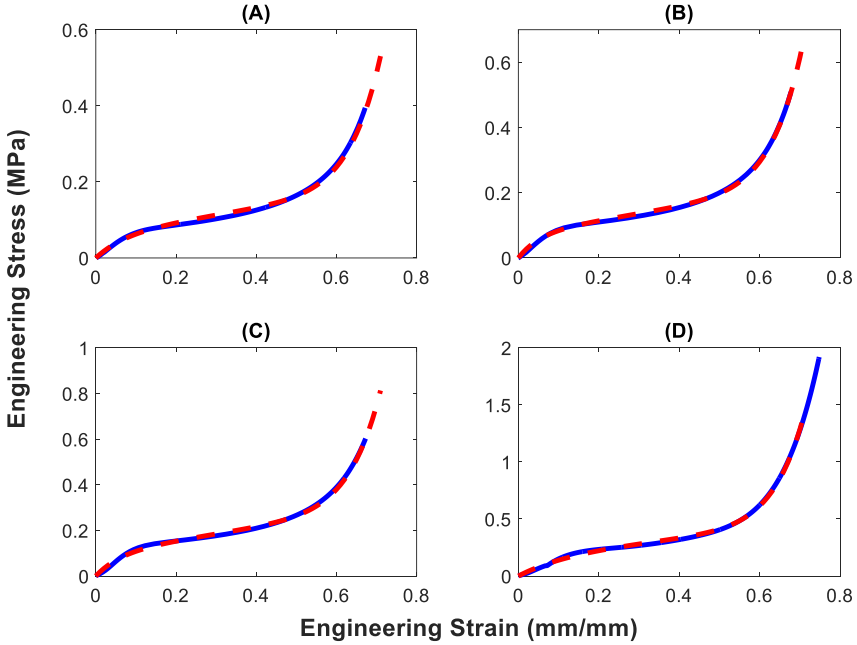


Figure 8.7: PU-200 kg/m^3 experimental data vs. Goga model (A) .004 (B) .04 (C) .4 (D) 60 s^{-1}.

Table 8.1: Goga constitutive model parameters for PU foams.

Foam	Strain Rate (s^{-1})	K (MPa)	C (MPa.sec)	Kp (MPa)	γ	n
PU140	0.004	0.28	4.7	0.055	0.115	4
PU140	0.04	0.33	0.51	0.072	0.155	4
PU140	0.4	0.41	0.07	0.117	0.115	6
PU140	60	0.88	0.007	0.198	0.75	6
PU180	0.004	0.55	11	0.10	0.20	4
PU180	0.04	0.75	1.6	0.114	0.33	6
PU180	0.4	1.17	0.19	0.158	0.33	4
PU180	60	2.01	0.002	0.161	0.34	4
PU200	0.004	0.81	15.7	0.17	0.40	6
PU200	0.04	1.4	1.85	0.208	0.52	6
PU200	0.4	1.6	0.25	0.283	0.59	6
PU200	60	1.6	0.003	0.386	1.1	6

8.4.3 Jeong Foam Model Results

Figures 8.8-8.10 show the stress-strain behavior for experimental (blue line) versus Jeong model (red dash line) for PU140, PU180 and PU200, respectively. The values corresponding to the Jeong model are shown in Table 8.2. In general, the Jeong model fits the experimental data very well. The energy per unit volume (area under the stress-strain curve) was calculated using the Jeong model and compared using numerical integration of the experimental curve. The difference in calculated energies ranged from 3-12%. Although the Jeong constitutive model is slightly less

accurate than the Goga model, it is able to predict the foam behavior under a dynamic loading at different strain rates while using only 5 parameters per each density foam. This significantly reduces the parameters needed to model different density foams under quasi-static and dynamic deformation rates. The drawback in this model is that the parameters do not correlate at all with foam material properties since the model is based simply on shape fitting.

Table 8.2: Jeong constitutive model parameters for PU foams.

Parameters	A	B	e	m	n	a	b
PU140	0.029	0.024	0.131	-9.019	1.60	0.095	0.039
PU180	0.096	0.020	0.524	0.381	2.41	0.219	-0.225
PU200	0.095	0.063	0.521	-4.84	1.84	0.114	0.073

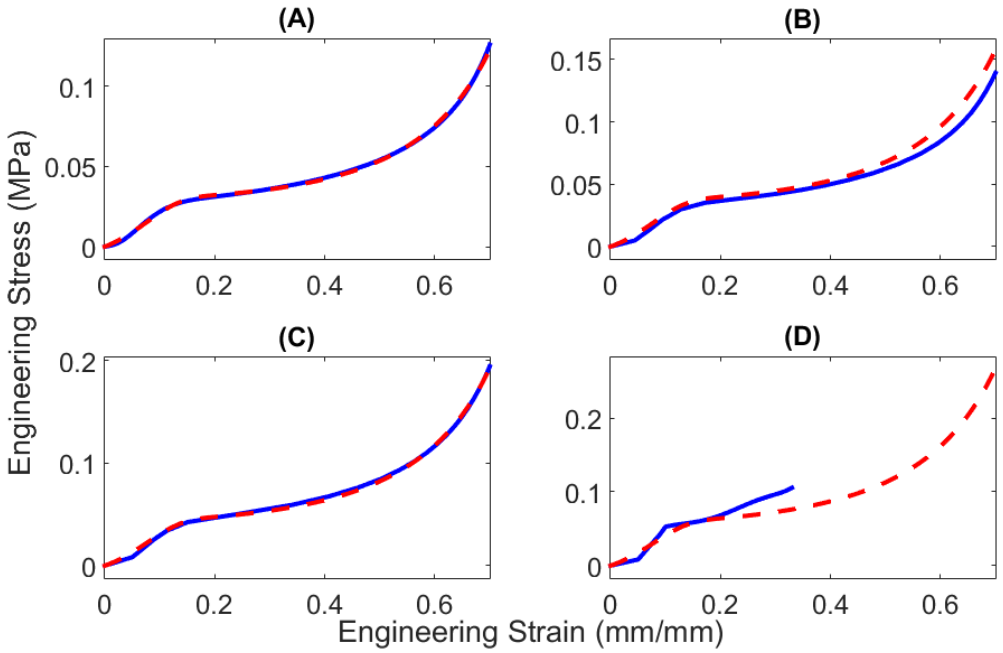


Figure 8.8: PU-140 kg/m^3 experimental data vs. Jeong model (A) .004 (B) .04 (C) .4 (D) 60 s^{-1}.

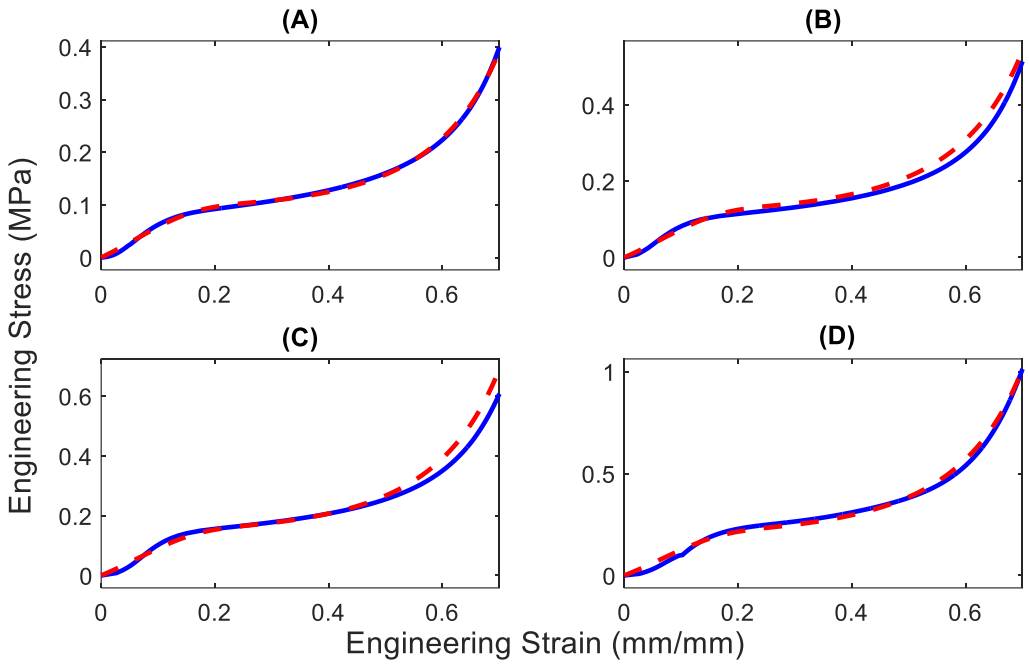


Figure 8.9: PU-180 kg/m^3 experimental data vs. Jeong model (A) .004 (B) .04 (C) .4 (D) 60 s^{-1}.

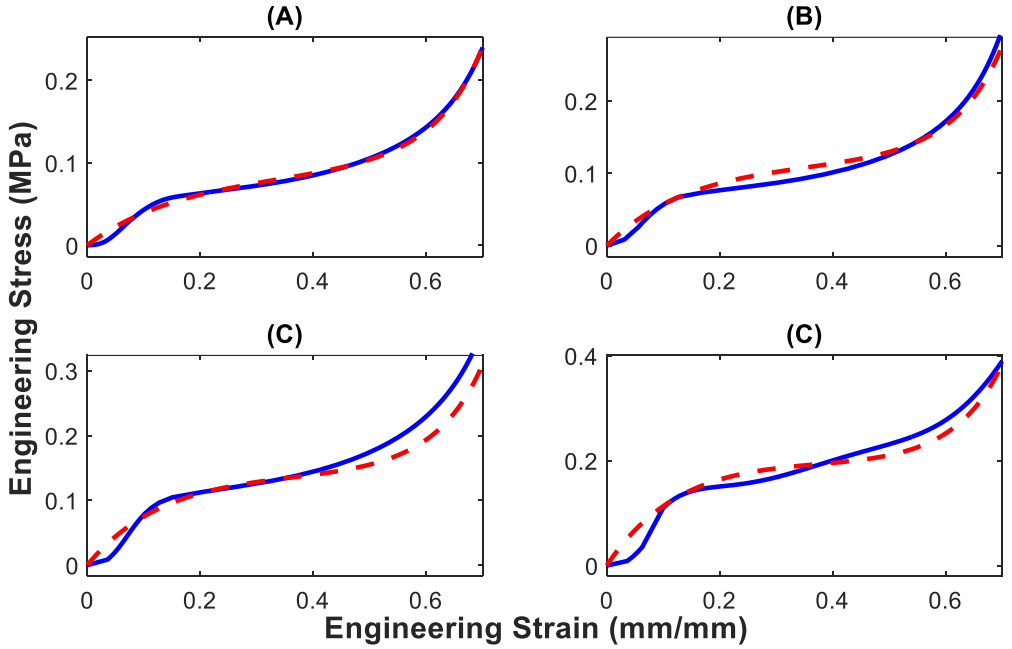


Figure 8.10: PU-200 kg/m^3 experimental data vs. Jeong model (A) .004 (B) .04 (C) .4 (D) 60 s^{-1}.

8.5 Conclusion

In summary, the stress-strain behavior of newly developed polyurea foams were investigated under quasi-static (10^{-2} s^{-1}) and intermediate (10^{2} s^{-1}) strain rate conditions. An increase in Young's modulus, plateau stress, and decrease in densification strain under increasing strain rate was observed for low-density PU foams. Additionally, the experimental results were compared with those of the Goga and Jeong constitutive models. When comparing the energy per unit volume between the experimental curves and the respective models, the differences ranged from 3-12%, showing good agreement with the experiments. The Jeong constitutive model is slightly less accurate (~3%) than the Goga model, however, it is able to predict the foam behavior under a dynamic loading at different strain rates while using only 5 parameters per each density. This significantly reduces the parameters needed to model different density foams under various deformation rates. Understanding the stress-strain behavior of strain rate sensitive foams can be used to design new materials for emerging impact application.

Chapter 9

Conclusions and Outlook

This works presents the development and characterization on novel low density (less than 250 kg/m^3) viscoelastic polyurea foams that retain their high energy absorption performance over a range of temperature (0°C to 40°C) and strain rates (50 s^{-1} to 5000 s^{-1}). The polyurea foam comprises of large polyhedral cells (300 μm -500 μm) covered with perforated membranes with small apertures (20 μm-70 μm). This makes the foam strain rate sensitive as the rate at which the air escapes the cells through perforations depends upon the loading rate. Thus, even with their uniform microstructure, they behave effectively as an elastically modulated layered composite because the cells stiffen or soften in response to the changing loading rate within the same impact event. This increase in the strength, provided by the cell wall aperture, also increases the energy absorption properties of the PU foams and makes them comparable to EPS type foam. Thus, polymer foams can be manufactured with large cell sizes (≥ 400 μm) and small aperture diameters (≤ 66 μm) to make them both low density and highly strain rate sensitive to absorb more energy than EPS. However, unlike EPS foams which are irreversible crushed after each impact PU foams recover fully after each impact and thus have multiple hit capabilities. This will allow these materials to have a wide range of military and aerospace applications, especially in advance armors and protective body and headgears that are subjected to blast shockwaves and impact from space debris and hypervelocity projectiles that emanate from IEDs.

Because of low T_g and its polyurea structure, the novel polyurea foams enjoy benefits of these dissipative processes at both very low (-15°C) and high (40°C) temperature conditions where their polyurethane/VN/Poron foam counterparts either become glassy or their structure deteriorate

so significantly that there is a substantial reduction in stiffness and a total loss of their impact properties. Consequently, at these extreme temperatures, the newly developed polyurea foams outperform VN foams and their products by a significant margin.

The combined benefits of temperature stability and rate sensitivity of low density ($\leq$ 200 kg/m^3) viscoelastic polyurea based foams were demonstrated by integrating them as liners into football, motorcycle helmets, and midsoles for athletic shoes. Polyurea foams showed promise in the reduction of head injuries and lower body limbs when used as foam liners helmets and midsoles in shoes, respectively, by showing an increase in reduction of transmitted gs by as much as 28% across the foam sections when compared to currently used foam systems.

Lastly, this thesis introduced a composite foam concept that combines the novel microstructure of the previously developed PU foams with an open lattice structure with a network of mm-size struts to result in impact properties better than Expanded Polystyrene foam systems even at lower rates of loading. These foams are viscoelastic and recover fully after each impact. The composite foam also inherits the low T_g and moisture and chemical resistance of the PU foam component. With these attributes, the composite foams presented here represent a major advance in this field and can potentially replace EPS foams that are ubiquitously used in a wide range of applications and industries.

While great strides have been made in the in the development of low density (less than 250 kg/m^3) *viscoelastic* polyurea foams with high energy absorbing capabilities, there still exist a challenge in controlling the microstructure of foams, to obtain specific spatially varying properties. In general, foams are produced by a stochastic process, thus their properties are mainly a function of porosity and bulk behavior. It is therefore highly desirable to create a new class of high

performance materials whose microstructure can be tuned to respond to specific threats. Thus, the future goals would be to design and test new materials with tailored microstructural anisotropy that can absorb a larger amount of energy during impact. This can possibly be done with the new advancements in small-scale additive manufacturing and 3D printing technologies.

References

[1] M. Avalle, G. Belingardi, and R. Montanini, International Journal of Impact Engineering 25, 445 (2001).

[2] M. R. Shorten and J. A. Himmelsbach, The Engineering of Sport 4, 152 (2002).

[3] A. Nagy, W. L. Ko, and U. S. Lindholm, Journal of Cellular Plastics 10, 127 (1974).

[4] K. C. Rusch, Journal of Applied Polymer Science 14, 1433 (1970).

[5] K. C. Rusch, Journal of Applied Polymer Science 13, 2297 (1969).

[6] K. C. Rusch, Journal of Applied Polymer Science 14, 1263 (1970).

[7] K. Y. Jeong, S. K. Cheon, and M. B. Munshi, Journal of Mechanical Science and Technology 26, 2033 (2012).

[8] M. F. Alzoubi, S. Al-Hallaj, and M. Abu-Ayyad, Journal of Solid Mechanics 6, 82 (2014).

[9] S. Ouellet, D. Cronin, and M. Worswick, Polymer Testing 25, 731 (2006).

[10] M. C. Saha, H. Mahfuz, U. K. Chakravarty, M. Uddin, M. E. Kabir, and S. Jeelani, Materials Science and Engineering: A 406, 328 (2005).

[11] B. Song, W. W. Chen, S. Dou, N. A. Winfree, and J. H. Kang, International Journal of Impact Engineering 31, 509 (2005).

[12] J. Zhang, Z. Lin, A. Wong, N. Kikuchi, V. C. Li, A. F. Yee, and G. S. Nusholtz, Journal of Engineering Materials and Technology 119, 284 (1997).

[13] M. Avalle, G. Belingardi, and A. Ibba, International Journal of Impact Engineering 34, 3 (2007).

[14] L. J. Gibson and M. F. Ashby, Cellular Solids: Structure and Properties, Cambridge University Press, 1999.

[15] N. Mills, Polymer Foams Handbook: Engineering and Biomechanics Applications and Design Guide, Butterworth-Heinemann, 2007.

[16] S. Hayes and P. Venkatraman, Materials and Technology for Sportswear and Performance Apparel, CRC Press 2015.

[17] M. R. Shariatmadari, R. English, and G. Rothwell, Mater. Des. 37, 543 (2012).

[18] D. V. Dounis, and G. L. Wilkes, Polymer 38, 2819 (1997).

[19] D. Klempner, and K. C. Frisch, Handbook of Polymeric Foams and Foam Technology, Hanser, 1991.

[20] R. Herrington, and K. Hock, Flexible Polyurethane Foams Dow Chemical Co, Midland, MI (1998).

[21] C. Briody, B. Duignan, and S. Jerrams, Constitutive Models for Rubber 7, 143 (2011).

[22] C. Briody, B. Duignan, S. Jerrams, and J. Tiernan, Computational Materials Science 64, 47 (2012).

[23] Y. He, D. Xie, and X. Zhang, Journal of Materials Science 49, 7339 (2014).

[24] M. Grujicic, B. Pandurangan, T. He, B. A. Cheeseman, C-F. Yen, and C. L. Randow, Materials Science and Engineering: A 527, 7741 (2010).

[25] D. Fragiadakis, R. Gamache, R. B. Bogoslovov, and C. M. Roland, Polymer 51, 178 (2010).

[26] T. Choi, D. Fragiadakis, C. M. Roland, and J. Runt, Macromolecules 45, 3581 (2012).

[27] K. Holzworth, Z. Jia, A. V. Amirkhizi, J. Qiao, and S. Nemat-Nasser, Polymer 54, 3079 (2013).

[28] Z. Jia, A. V. Amirkhizi, K. Holzworth, and S. Nemat-Nasser, Springer International Publishing 2, 17 (2014).

[29] J. Yi, M. C. Boyce, G. F. Lee, and E. Balizer, Polymer 47, 319 (2006).

[30] A. V. Amirkhizi, J. Isaacs, J. McGee, and S. Nemat-Nasser, Philosophical Magazine 86, 5847 (2006).

[31] C. M. Roland, J. N. Twigg, Y. Vu, and P. H. Mott, Polymer 48, 574 (2007).

[32] J. Shim and D. Mohr, International Journal of Impact Engineering 36, 1116 (2009).

[33] S. S. Sarva, S. Deschanel, M. C. Boyce, and W. Chen, Polymer 48, 2208 (2007).

[34] T. Jiao, R. J. Clifton, and S. E. Grunschel, AIP Publishing 1195, 1229 (2009).

[35] T. Jiao, R. J. Clifton, and S. E. Grunschel, AIP Publishing 955, 707 (2007).

[36] G. Youssef and V. Gupta, Journal of Materials Research 27, 494 (2012).

[37] M. R. Amini, J. B. Isaacs, and S. Nemat-Nasser, International Journal of Impact Engineering 37, 82 (2010).

[38] M. R. Amini, J. B. Isaacs, and S. Nemat-Nasser, Mechanics of Materials 42, 628 (2010).

[39] M. R. Amini, J. B. Isaacs, and S. Nemat-Nasser, Mechanics of Materials 42, 615 (2010).

[40] A. Jain and V. Gupta, Mechanics of Materials 46, 16 (2012).

[41] A. Jain, G. Youssef, and V. Gupta, Journal of Adhesion Science and Technology 27, 403 (2013).

[42] H. Kim, J. Citron, G. Youssef, A. Navarro, and V. Gupta, Mechanics of Materials 45, 10 (2012).

[43] J. Citron, J. University of California, Los Angeles, Dissertation, 2012.

[44] V. Gupta and G. Youssef, Experimental Mechanics 54, 1133 (2014).

[45] H. J. Qi and M. C. Boyce, Mechanics of Materials 37, 817 (2005).

[46] T. Reppel, T. Dally, and K. Weinberg, Technische Mechanik 33, 19 (2013).

[47] C. M. Roland, D.Fragiadakis, R. M. Gamache, and R. Casalini, Philosophical Magazine 93, 468 (2013).

[48] C. Li and J. Lua, Materials Letters 63, 877 (2009).

[49] W. G. Knauss and J. Zhao, Mechanics of Time-Dependent Materials 11, 199 (2007).

[50] J. Zhao, W. G. Knauss, and G. Ravichandran, Mechanics of Time-Dependent Materials 11, 289 (2007).

[51] G. Youssef and V. Gupta, Mechanics of Time-Dependent Materials 16, 317 (2012).

[52] H. Kolsky, Proceedings of the Physical Society B 62, 676 (1949).

[53] P. S. Follansbee and C. Frantz, Journal of Engineering Materials and Technology 105, 61 (1983).

[54] B. A. Gama, S. L. Lopatnikov, and J. J. W. Gillespie, Applied Mechanics Reviews 57, 223 (2004).

[55] B. Song and W. Chen, Experimental Mechanics 44, 300 (2004).

[56] W. Chen, B. Zhang, and M. J. Forrestal, Experimental Mechanics 39, 81 (1998).

[57] A. Bartsch, E. Benzel, V. Miele, and V. Prakash, Journal of Neurosurgery 116, 222 (2012).

[58] J. T. Gwin, J. J. Chu, S. G. Diamond, J. J. Crisco, and R. M. Greenwald, Journal of Biomechanical Engineering 132, 011006 (2010).

[59] F. Hernandez, P. B. Shull, and D. B. Camarillo, Journal of Biomechanics 48, 3469 (2015).

[60] W. C. Moss, and M. J. King, Lawrence Livermore National Lab CA, No. LLNL-SR-464951 (2011).

[61] E. J. Pellman, D. C. Viano, A. M. Tucker, and I. R. Casson, Neurosurgery 53, 1328 (2003).

[62] E. J. Pellman, D. C. Viano, C. Withnall, N. Shewchenko, C. A. Bir, and P. D. Halstead, Neurosurgery 58, 78 (2006).

[63] E. J. Pellman, D. C. Viano, A. M. Tucker, I. R. Casson, and J. F. Waecherle, Neurosurgery 53, 799 (2003).

[64] S. Rowson, and S. M. Duma, Annals of Biomedical Engineering 39, 2130 (2011).

[65] National Operating Committee on Standards for Athletic Equipment: Standard Performance Specification for Newly Manufactured Football Helmets: NOCSAE Standard 002-98m03. 1998.

[66] National Operating Committee on Standards for Athletic Equipment: Standard Drop Test Method and Equipment Used in Evaluating the Performance Characteristics of Protective Headgear: NOCSAE Standard 001-04m05. 2004.

[67] H. R. Lissner, M. Lebow, and F. G. Evans, Surgery, Gynecology and Obstetrics 111, 329 (1960).

[68] C. W. Gadd, Research Laboratories, General Motors Corp 660793, 164 (1966).

[69] J. Versace, SAE Technical Paper 710881, 771 (1971).

[70] W. N. Hardy, T. B. Khalil, and A. I. King, International Journal of Impact Engineering 15, 561 (1994).

[71] L. Zhang, K. H. Yang, and A. I. King, Journal of Biomechanical Engineering 126, 226 (2004).

[72] S. A. Berger, W. Goldsmith, and E. R. Lewis. Introduction to Bioengineering, Oxford University Press, USA, 1996.

[73] D. E. Lieberman, M. Venkadesan, W. A. Werbel, A. I. Daoud, S. D'Andrea. I. S. Davis, R. O. Mang'Eni, and Y. Pitsiladis, Nature 463, 531 (2010).

[74] B. M. Nigg, Clinical Journal of Sport Medicine 11, 2 (2001).

[75] M. R. Shorten, Marathon Medicine, 159 (2000).

[76] M. R. Shorten, IV International Conference on the Engineering of Sport 17, (2002).

[77] S. Schwanitz, and S. Odenwald, The Engineering of Sport 7, 95 (2009).

[78] R. Verdejo and N. J. Mills, Polymer Testing 23, 567 (2004).

[79] R.Verdejo and N. J. Mills, Journal of Biomechanics 37, 1379 (2004).

[80] K. Brückner, S. Odenwald, S. Schwanitz, J. Heidenfelder, and T. Milani, Procedia Engineering 2, 2789 (2010).

[81] ASTM F1976 Impact Attenuation of Athletic Shoe Cushioning System and Materials, American Society for Testing and Materials, 2013.

[82] ASTM D3574 Standard Test Methods for Flexible Cellular Materials-Slab, Bonded, and Molded Urethane Foams, American Society for Testing and Materials, 2008.

[83] Q. Liu and G. Subhash, Polymer Engineering and Science 44, 463 (2004).

[84] V. Goga, Computational Modeling and Advanced Simulations Series: Computational Methods in Applied Sciences 24, 67 (2011).